

PERIODIC DOMAIN INVERSION OF MgO-DOPED LITHIUM NIOBATE
BY CORONA DISCHARGE METHOD

PERIODIC DOMAIN INVERSION OF MgO-DOPED LITHIUM NIOBATE
BY CORONA DISCHARGE METHOD

By

JON MARKLE, B.Eng.Mgt.

A Thesis

Submitted to the School of Graduate Studies

In Partial Fulfillment of the Requirements

for the degree

Master of Applied Science

McMaster University

© Copyright by Jon Markle, 2006

Master of Applied Science (2006)
(Engineering Physics)

McMaster University
Hamilton, Ontario

TITLE: Periodic Domain Inversion of MgO-Doped Lithium Niobate
 By Corona Discharge Method

AUTHOR: Jon Markle, B.Eng.Mgt. (McMaster University)

SUPERVISORS: Professor Chang-Qing Xu
 Professor Jen-Shih Chang

NUMBER OF PAGES: x, 103

Abstract

In this work a flow stabilized corona torch plasma was used for periodic domain inversion of MgO-doped lithium niobate with 19.1 μ m periodic gratings. The effective non-linear coefficient (d_{eff}) achieved through corona discharge poling was 17.5 pm/V, which agrees well with theoretical value of 16~19 pm/V. By analysing the second harmonic generation (SHG) tuning curves, the grating uniformity over the 10 mm grating was investigated. The 0.6 nm bandwidth of the SHG tuning at full width half maximum (FWHM) corresponded exactly to the theoretical value. The agreement between experimental data and theoretical results imply that the obtained periodically poled lithium niobate (PPLN) has high quality. By controlling temperature in the range of 20 °C to 120 °C tunability of SHG wavelength was demonstrated between 782 nm and 788 nm.

Discharge characteristics of the corona were studied using a floating potential double probe and optical emission spectroscopy. Using the double probe the distribution of ion density downstream of the corona torch was observed. The maximum ion density of 2×10^{18} (ions/cm³) was achieved 2 mm below the discharge electrode. Measurement of the optical emission spectrum was used to determine the vibrational ion temperature to be 3953 K. The observed spectrum consisted entirely of the second positive band of nitrogen.

The applied voltage range of 9 kV to 10 kV was observed to be optimum for domain growth in periodic poling. Poling uniformity of the 12 mm grating was optimized for an electrode to crystal spacing of 13 mm. Increasing the crystal temperature during poling reduces the required coercive field for domain inversion. This reduces the required applied voltage and also reduces the required poling time by increasing the domain-switching rate. Proton exchange pre-treatment of the (+z) crystal surface prior to poling has been demonstrated to control domain spreading, however future efforts are required to ensure a more reliable nucleation condition. Both high vacuum and spin coated photoresist function to increase electrical discrimination of anode grating and provide an improved nucleation condition for periodic poling of MgO-doped lithium niobate. Poling uniformity of the 12 mm grating was optimised for an electrode to crystal spacing of 13mm.

Acknowledgments

I would like to thank Dr. Chang-Qing Xu, who has been my supervisor at McMaster University, in various forms, for the past 4 years. Dr. Xu has devoted a lot of time and attention to supporting me throughout my academic pursuits. I owe my academic career to him. Secondly, I would like to thank Dr. Jen-Shih Chang for his continual guidance and support on this project. Dr. Chang's knowledge and experience has been invaluable. Without his experimental and analytical guidance this project would not have been a success. I would also like to thank the other members of my defense committee: Dr. Kitai and Dr. Kumar for providing suggestions and taking their time with this thesis.

A large part of my success on this project has come from the excellent people I have worked with. Without their continual support this project could not have progressed to the point it has today. I owe a special thanks to Dr. Wanguo Liang for his extensive efforts in sample preparation and his advice during the parametric study. I am also very grateful to Jorge Fronseca Campos for many fruitful discussions and his help with optical characterization. Both Dr. Liang and Jorge have been a pleasure to work with.

I owe special thanks to Paul Bray for his continuous help with the design and fabrication of numerous devices over the past 4 years. I would also like to acknowledge all the members in Dr. Xu's and Dr. Chang's research groups for their friendship and guidance during my study here at McMaster.

My parents and my sister deserve my greatest gratitude for their continuous encouragement, understanding and support.

TABLE OF CONTENTS

| | |
|---|----|
| CHAPTER 1: INTRODUCTION | 1 |
| 1.1 Background | 1 |
| 1.2 Nonlinear crystal for all-optical wavelength converter | 1 |
| 1.3 Strategy for periodic domain inversion | 3 |
| 1.4 Overview of dissertation | 5 |
| References | 7 |
| CHAPTER 2: LITERATURE REVIEW | 8 |
| 2.1 Lithium niobate | 8 |
| 2.2 Second harmonic generation for optical devices | 9 |
| 2.3 Quasi-phase matching | 11 |
| 2.4 Conventional domain inversion methods | 13 |
| 2.4.1 Thermal methods | 13 |
| 2.4.2 Proton exchange method | 14 |
| 2.4.3 Electron beam writing method | 15 |
| 2.4.4 Direct voltage application (Electrostatic) method | 16 |
| 2.4.5 Corona discharge domain inversion method | 17 |
| 2.5 Mechanism of periodic domain inversion in ferroelectric materials | 18 |
| 2.6 Photorefractive effect | 25 |
| References | 27 |
| CHAPTER 3: EXPERIMENTAL APPARATUS AND PROCEDURES | 29 |
| 3.1 Experimental apparatus | 29 |
| 3.1.1 Environmental chamber | 30 |
| 3.1.2 Crystal holder | 32 |
| 3.1.3 Corona torch | 33 |
| 3.2 Experimental procedures | 35 |
| 3.2.1 Chrome deposition | 35 |
| 3.2.2 Dicing quarter wafers | 36 |
| 3.2.3 Proton exchange treatment | 37 |
| 3.2.4 Domain inversion process | 37 |
| 3.3 Analysis of periodic domain inverted materials | 39 |
| 3.3.1 Characteristics of periodic domain inversion | 39 |
| 3.3.2 Initial visual inspection | 40 |
| 3.3.3 Domain inspection via etching | 40 |
| 3.3.4 Domain inspection via cross sectional etching | 41 |
| 3.3.5 Quantitative analysis techniques for domain inverted crystals | 41 |
| References | 46 |

| | |
|--|-----|
| CHAPTER 4: CORONA TORCH CHARACTERIZATION | 47 |
| 4.1 Plasma parameters | 48 |
| 4.1.1 Double probe method | 49 |
| 4.1.2 Ion density distribution | 52 |
| 4.1.3 Optical emission spectroscopy background | 56 |
| 4.1.4 Optical emission spectrum from discharge | 58 |
| References | 61 |
| CHAPTER 5: PERIODIC DOMAIN INVERSION BY CORONA TORCH METHOD | 62 |
| 5.1 Corona torch characteristics | 62 |
| 5.2 Torch Variables | 63 |
| 5.2.1 Effect of applied voltage | 64 |
| 5.2.2 Effect of electrode position | 68 |
| 5.2.3 Effect of gas and flow rate | 72 |
| 5.3 Crystal variables | 72 |
| 5.3.1 Effect of crystal temperature | 74 |
| 5.3.2 Effect of anode properties | 75 |
| 5.3.3 Effect of proton exchange pretreatment | 76 |
| 5.3.4 Batch dependent properties | 79 |
| 5.4 Characterization of MgO-PPLN | 79 |
| 5.4.1 Quality of optimized Periodic Domain inversion | 80 |
| 5.4.2 SHG performance of MgO-PPLN | 82 |
| 5.4.3 QPM temperature shift in MgO-PPLN | 84 |
| 5.4.4 SHG performance related to domain characteristics in MgO-PPLN | 86 |
| 5.4.5 SHG efficiency of MgO-PPLN | 88 |
| References | 90 |
| CHAPTER 6: CONCLUSIONS | 91 |
| CHAPTER 7: RECOMMENDATION FOR FUTURE WORK | 94 |
| APPENDICES: | |
| Appendix A: Dimension drawings of major components | 95 |
| Appendix B: A list of dominant optical emission bands in N ₂ – O ₂ plasmas | 100 |

LIST OF FIGURES

| | | |
|--------------|---|----|
| Figure 2.1: | Crystal structure of lithium niobate. | 8 |
| Figure 2.2: | Schematic of single-pass short wavelength coherent light source. | 9 |
| Figure 2.3: | Principle of second harmonic generation. | 9 |
| Figure 2.4: | QPM effect on $E(\omega_2)$ and $I(\omega_2)$. | 12 |
| Figure 2.5: | Periodic domain inversion by (a) Ti diffusion (b) LiO ₂ outdiffusion (c) SiO ₂ Cladding and heat treatment. | 14 |
| Figure 2.6: | Fabrication of domain inversion via proton exchange. | 15 |
| Figure 2.7: | Schematic of EB domain inversion. | 16 |
| Figure 2.8: | Electrostatic method of periodic poling lithium niobate. | 16 |
| Figure 2.9: | Comparison of domain inversion cross sections for different processing methods. | 17 |
| Figure 2.10: | Schematic diagram of corona discharge poling. | 18 |
| Figure 2.11: | Typical hysteresis characteristics for non-doped and doped crystal. | 19 |
| Figure 2.12: | Lithium niobate lattice change with domain inversion. | 20 |
| Figure 2.13: | Effect of spontaneous polarization (P_s) on lithium potential. | 21 |
| Figure 2.14: | Sequence of polarization inversion for a stoichiometric crystal. | 22 |
| Figure 2.15: | Sequence of polarization inversion for a congruent crystal. | 23 |
| Figure 2.16: | Temperature dependence of cohesive field (5% MgO doped). | 23 |
| Figure 2.17: | Six stages of domain kinetics during electric filed poling. (a) Domain nucleation at the electrode edges. (b) Domain tip propagation toward the opposite face of the crystal. (c) Termination of the tip at the opposite side of the crystal. (d) Rapid coalescence under the electrodes. (e) Propagation of the domain walls out from under the electrodes and stabilization of the new domains. | 24 |

| | | |
|--------------|---|----|
| Figure 3.1: | Photograph of environmental chamber with corona torch system. | 30 |
| Figure 3.2: | Schematic of corona torch domain inversion processing system. | 31 |
| Figure 3.3: | Schematic of crystal holder. | 33 |
| Figure 3.4: | Schematic of corona torch. | 33 |
| Figure 3.5: | Corona torch assembly procedure. | 34 |
| Figure 3.6: | Two types of corona torch ground ring electrodes. | 35 |
| Figure 3.7: | Quarter wafer with 12mm diameter anode pattern. | 36 |
| Figure 3.8: | Domain analysis via cross-sectional etching in HF. | 41 |
| Figure 3.9: | Image of typical domain inverted structure after etching by HF. | 42 |
| Figure 3.10: | Typical pixel analysis for determining domain duty cycle. | 43 |
| Figure 3.11: | Typical derivative of pixel intensity used for determination of domain duty cycle. | 44 |
| Figure 3.12: | Pixel length measurements of both domain width and grating period. | 45 |
| Figure 4.1: | Effect of crystal presence on corona torch time averaged discharge current-voltage characteristics. | 48 |
| Figure 4.2: | Circuit diagram of double probe. | 49 |
| Figure 4.3: | Schematic of potential distribution between the probes of a floating potential double probe system. | 50 |
| Figure 4.4: | Schematic of a double probe I-V characteristic with symmetric probes. | 51 |
| Figure 4.5: | Schematic of double probe plasma profile measurement. | 53 |
| Figure 4.6: | Ion density profile along gas exit axis. | 54 |
| Figure 4.7: | Ion densities vs. Position in 2D. | 55 |
| Figure 4.8: | Potential curves for N ₂ in the range from 6 to 12 eV. | 57 |

| | | |
|--------------|---|----|
| Figure 4.9: | Typical optical emission spectrum of the corona torch, at $V_{\text{applied}} = 10 \text{ kV}$, $I_{\text{corona}} = 150 \mu\text{A}$, separation distance was 13 mm and 5% MgO LN crystal present. | 59 |
| Figure 4.10: | Population density versus the vibrational quantum number ν' . | 60 |
| Figure 5.1: | Typical corona torch current waveform yielding high quality crystal poling. | 63 |
| Figure 5.2: | Typical domain structures for incorrect applied voltage. | 65 |
| Figure 5.3: | Horizontal processing uniformity for different corona torch electrode heights. | 69 |
| Figure 5.4: | Poling of a 76 mm substrate with single corona torch in center position. | 70 |
| Figure 5.5: | Poling of a 76 mm substrate with multiple corona torch positions. | 71 |
| Figure 5.6: | Typical corona current vs. time. | 73 |
| Figure 5.7: | Effect of proton exchange treatment on domain profile. | 77 |
| Figure 5.8: | Typical domain profile under optimized poling conditions. | 80 |
| Figure 5.9: | Measured domain width and grating period at different vertical positions in the crystal. | 81 |
| Figure 5.10: | Schematic of experimental setup used to analyze SHG performance. | 82 |
| Figure 5.11: | SHG power vs. wavelength. | 83 |
| Figure 5.12: | Temperature effect on QPM wavelength based on Sellmeier equation. | 85 |
| Figure 5.13: | Temperature effect on QPM wavelength. | 86 |
| Figure 5.14: | Device performance vs. vertical position. | 87 |
| Figure 5.15: | Device performance vs. domain duty cycle. | 88 |
| Figure 5.16: | SHG generation with a focused Gaussian beam. | 89 |

LIST OF TABLES

| | | |
|------------|---|----|
| Table 3.1: | Microscope Resolutions (Nikon E200) | 42 |
| Table 4.1: | Identified 2 nd positive band emissions used and values used in calculations | 59 |
| Table 5.1: | Typical effect of applied voltage on poling result | 67 |
| Table 5.2: | Typical data from temperature study of corona torch at applied voltage V_c | 75 |

CHAPTER 1: INTRODUCTION

1.1 Background

For the past quarter century, many different types of optical wavelength converters have been developed. More recently, the developmental effort has been significantly increased due to the requirement from advanced communications systems. All optical wavelength converters are an ideal solution because they don't require signal recognition and regeneration via electrical systems. These devices are also well suited for the generation of coherent light ranging from UV to Mid IR wavelengths.

In this chapter, a brief description of all optical wavelength converters and their applications for optical fiber communications and laser light sources are presented. The strategies used for periodic domain inversion are discussed and followed by an overview of the dissertation.

1.2 Nonlinear crystal for all-optical wavelength converter

Nonlinear optical effects provide a wide variety of possibilities for realizing important and unique photonic functions unfeasible with linear optics and electronics. Many optical instruments in laboratories currently make use of bulk nonlinear crystals. The implementation of a waveguide structure in nonlinear crystals confines the interacting waves and allows for the development of compact efficient devices that are more practical for consumer products. These nonlinear waveguide devices have been the focus of research for the past 30 years [1].

For an application of telecommunications, nonlinear waveguides have the potential to function as all-optical wavelength converters at the cross connects of optical networks. These devices will increase network flexibility by decreasing channel blocking and make better use of available wavelengths. All optical wavelength conversion does not require signal recognition and regeneration via electrical means making the device faster and more transparent to different signal formats.

For the purpose of coherent light generation, nonlinear crystals function to convert laser light at one wavelength to another. This can extend the existing spectral coverage of the currently available light sources. Commercially this device can be coupled with an inexpensive semiconductor laser diode of the appropriate wavelength which allows for a cost effective solution to generating coherent light in certain spectral regions. Currently semiconductor laser diodes are not available in wavelengths between 500 and 600 nm (green to yellow) and have difficulties in achieving wavelengths above 2000 nm (mid-IR). By creating short period gratings ($< 2 \mu\text{m}$) a coherent UV light source can be created. Considerable interest in a compact cost effective UV laser is driven by the increasing need to optically store information at greater densities. The need for coherent light sources in the visible spectrum has also been pursued extensively for the purpose of optical data storage, as well as colour displays applications and biotechnology [3]. The common device needs are: wavelength tunability, high output power, small, rugged and inexpensive. Environmental modeling and process analysis has been the driving force behind the requirement of a tunable laser source in the mid infrared (2 - 5 μm) region of the spectrum. Many solutions exist to generate coherent

light in these different spectral regions however few meet the needs of tunability and room temperature operation.

A waveguide structure employed in MgO:PPLN is an excellent solution to an all optical wavelength converter for many reasons. First, the crystal is transparent over a large spectral range from 300 nm to 5000 nm which gives significant flexibility with regard to available wavelengths. The employment of a waveguide structure makes optical confinement very effective and achievable over long grating lengths. These two factors dramatically increase the efficiency of the second harmonic generation process. The recent introduction of MgO doping at 5% mol in LiNbO₃ has increased the allowable pump power of the device by a factor of 100 [5] before the onset of photorefractive damage. The output power of the second harmonic is proportional to the intensity of the pump source squared. By increasing the pump power by a factor of 100 while using lithium niobate with 5% mol MgO doping the output power of the device can be increased by roughly a factor of 10 000. The introduction of the MgO doping in lithium niobate has greatly improved this material for the purpose of coherent light generation.

1.3 Strategy for periodic domain inversion

With the introduction of the MgO doping in PPLN considerable difficulties in fabricating periodic domain inverted grating in the material were observed. It is not well understood why the well established electrostatic method of domain inversion doesn't work well for fabrication of periodic grating in the doped crystal. This problem may be due to the doping non-uniformity in the material. Doping irregularity or the presence of

crystal imperfections would create variation in the poling rates of different crystal regions. In order to improve this problem the corona discharge method was proposed [5]. The principle behind this method is that by soft charging the (-z) surface of the crystal via a negative polarity corona discharge a more uniform process of domain inversion can be achieved. Through this charging method, the negative effect of crystal irregularities can be minimized by limiting the mobility of charge on the crystal surface. This increases the likelihood that a uniform poling field will be maintained across the substrate with the presence of crystal imperfections.

The goal of this project has been to develop a corona discharge method for the purpose of fabricating periodic domain reversal in MgO doped LiNbO₃. Early in this project attempts were made by surface charging via a corona wire. The corona discharge arrangement of wire electrode was considered optimal to process long gratings as previously demonstrated Harada and Nihei [5]. Multiple corona wire poling systems were fabricated and tested however they failed to achieve adequate surface charge for uniform domain inversion.

In order to increase the achievable surface charge, a flow stabilized corona torch was introduced. This device used a nitrogen gas flow through a hollow electrode to stabilize the corona discharge and aid in ion transport. The characteristics of the corona torch were studied by an electrostatic probe and optical emission spectroscopy. This device was optimized for creating a 19.1 um period grating over a 12 mm diameter circular pattern.

The impact of this work is that now another corona discharge method of charging ferroelectric substrates for the purpose of domain inversion has been demonstrated. This work is a preliminary investigation into ferroelectric poling via corona discharge. One of the major contributions from this work is that the corona discharge poling method represents a valid solution for the large scale production of MgO:PPLN. This method involves less substrate preparation and is better suited to deal with crystal imperfections, hence it may achieve higher process yields than the traditional electrostatic method.

1.4 Overview of dissertation

Chapter 2 introduces the nonlinear optical crystal lithium niobate and reviews wavelength conversion by second harmonic generation. The necessity for phase matching and the quasi-phase matching technique are discussed in detail. Different domain inversion methods are introduced and the rationale and motivation behind the corona discharge charging approach is presented. The basic mechanism of domain inversion in ferroelectric materials is described and the chapter closes with a description of the photorefractive effect.

Chapter 3 explains the experimental apparatus and procedures involved in the different stages of this work. The analytical methods used in evaluating the quality of periodic domain inverted gratings are also covered in detail.

Chapter 4 presents the properties of the corona torch plasma used in the poling process. The plasma discharge is characterized using an electrostatic double probe placed in the plasma region and also by optical emission spectroscopy methods.

Chapter 5 discusses the characteristics of a functional corona torch. The interdependence of many of the poling parameters and the complexity this introduces in optimizing the process is explained. The unique crystal properties and their significant contribution to the complexity of the poling process are presented. The results of studying the many different parameters in the poling process and how they influence the poling result is discussed in detail. Periodic gratings fabricated from the optimized corona torch are then tested optically. The quality of these gratings is then characterized through the optical performance of the wavelength converter.

Conclusions and Recommendations for future work were summarized in chapters 6 and 7.

References for Chapter 1

- [1] T. Suhara and M Fujimura, “Waveguide Nonlinear-optic Devices,” Springer, New York (2003).
- [2] T. Sugita, K. Mizuuchi, Y. Kitaoka and K. Yamamoto, “Ultraviolet Light Generation in a Periodically Poled MgO:LiNbO₃ Waveguide,” *Jpn. J. Appl. Phys.* Vol. **40** (2001) 1751-1753.
- [3] D. C. Gerstenberger, G. E. Tye, “Efficient second-harmonic conversion of c-w single-frequency Nd:YAG laser light by frequency locking to a monolithic ring frequency doubler,” *Opt. Lett.* **16** (13), 992-994. 1991.
- [4] D. Hofmann, G. Schreiber, ” Quasi-phase-matched difference-frequency generation in periodically poled TiLiNbO₃ channel waveguides,” *Opt. Lett* **24** (13), 896-989, 1999.
- [5] A. Harada and Y. Nihei, “Bulk periodically poled MgO-LiNbO₃ by corona discharge method,” *Applied Physics Letters* **69** (18), 2629-31 (1996).

CHAPTER 2: LITERATURE REVIEW**2.1 Lithium niobate**

Lithium niobate is often referred to as “the silicon of nonlinear optics.” It is transparent from 400 nm to 4000 nm and has a high nonlinear coefficient. Its melting temperature is 1257 °C and its density is 4.65 g/cm³. Figure 2.1 shows the trigonal crystal structure of the crystal. Lithium niobate can be doped by magnesium oxide, which increases its resistance to the photorefractive effect (also known as optical damage)[1]. These characteristics of lithium niobate make it an ideal material for creating an all-optical wavelength converter.

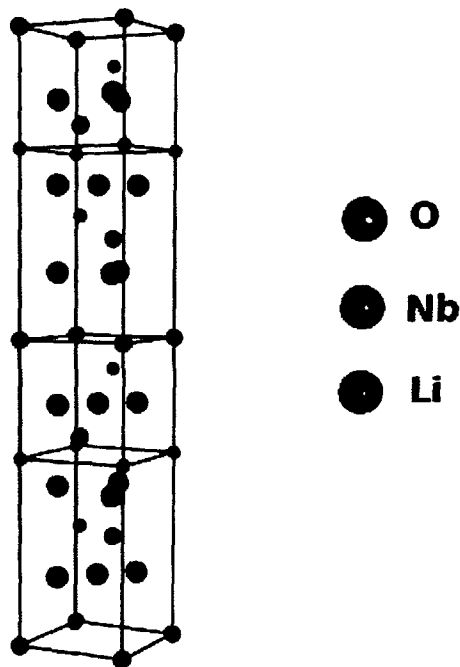


Figure 2.1: Crystal structure of lithium niobate.

All optical wavelength converters are needed for the future challenges in the optical communications industry. These wavelength converters can also be used for the generation of short wavelength coherent light sources. For example, by coupling this device with an

inexpensive semiconductor laser a short wavelength laser source can be achieved. This short wavelength is accomplished by second harmonic generation based wavelength conversion and would otherwise be difficult, if not impossible to produce. A schematic of such a device can be seen in Figure 2.2.

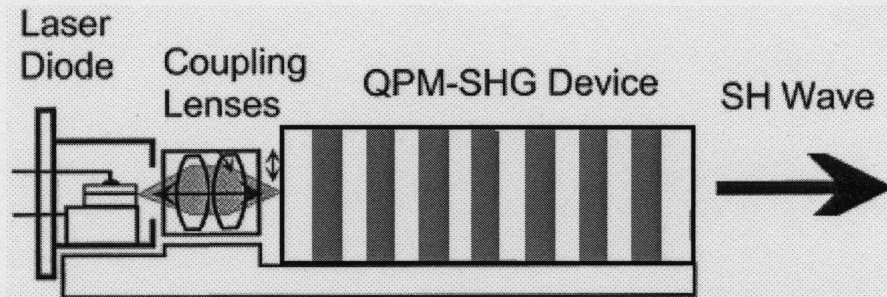


Figure 2.2: Schematic of single-pass short wavelength coherent light source [2].

2.2 Second harmonic generation for optical devices

Second harmonic generation (SHG, also called frequency doubling) is a nonlinear optical process, in which photons interacting with a nonlinear material are effectively "combined" to form new photons with twice the energy, and therefore twice the frequency and half the wavelength of the initial photons. Figure 2.3 shows the principle of SHG.

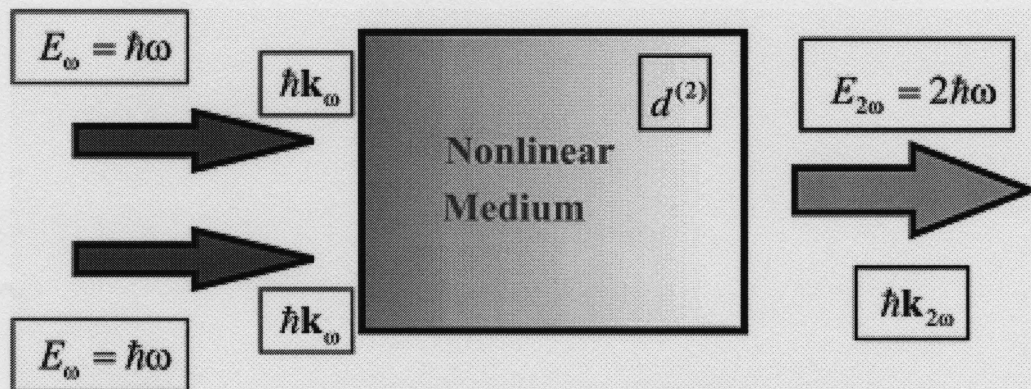


Figure 2.3: Principle of second harmonic generation.

Only under special circumstances is the rate of SHG significant. The two fundamental requirements for efficient nonlinear power conversion are that the pump intensity is high over a certain propagation length, and that the involved beams preserve a certain phase relationship during propagation.

In SHG, the fundamental wave of frequency ω_1 interacts with the second-order nonlinear susceptibility of a material $\chi^{(2)}$ to produce a polarization wave at the second-harmonic frequency $\omega_2 = 2\omega_1$. Since the polarization wave is driven by the fundamental wave, it travels with the same velocity, determined by the index of refraction n_1 . The polarization wave radiates a second-harmonic wave which travels at a velocity determined by the index of refraction at the harmonic wavelength n_2 . In general, n_2 is greater than n_1 due to normal dispersion in the material. The wavelength dependent refractive index causes the fundamental and second harmonic waves to travel at different phase velocities. The power flow from the fundamental to the second harmonic is determined by their relative phase. The continuously changing phase mismatch between these two waves caused by their different phase velocities leads to an oscillation in the direction of power flow. This results in repetitive growth and decay of the second harmonic intensity along the length of the interaction. This situation is illustrated by the phase mismatch curve in Figure 2.4(c). The distance over which the relative phase of the two waves changes by π is the coherence length, l_c as follows [3];

$$l_c = \frac{\pi}{4}(n_2 - n_1) \quad (2-1)$$

The coherence length represents half the period of the growth and decay cycle of the second harmonic. If not for the phase mismatch the intensity of the second harmonic would grow quadratically over the propagation length of the device.

2.3 Quasi-phase matching

In order to achieve efficient nonlinear wavelength conversion quasi-phase matching (QPM) must be employed throughout the crystal structure. The theory of QPM was first described by Armstrong and Bloembergen [4]. Essentially, it is a technique that compensates for the difference in phase velocity between the fundamental wave and its second harmonic in a nonlinear crystal caused by natural dispersion. This approach is fundamentally different from birefringent phase matching, where the anisotropy of nonlinear crystal is used to find unique propagation directions whereby the fundamental and harmonic waves have the same phase velocity.

In QPM, the sign of the nonlinear coefficient is reversed every coherence length, causing the locally generated polarization field to transfer power to the harmonic beam. By compensating for phase-velocity mismatch in this way, the largest elements of a crystal's nonlinear tensor can be accessed throughout the entire transparency range. Figure 2.4 shows the effect of QPM on $E(\omega_2)$ vectorially and $I(\omega_2)$ over the length of propagation. In the non-phase matched case (a), the generated $E(\omega_2)$ grows and reaches a maximum at $z = l_c$. With further propagation $E(\omega_2)$ begins to shrink returning to zero at $z = 2 l_c$. In the QPM case (b), the sign of the nonlinear interaction is reversed every l_c . This is achieved by reversing the sign of $d(z)$. The resultant $E(\omega_2)$ grows monotonically.

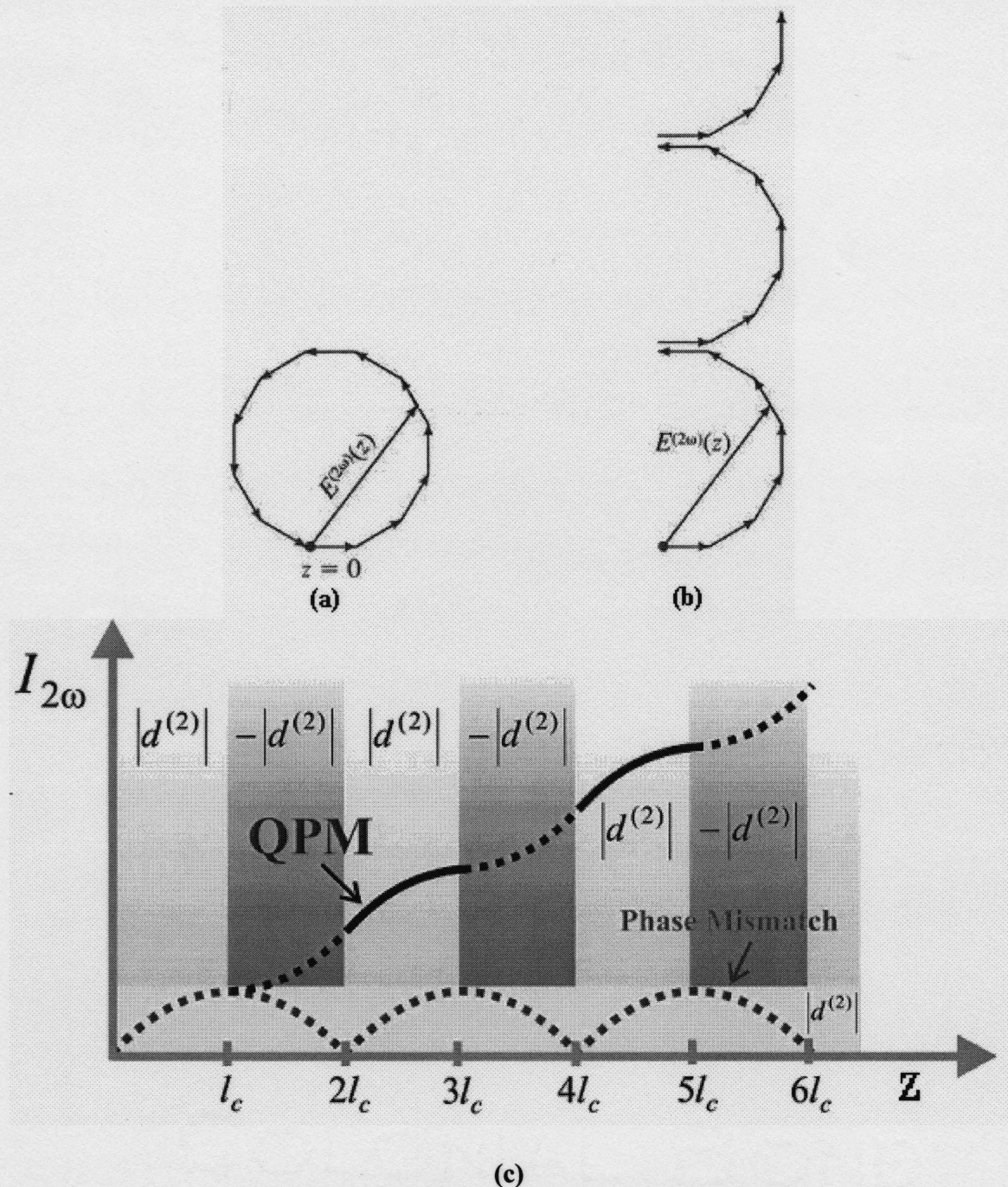


Figure 2.4: QPM effect on $E(\omega_2)$ and $I(\omega_2)$ [5].

In practice however, it is difficult to make a perfect QPM grating in a nonlinear crystal. Factors such as uncertainty in exact value of material constants, fabrication

errors, and the change of material constants due to the fabrication process may give rise to a residual phase mismatch. Working conditions of the device can also effect the phase matching. Changes in ambient temperature, laser diode wavelength fluctuation, and the photorefractive effect can cause deviation in performance in an optical wavelength converter [6]. The photorefractive effect is further discussed in section 2.7.

2.4 Conventional domain inversion methods

The QPM concept was first proposed for the bulk configuration in the 1960s. It was not until much later that an effective method to fabricate the structure was demonstrated. The first QPM-SHG structure in lithium niobate used a Ti diffusion process and was done by Jaskorzynska [7]. Unfortunately the conversion efficiency was relatively low.

2.4.1 Thermal methods

Early studies [2] in the pursuit of periodic poling (1980-1990) believed that the domains were frozen in the crystal and that considerable temperatures were required in order to achieve domain inversion. Significant effort was devoted toward methods of achieving periodic domains during the growth process. Czochralski [8] growth incorporating the modulation of doping, temperature, current and laser heating were attempted. Bulk SHG was achieved but the processing was limited by the difficulty to precisely control the domain period. Many high temperature methods involving diffusion processes were also pursued. Miyazawa [9] observed that a domain inverted layer

resulted from Ti diffusion shown in Figure 2.5a. It was proposed that the inversion mechanism was related to a change in spontaneous polarization due to Ti diffusion and associated depolarization. Lithium out-diffusion was also observed to cause domain inversion. This was achieved in two different ways depending on the gas environment as shown in Figures 2.5b and 2.5c.

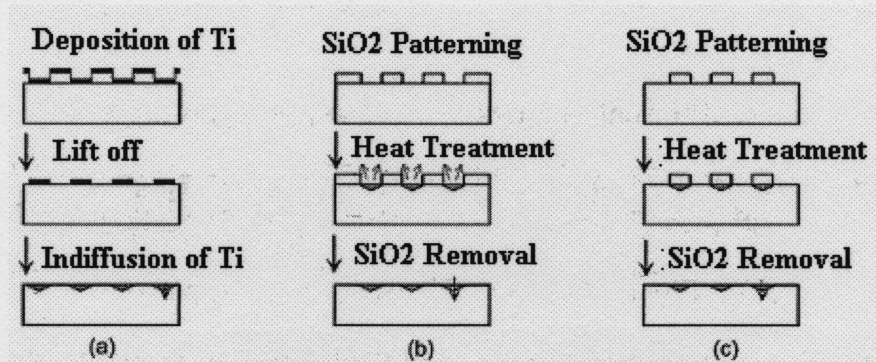


Figure 2.5: Periodic domain inversion by (a) Ti diffusion (b) LiO₂ out-diffusion (c) SiO₂ Cladding and heat treatment [2].

Although prototype waveguides were fabricated via these different methods, the conversion efficiencies were relatively low. The shallow inversion depth and imperfect domain profile were two of the major problems [2].

2.4.2 Proton exchange method

In an effort to achieve QPM gratings at temperatures significantly lower than the Curie point, proton exchange methods were studied. Suhara et al. [10] proposed the use of proton exchange to achieve domain inversion in lithium niobate. There are many different methods of proton exchange. The depth of domain inversion is greater than the two thermal methods previously mentioned. Further increase in domain depth can be achieved by masking the crystal to avoid out-diffusion during thermal annealing. Using

this method many high efficiency waveguide devices have been demonstrated. Figure 2.6 shows three different methods of domain inversion via proton exchange.

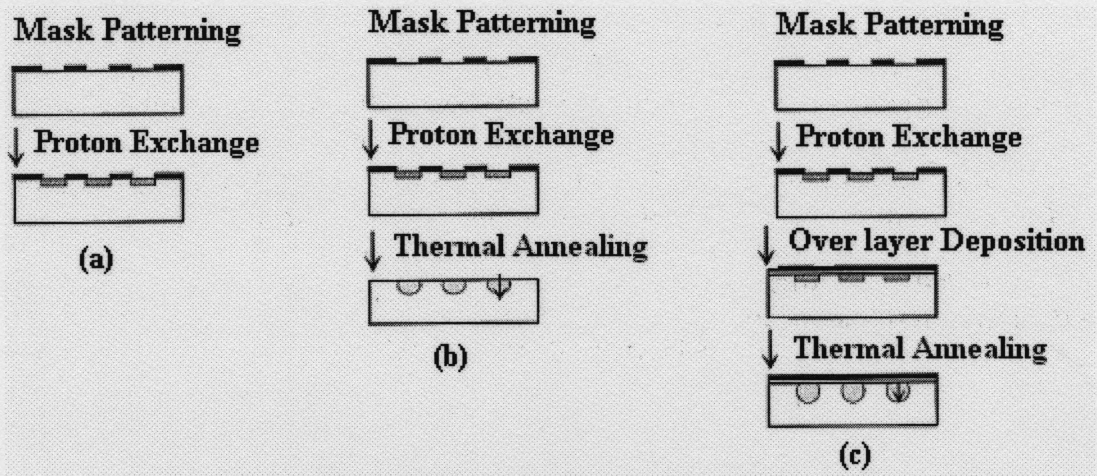


Figure 2.6: Fabrication of domain inversion via proton exchange [2].

2.4.3 Electron beam writing method

Domain inversion via electron beam (EB) bombardment has been achieved in lithium niobate wafers up to 1mm in thickness at room temperature [11]. The grating is achieved by scanning each individual domain along the periodic grating. The exact poling method is not completely understood, where it is believed that some of the electrons that impinge on the crystal surface actually penetrate the material and accumulate. Figure 2.7 shows a schematic of the EB writing process. Fabrication of these gratings has been demonstrated however reproducibility cannot be obtained. More precise control of EB scanning is required.

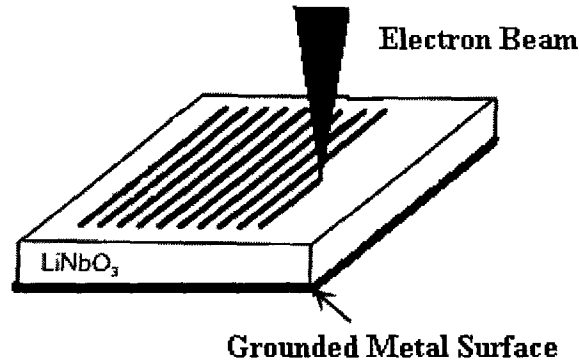


Figure 2.7: Schematic of EB domain inversion.

2.4.4 Direct voltage application (Electrostatic) method

Most recently, many investigators [2] have studied bulk periodic domain formation in ferroelectrics by applying an electric field using lithographically defined periodic electrodes. Yamada, et al. [12] reported the demonstration of this approach. This technique is referred to as the electrostatic technique and has become the industry standard for fabricating domain inversion structures in non-doped lithium niobate. A schematic of this poling method is shown in Figure 2.8.

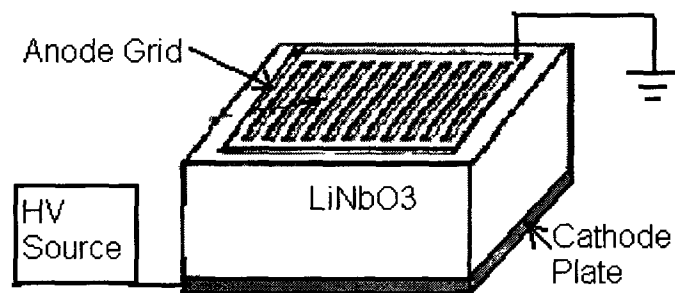


Figure 2.8: Electrostatic method of periodic poling lithium niobate.

Among these four poling methods, the electron beam and electrostatic methods are the only two capable of achieving adequate poling depth for device fabrication. These processes also yield a superior quality boundary between domains. Figure 2.9

shows domain cross sections for the various different poling methods. Due to factors such as time, cost, temperature required, and complexity, the electrostatic method has become the standard method for achieving periodic domain version in lithium niobate.

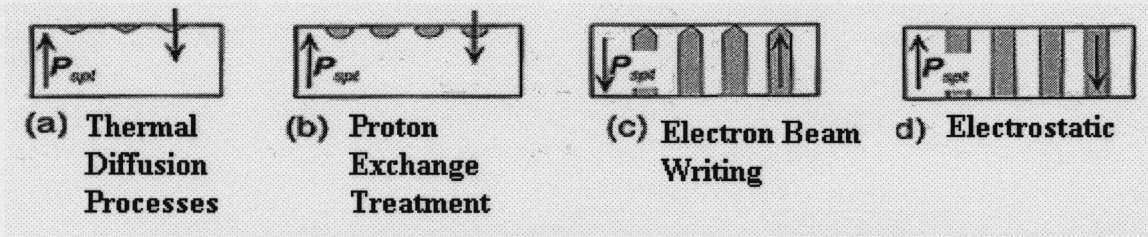


Figure 2.9: Comparison of domain inversion cross sections for different processing methods [2].

2.4.5 Corona discharge domain inversion method

To achieve devices capable of higher output powers, a lithium niobate crystal with a 5 mol % MgO dopant was developed [13]. This crystal has a higher resistance to photorefractive effect, which allows for an increase in pumping power by two orders of magnitude [14]. It is believed that this effect is due to the suppression of the internal electric field. The dopant increases the non-uniformity of the crystal, making it difficult to use the traditional electrostatic technique when poling the crystal. To pole the doped crystal, the corona discharge technique was developed [1]. Figure 2.10 shows a schematic diagram of corona discharge poling.

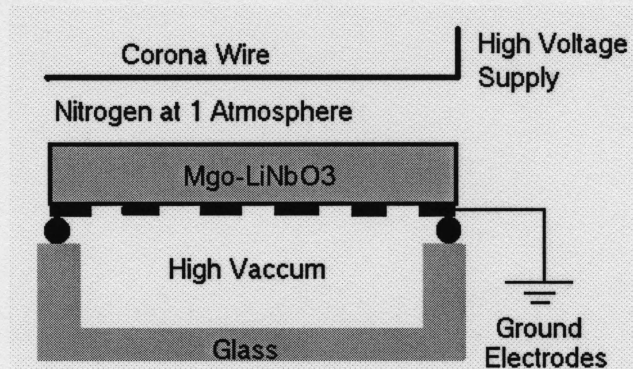


Figure 2.10: Schematic diagram of corona discharge poling [1].

Most of the previous works[2] on crystal poling focus mainly on how to pole the crystal, and few models have been proposed on the mechanism of crystal poling. In this work, the advanced corona discharge poling was developed for poling the MgO doped crystal, and the difference in poling mechanism between the electrostatic and corona discharge technique was discussed.

2.5 Mechanism of periodic domain inversion in ferroelectric materials

Ferroelectric domain inversion is caused by applying an external field anti-parallel to the polarization of the material. Lithium niobate is of the displacive type of ferroelectrics belonging to the trigonal system (3m point group). The Curie temperature of lithium niobate is 1195 °C [8]. In order to alter the spontaneous polarization of lithium niobate an external electric field of at least 20.7 kV/mm must be applied at room temperature [8]. For MgO doped lithium niobate the required field is reduced to roughly 1/5 of this value. It is not well understood how the 5% per mole MgO dopant contributes to the heightened properties of the doped crystal, or why exactly it complicates the poling process. At this time it is believed that the dopant contributes conductivity and

irregularity to the crystal and it is these two properties that complicate the poling process. Figure 2.11 shows the typical hysteresis characteristics for both the non-doped and doped lithium niobate crystals. It can be seen that the inversion characteristics of the doped crystal are analogous to those for the non-doped crystal; however the coercive field and breakdown fields are dependent on MgO dopant. It should be noted that there is also considerable sample to sample variance between the doped crystals which complicates QPM-SHG device fabrication [8].

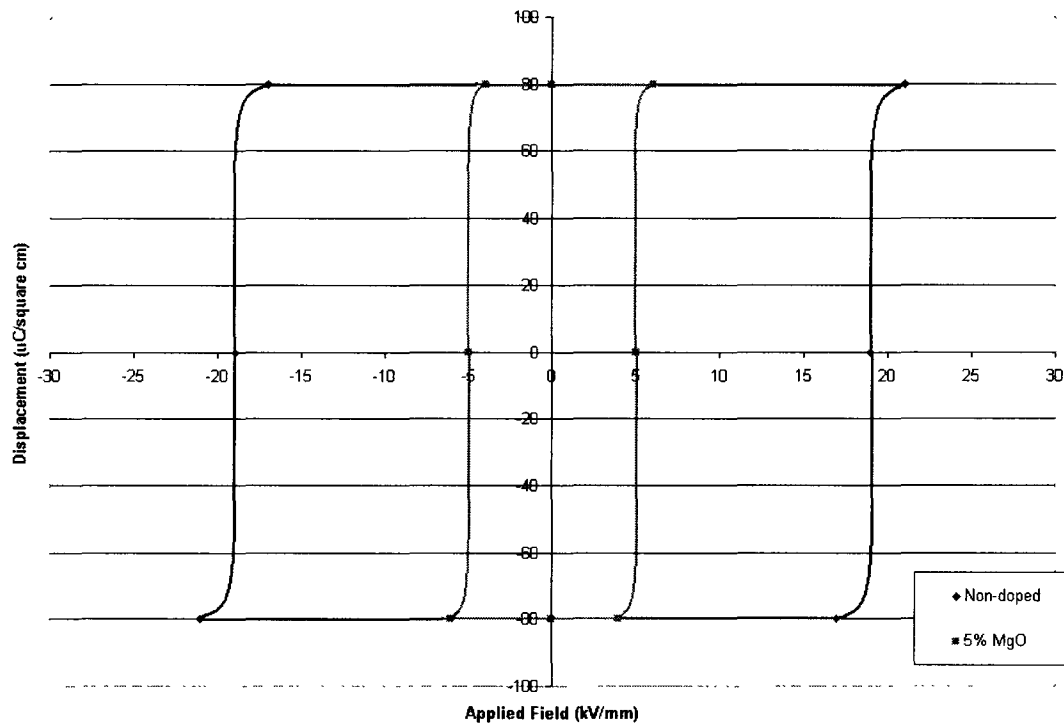


Figure 2.11: Typical hysteresis characteristics for non-doped and doped crystal [8,15].

The change in spontaneous polarization is a result of the displacement of the lithium ions in the crystal lattice. Figure 2.12 shows how the orange lithium atoms are

displaced in the lattice, where the purple atoms are niobium and the white atoms are oxygen.

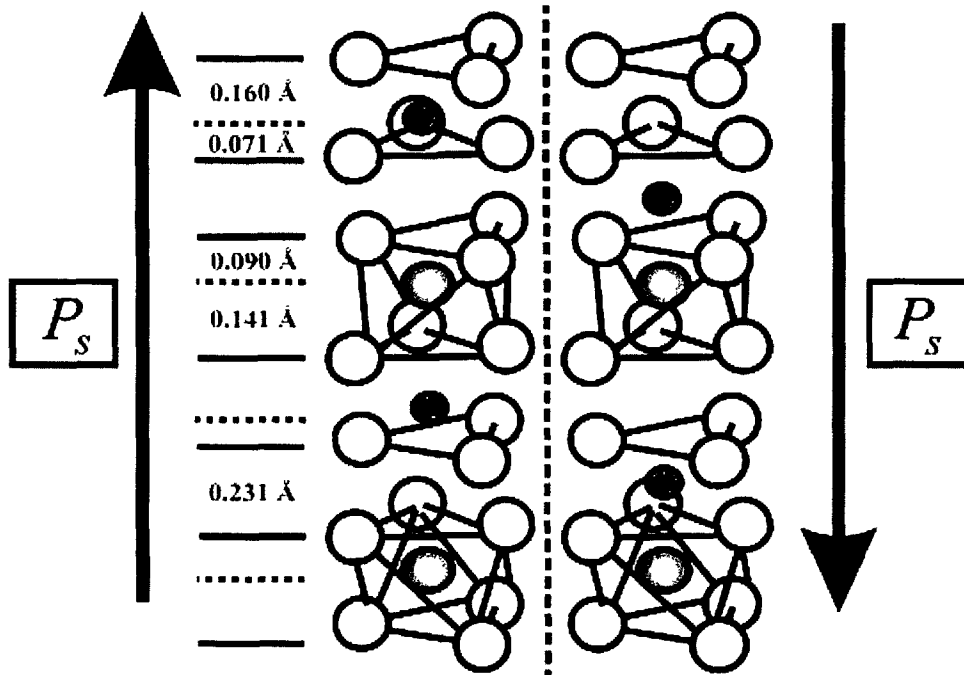


Figure 2.12: Lithium niobate lattice change with domain inversion [16].

The microscopic behavior of the lithium ions can be interpreted in terms of potential energy. The local electric field that affects the ion can be written [2] as

$$\mathbf{E}_{loc} = \mathbf{E} + \frac{\gamma}{3\epsilon_0} \mathbf{P} \quad (2.2)$$

where \mathbf{E} and \mathbf{P} are the external field and polarization. The second term represents the effect of the surrounding ions. The potential for the lithium ions, with the effect of polarization neglected, would have two symmetrical minima corresponding to both sides of the oxygen triangle as shown in Figure 2.13(a1). The effect of polarization generates a much deeper minimum as shown in Figure 2.13(a2).

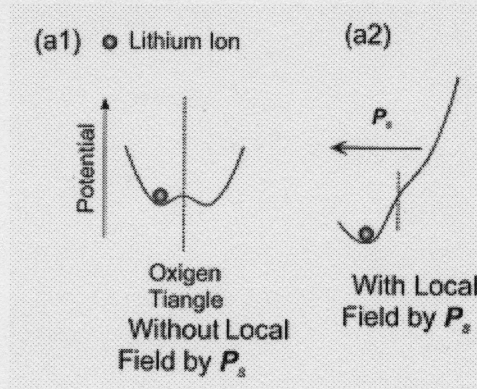


Figure 2:13: Effect of spontaneous polarization (P_s) on lithium potential [2].

The external field required to eliminate the potential barrier however, far exceeds experimental findings. It is very difficult to invert domains in a uniform crystal. In fact domain inversion requires nucleation resulting from defects.

For lithium ions present on a horizontal domain wall, it can be easily understood that the long range effects of spontaneous polarization cancel out due to symmetry arguments. Thus, the local field is influenced by the short range influence of neighboring lithium ions, which is far less in magnitude than the second term in equation 2.2. The expression for local field on a domain boundary can be written as

$$\mathbf{E}_{loc} = \mathbf{E} + \mathbf{E}_{sr} \quad (2.3)$$

When the applied field reaches the cohesive field, the barrier is removed as shown in Figure 2.14(b2). Then with the aid of thermal energy the Li ion is shifted to the other site as shown in Figure 2.14(b3). Both forward growth and sideways growth function in this manner. The reason sideways growth is significantly slower than vertical growth stems from the short range effect of neighboring lithium ions. Due to lattice geometry, ion presence in the vertical direction contributes more to the local field. When the

applied field is removed the Li ion remains in its new position as shown in Figure 2.14(b4). This new ion position gives rise to a new spontaneous polarization as shown in Figure 2.14(b5).

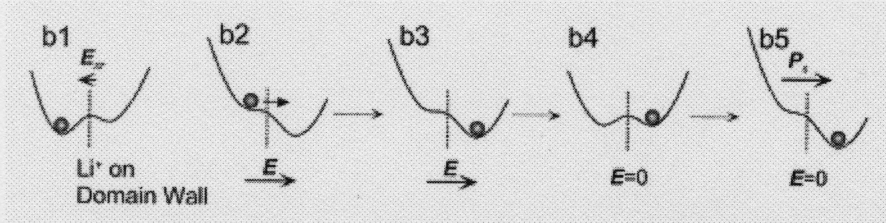


Figure 2.14: Sequence of polarization inversion for a stoichiometric crystal [2].

In order to accurately address the difference associated with congruent crystals, the internal field must be considered. Equation 2.2 can be rewritten as follows

$$\mathbf{E}_{loc} = \mathbf{E} + \frac{\gamma}{3\epsilon_0} \mathbf{P} + \mathbf{E}_{int} \quad (2.4)$$

The non-stoichiometric defects contribute electric charges in the crystal. These charges distribute themselves in order to minimize total energy. This gives rise to an internal field parallel to the spontaneous polarization. Therefore, the local field on a domain boundary can be described as

$$\mathbf{E}_{loc} = \mathbf{E} + \mathbf{E}_{sr} + \mathbf{E}_{int} \quad (2.5)$$

The presence of the internal field makes the required electric field that much higher as shown in Figure 2.15(c3). The redistribution of defect charges is required for the proper relaxation of the lithium ion into its new position. This process takes on the order of a millisecond and is considered to be caused by lithium vacancies [17]. If this

relaxation time is not accounted for the lithium ions will revert back to their original position as shown in Figure 2.15 (c5).

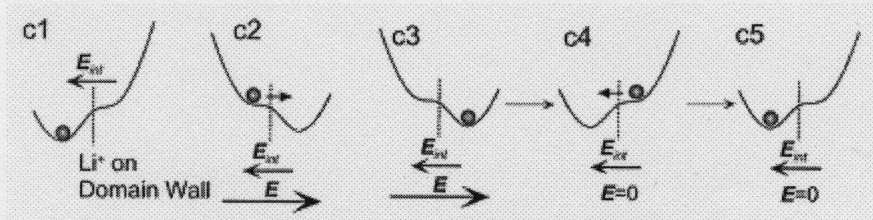


Figure 2.15: Sequence of events for a congruent crystal.

It is this small displacement of the lithium ions that makes the crystal generate the opposite phase of the second harmonic light as pump light passes through the material. The cohesive field that must be overcome in order to make this displacement is dependent on crystal temperature and is shown in Figure 2.16. The rate of domain switching is a function of crystal temperature and applied electric field [18].

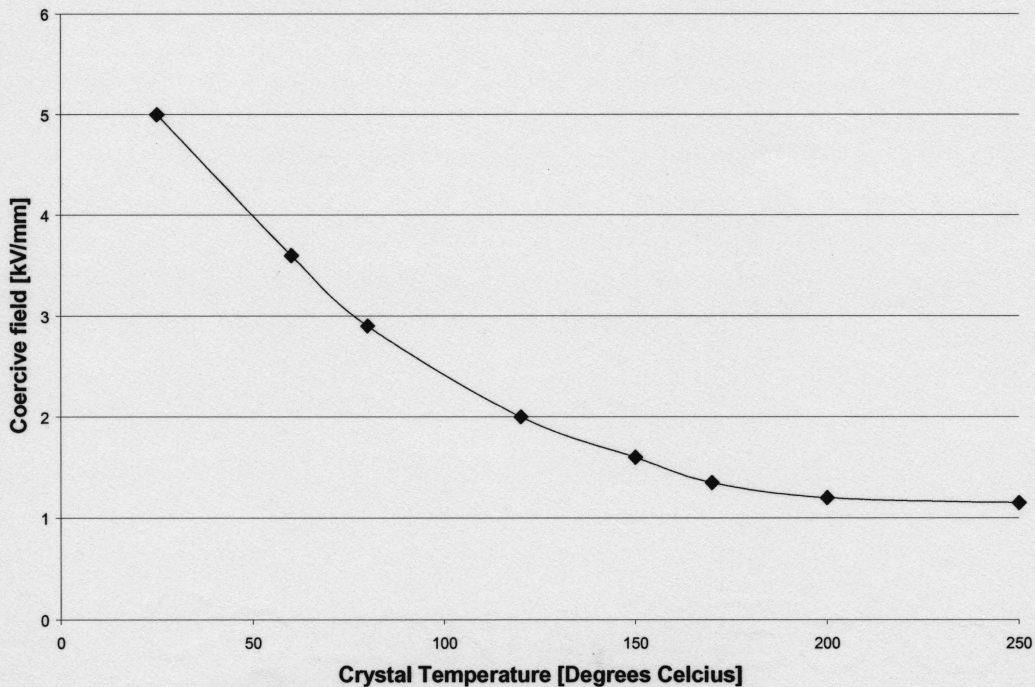


Figure 2.16: Temperature dependence of cohesive field (5% MgO doped) [18].

In periodic poling using patterned electrodes, domain nucleation occurs at the edges of the electrodes, after which the inverted domains progress both inward and outward from the edge of the electrode. The six steps of domain kinetics can be seen in Figure 2.17.

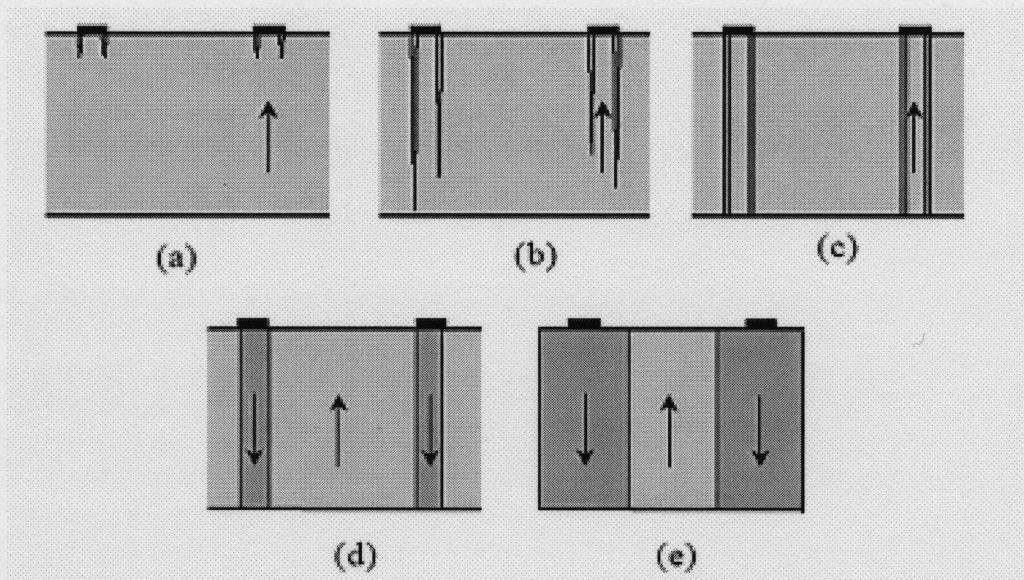


Figure 2.17: Six stages of domain kinetics during electric field poling. (a) Domain nucleation at the electrode edges. (b) Domain tip propagation toward the opposite face of the crystal. (c) Termination of the tip at the opposite side of the crystal. (d) Rapid coalescence under the electrodes. (e) Propagation of the domain walls out from under the electrodes and stabilization of the new domains [19].

The periodic influence of the electrodes is only felt for the first 10 μm of the domain growth [20]. Past this depth the electric field is uniform perpendicular to the surface of the crystal surface. This stems from the high dielectric constant of the material and the relatively small period in comparison to the thickness of the crystal wafer. In the region of uniform field, domain propagation kinetics is the key processing issue. As the domains propagate through the crystal they also spread laterally. The relative rate of spreading to domain propagation is dependent on the duty cycle and period of the anode

grid as well as the electric field applied [20]. This makes the choice of anode duty cycle a complex one that often requires some trial and error.

2.6 Photorefractive effect

The photorefractive effect (or optical damage) is a nonlinear optical effect seen in certain crystals and other materials that respond to intense light by altering their refractive index. How the refractive index is affected by an electric field can be expressed as follows

$$\frac{1}{n^2} = \frac{1}{n_0^2} + rE + RE^2 \quad (2.6)$$

In the photorefractive effect, the applied fields are not the fields of the light, but are electric fields due to rearranged charges in the material. In lithium niobate the charges that get rearranged are electrons. These electrons are localized (the crystal is an insulator) unless something gives the electron enough energy to (at least temporarily) join the conduction band. The excited electron will travel through the crystal (over short distances) until it is trapped again at some other impurity site. An absorbed photon can provide this energy, so regions of the crystal that are illuminated will eventually ‘lose’ their extra electrons as they get stuck in dark regions of the crystal. If the excited electron stops at an impurity in the bright region, it will eventually be excited again. If it is in the dark region, no photon will excite it, so it stays there. After a while, a charge distribution is formed that mimics the profile of the light intensity. The non-uniform charge

distribution creates a non-uniform electric field in the material which will vary the refractive index through the electro-optic effect.

In lithium niobate the extrinsic defects are mainly due to the presence of impurity ions, such as iron, introduced in the melt during crystal growth. This problem can be minimized by starting the crystal growth with very pure substances or by heat treatments in an oxidizing atmosphere [21]. The intrinsic defects include Li vacancies, and antisite defects (Nb on Li site, NbLi). This type of defect can be reduced by adding Mg^{2+} , or Zn^{2+} ion to the melt a dopant to the congruent $LiNbO_3$. Also, treatments such as the vapor transport equilibration method can be used to modify the composition of congruent crystals to enhance the photorefractive damage tolerance [22].

References for chapter 2

- [1] A. Harada and Y. Nihei, “Bulk periodically poled MgO-LiNbO₃ by corona discharge method,” *Applied Physics Letters* **69** (18), 2629-31 (1996).
- [2] T. Suhara and M Fujimura, “Waveguide Nonlinear-optic Devices,” Springer, New York (2003).
- [3] M. Weber, “Handbook of Laser Science and Technology Vol. 3: Optical materials Part1: Nonlinear Optical properties/Radiation Damage,” CRC Press, Inc., Florida (2000).
- [4] J. A. Armstrong, N. Bloembergen, J. Ducuing, and P. S. Pershan, “Interactions between light waves in a nonlinear dielectric,” *Phys. Rev.* **127**, 1918 (1962).
- [5] A. Yariv, “Optical Electronics in Modern Communications,” Oxford University Press, New York (1997).
- [6] M. M. Fejer, G. A. Magel, D. H. Jundt *et al.*, “Quasi-phase-matched second harmonic generation: tuning and tolerances,” *IEEE Journal of Quantum Electronics* **28** (11), 2631-2654 (1992).
- [7] B. Jaskorzynska, G. Agriddson, F. Laurell: Periodic structures for phase-matching in second harmonic generation in titanium lithium niobate waveguides,” *Proc. SPIE*, **651**, 221-228 (1986).
- [8] Y. Zheng, “Domain structures and etching morphologies of lithium niobate crystals with different Li contents grown by TSSG and double crucible Czochralski method,” *Crystal Research and Technology*, **39**, 387– 395, (2004).
- [9] S. Miyazawa, “Ferroelectric domain inversion in Ti-diffused LiNbO₃ optical waveguide,” *J. Appl. Phys.*, **50**, 4599-4603, 1979.
- [10] T. Suhara, H. Nishihara; “Theoretical analysis of waveguide second harmonic generation phase matched with uniform and chirped gratings,” *IEEE J. Quantum Electron.*, **26**, 1265-1276 (1990).
- [11] M. Yamada and K. Kishima, “Fabrication of periodically reversed domain structure for SHG in LiNbO₃ by direct electron beam lithography at room temperature,” *Electron. Lett.* **27**, 828-829 (1991).
- [12] M. Yamada, N. Nada, M. Saitoh, and K. Wananabe, “First-order quasi-phase matched LiNbO₃ waveguide periodically poled by applying an external field for efficient blue second-harmonic generation” *Appl. Phys. Lett.* **62**, 435-436 (1993).

- [13] B.C. Grabmaier, F. Otto, "Growth and investigation of MgO-doped LiNbO₃," *J. Crystal Growth*, **79**, 682 (1986).
- [14] D. A. Bryan, Robert Gerson, and H.E. Tomaschke, "Increased optical damage resistance in lithium niobate," *Appl. Phys. Lett.* **44**, 847 (1984).
- [15] V. Shur, and M. Feger, "Domain kinetics in congruent and stoichiometric lithium niobate," *Ferroelectrics*, **269**, 189-194 (2002).
- [16] A. Rauber, "Current topics in material science," **1**, ed. E. Kaldis, Amsterdam: North Holland, 481-601, (1978).
- [17] J. H. Ro, M. Cha, "Subsecond relaxation of internal field after polarization reversal in congruent LiNbO₃ and LiTaO₃ crystals," *Appl. Phys. Lett.*, **77**, 2391-2393 (2000).
- [18] H. Ishizuki, I. Shoji, and T. Tiara, "Periodical poling characteristics of congruent MgO:LiNbO₃ crystals at elevated temperature," *Appl. Phys. Lett.* **82**, 4062-4064 (2003).
- [19] Gopalan, Terence E. Mitchell, "Wall velocities, Switching times, and stabilization mechanism of 180° domains in congruent LiTaO₃ crystals" *J. Appl. Phys.*, **83**, 941-954, (1998).
- [20] K. Nakamura, J. Kurz, K. Parameswaran, and M. Fejer, "Periodic poling of magnesium-oxide-doped lithium niobate," *J. Appl. Phys.* **91**, 4528-4534 (2002).
- [21] A. M. Glass, "The photorefractive effect," *Opt. Eng.*, **17**, 470, (1978).
- [22] C. Q. Xu, H. Okayama, and Y. Ogawa, "Photorefractive damage of LiNbO₃ quasi-phase matched wavelength converters," *J. Appl. Phys.* **87**, 3203, (2000).

CHAPTER 3: EXPERIMENTAL APPARATUS AND PROCEDURES

This chapter presents the processing, analysis, and apparatus used for fabricating a 17.7 μm period MgO:PPLN over a 12 mm diameter grating. MgO:PPLN fabrication with uniform domain pattern quality permits fabrication of devices 10 mm in length. This chapter first describes the experimental apparatus, emphasizing the relevance for some of the choices made in the design of the apparatus. The various procedures are discussed next, including details on the domain inversion process. Finally, the analysis of periodic domain inverted materials is described.

3.1 Experimental apparatus

There are three major components of the corona poling system. The corona torch provides the discharge used to charge the $-z$ surface of the crystal. The crystal holder provides the ground connection to the anode grid. This metal support is insulated from all other metal grounds so that current flowing through it may be measured via a data acquisition card. The crystal holder also controls the temperature of the crystal by using 2 resistive heaters that are also insulated from ground. The last major function of the crystal holder is to support the crystal while providing a high vacuum region beneath it. Both the corona torch and crystal holder are contained in a glass environmental chamber. Dimension drawings for all major components can be found in Appendix A.

3.1.1 Environmental chamber

The crystal holder and corona torch are contained inside an 8 liter Pyrex glass environmental chamber. The environmental chamber is filled with nitrogen gas that allows for greater control and reproducibility of discharge and material processing parameters. Figure 3.1 shows a photograph of the actual environmental chamber. Figure 3.2 shows a schematic of the entire corona torch domain inversion processing system.

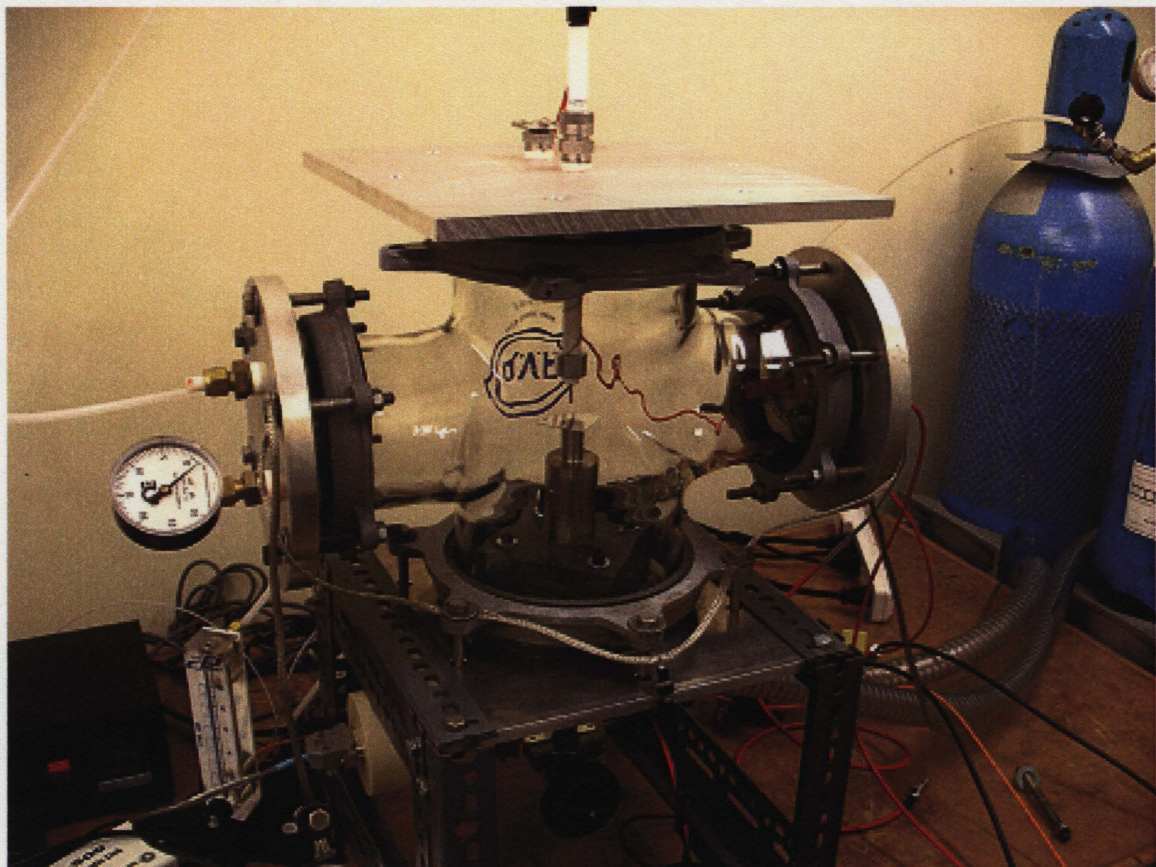


Figure 3.1: Photograph of environmental chamber with corona torch system.

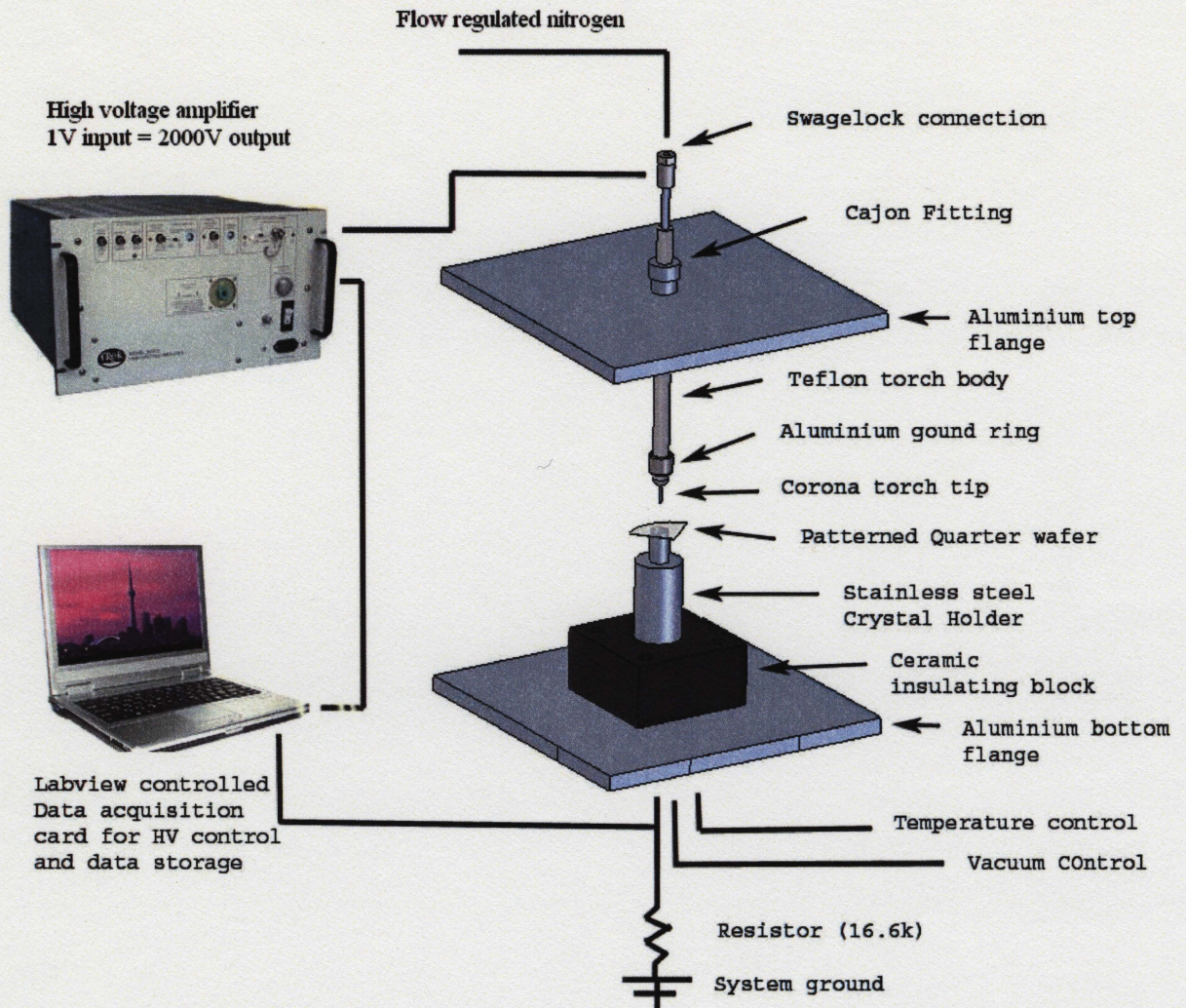


Figure 3.2: Schematic of corona torch domain inversion processing system.

3.1.2 Crystal Holder

The crystal is supported in the environmental chamber by a stainless steel tube. The 16 mm OD and 12 mm ID of the support structure matches the pattern deposited on the (+z) surface (ground side) of the crystal. This structure supports the crystal 140 mm above the chamber base and also functions to heat the crystal, connect the anode pattern to ground, and provide a high vacuum region below the crystal.

The vacuum system provides adequate force to ensure good contact between crystal and crystal holder. This good contact between crystal and crystal holder also enhances heat transfer between the holder and the crystal surface. Thermal imaging measured by an infrared camera (ThermalCAM SC3000) has shown that the crystal is able to heat up quickly, uniformly, and accurately to the desired temperature. The electrical discrimination of the anode grid was also enhanced by the presence of the vacuum beneath the crystal surface. The pressure beneath the crystal ranged between 10^{-3} and 10^{-4} Torr during processing.

Figure 3.3 shows the exploded view of the crystal holder as well as the assembled view with the crystal in place. The ceramic block is used to insulate the crystal holder from the base flange. This is for grounding and thermal reasons. In order to measure the current flowing to the grounded crystal holder, it must be insulated from the protective grounding used for all chamber flanges. Also the ceramic block reduces the heat loss to the base flange because it is less thermally conductive than aluminum. The three major components shown in Figure 3.3 have been precisely machined to maintain a high vacuum seal between the crystal surface and the vacuum pump.

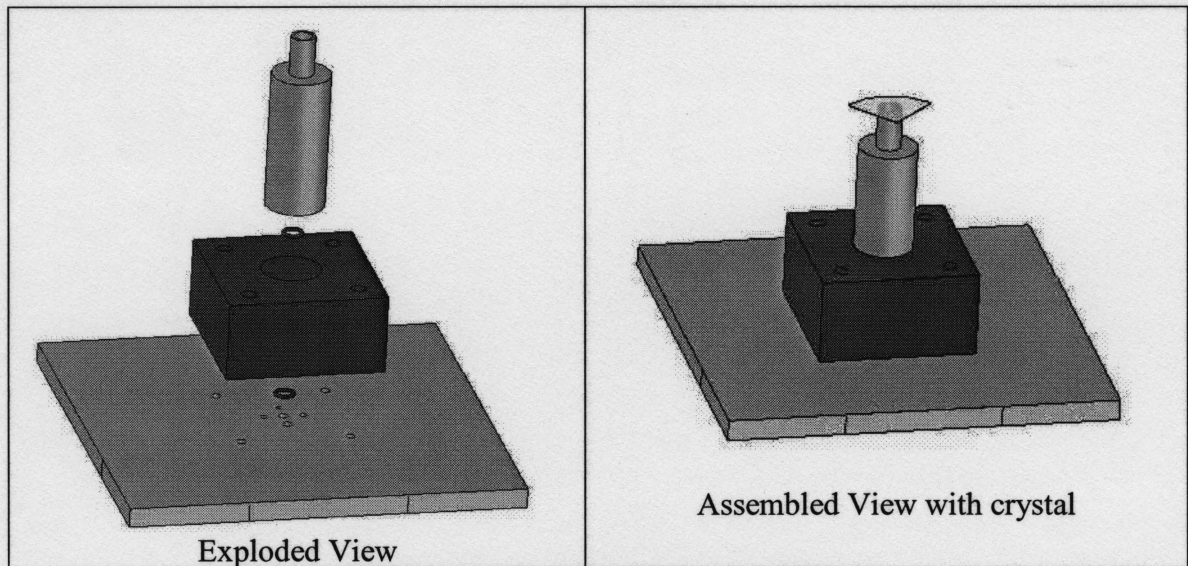


Figure 3.3: Schematic of crystal holder.

3.1.3 Corona torch

The corona torch is translated in a 12.7 mm (1/2") Cajon fitting positioned in the center of the top flange of the environmental chamber. This type of connection allowed for variability of corona torch position relative to crystal surface. The high voltage is insulated from the grounded flange by a (12.7 mm OD by 6.35 mm ID) Teflon tube. Inside the Teflon tube the stainless steel tube is stepped down in diameter. Figure 3.4 shows a schematic of the corona torch.

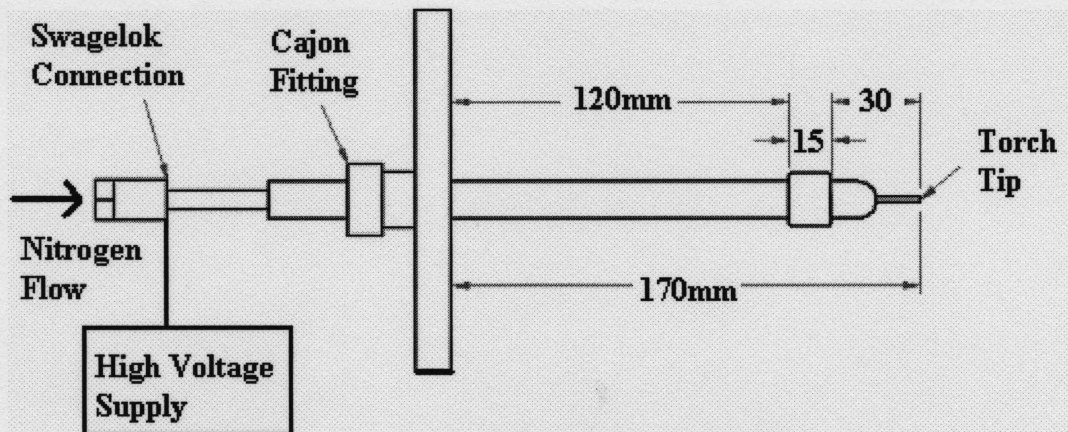


Figure 3.4: Schematic of corona torch.

Figure 3.5 shows how the corona torch is assembled. First the two stainless steel tubes of different diameter (6.35 mm OD with 5.35 mm ID to 2.00 mm OD with 1.50 mm ID) were mated with silver solder and inserted into a larger Teflon tube. A Teflon made end cap and a steel Swagelok pipe connector were added.

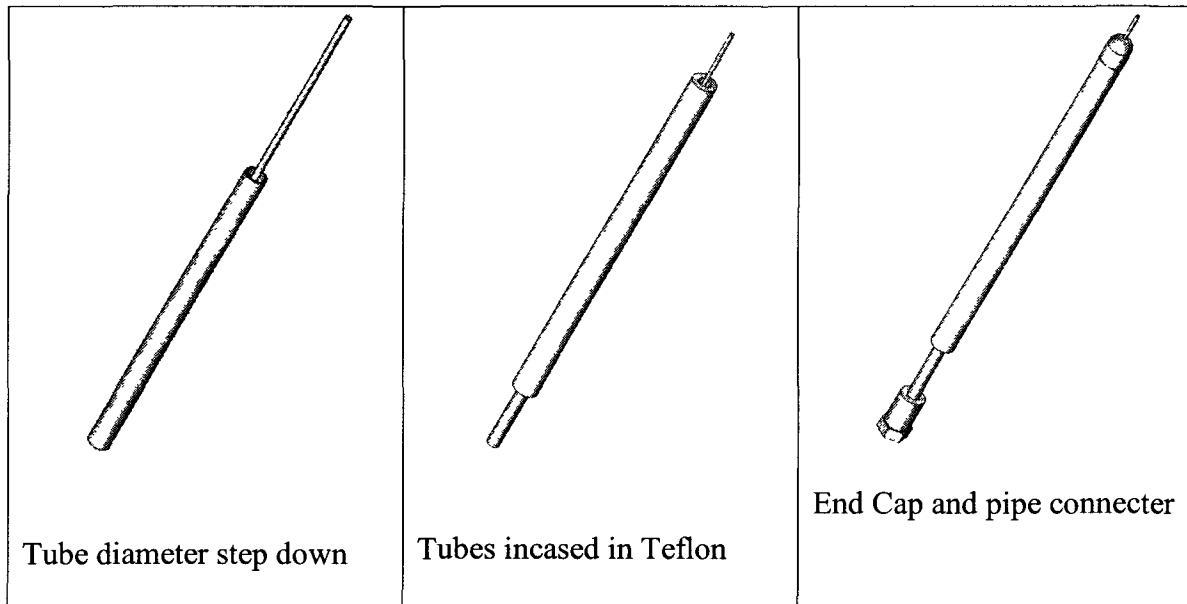


Figure 3.5: Corona torch assembly procedure.

An electrically grounding ring electrode was placed outside the Teflon insulator as shown in Figure 3.6. Two types of ground electrodes were tested, one is made by an aluminum ring rounded at all edges and the other was a thin brass sleeve as shown in Figure 3.6. The functional importance of these grounding rings is only significant when used without the presence of the crystal and grounded holder.

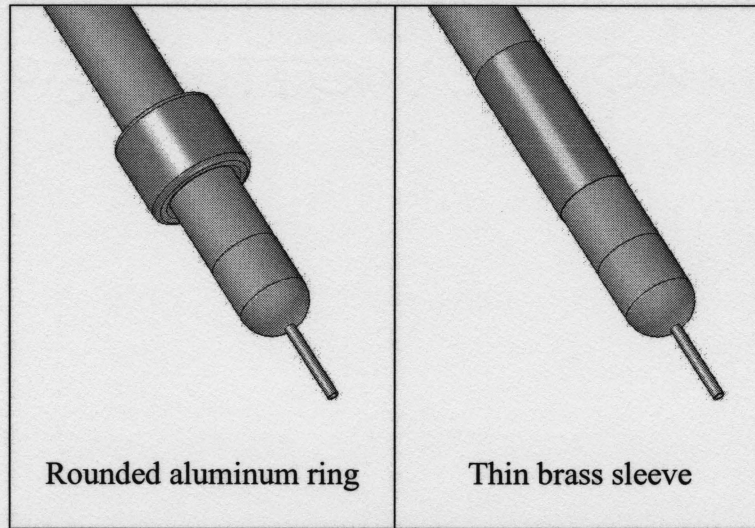


Figure 3.6: Two types of corona torch ground ring electrodes.

3.2 Experimental procedures

This section will outline the various procedures performed in crystal preparation and material processing. First the crystal substrates have a metallic anode grid deposited on the (+z) surface and the wafers are diced into four identical quarters. After dicing, some pieces were submitted to a proton exchange treatment before the domain inversion process was performed. This treatment was performed to see if it had any effect on the rate of horizontal domain spreading during the poling process.

3.2.1 Chrome deposition

The (+z) face of an optical grade *z*-cut 5% MgO:LiNbO₃ wafer was lithographically patterned using the lift-off technique, with a periodic array of sputtered chrome stripes with the grating *k* vector parallel to the crystallographic *x*-axis. The majority of the wafers were made by Huaying Electronics (China) and Soshin Electric (Japan). The wafers had a 500- μ m nominal thickness with a 76.2 mm diameter.

Pure chrome was used because it has been reported to provide excellent nucleation site density [1]. The (+z) face was chosen because a negative corona discharge was used for the domain inversion. The chrome stripes were 200 nm thick, 2.5 μm wide, and had a period of 19.1 μm . Although a 50% domain duty cycle is preferable, the lower duty cycle was chosen to reduce the coalescence of domains between the electrodes.

3.2.2 Dicing quarter wafers

In order to reduce the cost per trial associated with domain inversion attempts, the 76.2 mm diameter crystal was cut into 4 separate quarter pieces. Further size reduction was not reasonable due to the significant influence of edge effects on the discharge characteristics of the corona torch. A chrome-patterned wafer after dicing can be seen in Figure 3.7. From this 4 quarter cut wafers each with a circular metalized grating are separated.

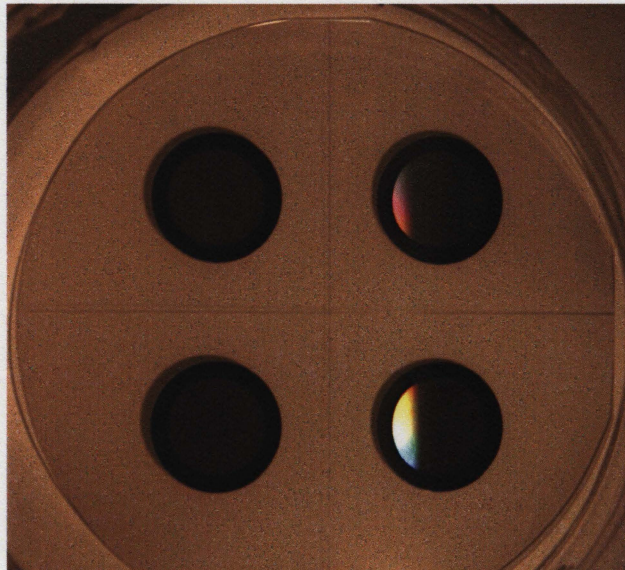


Figure 3.7: Quarter wafer with 12mm diameter anode pattern.

3.2.3 Proton Exchange Treatment

In order to achieve a proper domain profile proton exchange treatment can be employed to reduce the horizontal domain spreading [2]. Proton exchange is a method typically used to change the refractive index of the crystal in the formation of waveguides. In this case, the metalized anode stripes function as a mask protecting the regions underneath the electrodes from the proton exchange treatment. After treatment the zones between the anode stripes function to inhibit side growth during the domain inversion process. The proton exchange treatment is achieved by submersing the crystal in benzoic acid for 2 hours at 200 °C. The (-z) surface of the crystal must be protected during the proton exchange process. It was observed that proton exchange treatment of the (-z) surface contributed defects that destroyed the uniformity of the corona processing. This protection is achieved by depositing Al on the (-z) side of the wafer. After the proton exchange treatment, the Al layer is then removed by phosphoric acid.

3.2.4 Domain inversion process

All the steps involved in crystal domain inversion are listed below.

1. First the crystal holder is preheated to 50 °C.
2. During the preheat process both sides of the crystal are cleaned with acetone. Compressed air is also used to make sure no dust resides on either surface of crystal.
3. The crystal is placed on the crystal holder with the anode ring matching the surface of the holder.

4. Further heating of the crystal is done in 10 °C increments. The entire heating process to 90 °C should be done over the course of 1 hour. This gradual heating reduces the risk of thermal stress breaking the crystal
5. Once the desired temperature is reached the vacuum system can be switched on. This is done after heating so that thermal expansion does not break the crystal.
6. Nitrogen flow through the corona torch is fixed to 4 L/min for 10 minutes in order to remove the majority of impurities in system and maintain consistent process humidity and gas parameters.
7. Nitrogen flow through the corona torch is set to desired level for processing.
8. Processing parameters are then set in LABVIEW.
9. The high voltage amplifier is switched on.
10. The LABVIEW program is initiated.

The discharge appears as a faint pink glow at the tip of the corona torch. In some cases the intended domain inversion region will also glow faintly. Visual inspection of the corona is important in recognizing any non-ideal discharge parameters both at the torch tip and the crystal surface.

3.3 Analysis of periodic domain inverted materials

3.3.1 Characteristics of periodic domain inversion

To evaluate how domain characteristics affect conversion efficiency, the relevant factors must be investigated. Equation 3.1 shows all the relevant terms related to the irradiance of the second harmonic [3].

$$I^{2\omega}(L) \propto \frac{d_{33}}{\pi} \sin^2\left(\frac{a}{a+b} m\pi\right) [E^\omega]^2 L^2 \text{sinc}^2\left(\frac{\Delta k L}{2}\right) \quad (3.1)$$

where $I^{2\omega}$ is the irradiance of the second harmonic, d_{33} is the nonlinear coefficient, m is the order of the grating, a and b are widths of inverted and non-inverted domains respectively, E^ω is the electric field of the fundamental light wave, L is the device length, and Δk is the phase mismatch.

In order to evaluate what is relevant to the quality of domain inversion equation 3.1 must be simplified. The first term can be removed if the assumption is made to use first order quasi-phase matching. This is a fair assumption because it is the most efficient order of quasi phase matching. The E^ω term is a function of the pumping source and the ability of the light to be confined to a small area. The period of grating must also be assumed to correctly match the pump source, and thus $\Delta k = 0$. The factors relevant to the quality of the domain inverted gratings then becomes

$$I^{2\omega}(L) \propto \sin^2\left(\frac{a}{a+b} m\pi\right) L^2 \quad (3.2)$$

The characteristics of domain inversion quality that relate to the conversion efficiency of the device are grating length and domain duty cycle. The domain duty cycle refers the ratio of inverted to non-inverted domain width. The output irradiance is

proportional to the length of the device squared. For this reason the process must be uniform over large areas so that devices of adequate length and width can be fabricated with the highest efficiency possible. The remaining term deals with the efficiency with respect to domain duty cycle. Device efficiency is maximized for domain duty cycles of 50%. Any irregularities in the boundary position or domain duty cycle will reduce the overall efficiency of the device.

3.3.2 Initial visual inspection

After the actual domain inversion process some of the domain characteristics can be observed by the naked eye. At a certain orientations the reflected light from the grating can be visualized. The grating in the material that can be seen because of the periodic index change associated with domain boundaries. The refractive index of the boundary layer is not the same as that of the actual domains so the device functions as a grating to incident light. This method can reveal uniformity issues and the correct poling time.

3.3.3 Domain inspection via etching

The domains can be evaluated much more accurately via wet etching in HF. The orientation of the domain polarization has a significant effect on etch rate and thus will present the domain boundaries after only a few minutes.

3.3.4 Domain inspection via cross sectional etching

Dicing and polishing the crystal and etching the cross section of the domain boundaries can further evaluate the domain quality. This confirms the verticality of domains a gives a clear view of domain profile. Domain analysis on (-z) and (+z) surfaces match with analysis done on the cross section. Figure 3.8 shows that the domains duty cycle exposed by the cross-section matches the duty cycle exposed at the (+z) and (-z) surfaces.

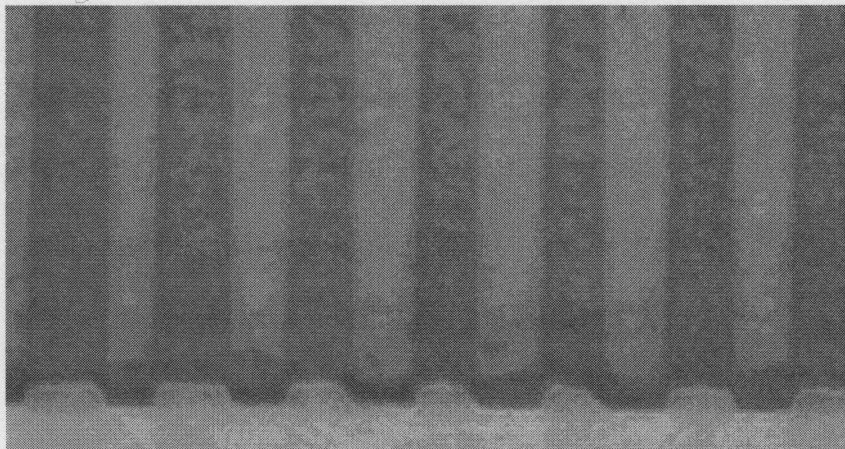


Figure 3.8: Domain analysis via cross-sectional etching in HF.

3.3.5 Quantitative analysis techniques for domain inverted crystals

In order to optimize the domain inversion process, quantitative image analysis must was performed. High-resolution images were captured though a microscope and stored using a digital camera. The microscope has 3 setting with 3 different resolutions. Table 3.1 shows the resolutions stated by the microscopes manufacturer.

Table: 3.1 Microscope Resolutions (Nikon E200)

| Microscope Setting | Resolution |
|--------------------|--------------------|
| 4X | 2.75 μm |
| 10X | 1.10 μm |
| 40X | 0.42 μm |

The limiting factor in the overall resolution of the system is the microscope. The digital camera pixel density far exceeds what is required. The images are converted to the bitmap format so they can be analyzed using a software package called HL Image++. The domain duty cycle exposed through the etching process can be consistently evaluated between different domain inversion trials. Figure 3.9 shows a typical image being evaluated and Figure 3.10 shows the resulting gray level pixel information.

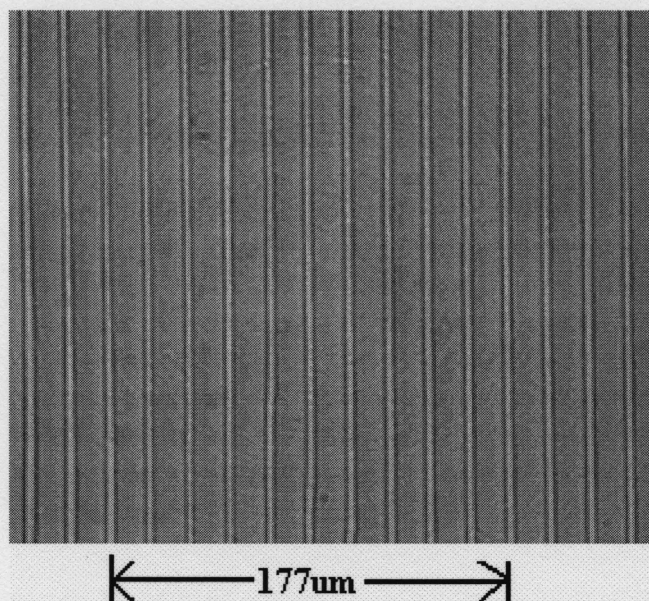


Figure 3.9: Image of typical domain inverted structure after etching by HF.

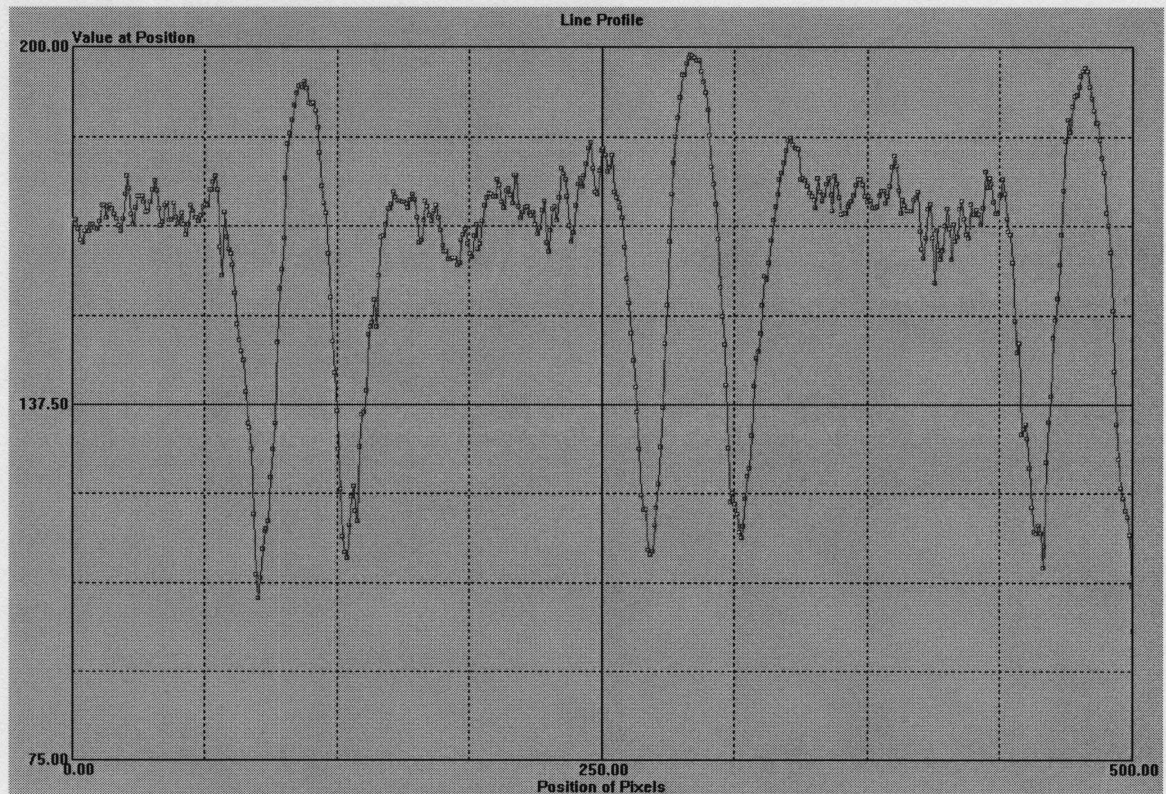


Figure 3.10: Typical pixel analysis for determining domain duty cycle.

Figure 3.10 shows the gray level intensity (y-axis) of a horizontal cut line analysis (x axis) taken from the middle of the image shown in Figure 3.9. The duty cycle of the inverted grating can be calculated by comparing the inverted domain width and the total width of grating period. These measurements are done via software aided pixel counting. The ratio of measured pixels is then multiplied by the known period of the grating to get the true domain width in [μm]. In Figure 3.9 the narrow bright regions represent domains that have been inverted. For consistency purposes the edges of the domain wall are used as the measurement points. It is assumed that the domain edges correspond to the greatest change in gray level pixel intensity. In order to conduct this measurement using HL Image++ the typical gray level pixel intensity along the x-axis shown in is converted

to the derivative of pixel gray level intensity (di/dx). This makes the actual measurement process faster and more accurate. Figure 3.11 shows the gray level pixel intensity (red) as well as the derivative of pixel gray level intensity (blue) used for determination of domain duty cycle.

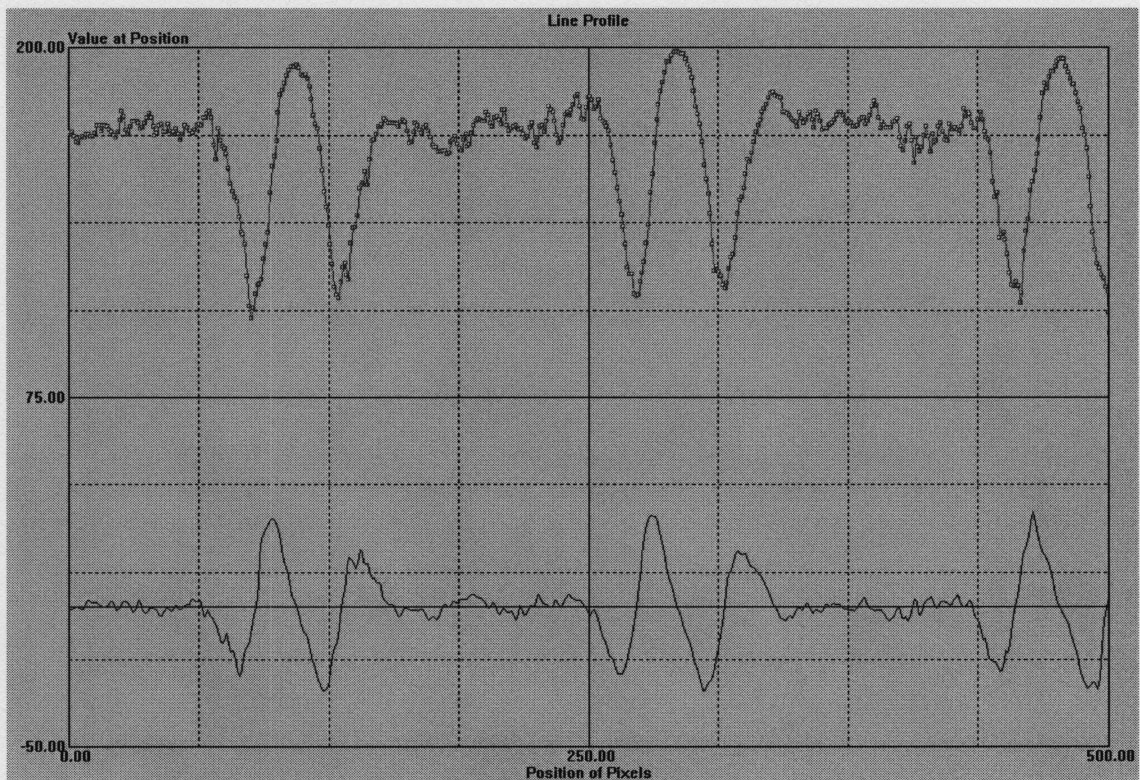


Figure 3.11: Typical derivative of pixel intensity used for determination of domain duty cycle.

By analyzing the data in this manner, the domain width can be consistently measured. In regions with variation in domain width, multiple domain duty cycles were recorded and the average domain width was then calculated.

In order to understand the variation in domain width the accuracy of the measurement method must first be determined. This was performed by comparing the variation in domain widths of a near uniform sample to the variation in grating period.

Figure 3.12 shows pixel lengths of both domain width and grating period. In Figure 3.12 twelve successive measurements were taken across the grating direction.

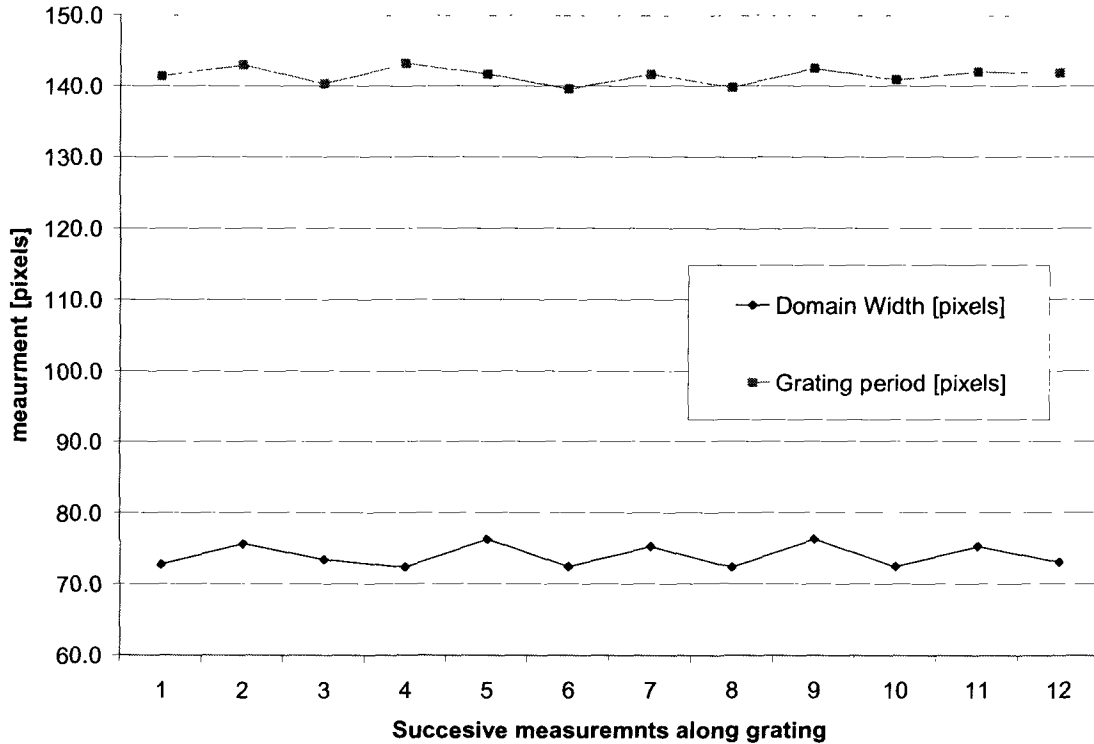


Figure 3.12: Pixel length measurements of both domain width and grating period.

From the data presented in Figure 3.12 the variation in measurements was determined. It was found that for measurements of grating period all values lie between ± 2 pixels or 1.2% of the mean value. For the domain width case all measurements lie within ± 3 pixels or 3.4% of the mean value. This shows that variation in domain width in excess of 3 pixels can be measured using the current techniques. It should be noted that for smaller domain widths the relative error in the measurements increases.

References for Chapter 3

- [1] G. D. Miller, R. G. Batchko, W. M. Tulloch, D. R. Wiese, M. M. Fejer, and R. L. Byer, "42% Efficient Single-Pass cw Second-Harmonic Generation in Periodically Poled LiNbO₃", *Opt. Lett.* **22**, p. 1834-1836 (December 1997).
- [2] S. Grilli, "Control of lateral domain spreading in congruent lithium niobate by selective proton exchange," Accepted by Applied Physics Letters, (2006).
- [3] M. M. Fejer, G. A. Magel, D. H. Jundt, and R. L. Byer, "Quasi-Phase-Matched Second Harmonic Generation: Tuning and Tolerances", *IEEE J. Quantum Electron.* **28**, 2631-2654 (1992).

CHAPTER 4: CORONA TORCH CHARACTERIZATION

The objective of the corona torch charging method for poling is to achieve optimum control of surface charging, which was not achieved by the corona wire method [1]. The use of the flow stabilized discharge corona torch [2] is to ensure adequate surface charge for initiation of the domain inversion process. The corona torch described in Chapter 3 and Appendix A had many variable parameters such as the size of grounding ring, position of grounding ring, extension distance of discharge tube, etc., so that greater control can be achieved.

One important variable in the poling process is related to the crystal. The presence of the grounded crystal and the crystal doping significantly influence the discharge characteristics. The influence of the different corona torch parameters were originally studied without the crystal present. The crystal positioned downstream from the corona torch functions like a ground surface, which drastically changes the discharge characteristics. The corona onset voltage of the corona torch without the crystal positioned beneath is roughly -15kV. The maximum achievable currents are much lower before the initiation of sparking in the case without the crystal present as well.

The crystal doping also has a significant effect on the corona torch characteristics. The 5% MgO doped crystal compared to the pure lithium niobate crystal has a much higher conductivity. This conductivity is due to the reduction of Li vacancies which function as traps for electrons in the conduction band. Figure 4.1 shows the effect of crystal presence on corona torch discharge characteristics, where the crystal was placed 15 mm in front of corona torch. The corona on-set voltage becomes lower when the

crystal is present and the conductivity of the doped crystal also helps to reduce corona on-set voltage. The I-V curves in Figure 4.1 were taken with a flow rate of 4 L/min and the crystals had no metal on the (+z) surface.

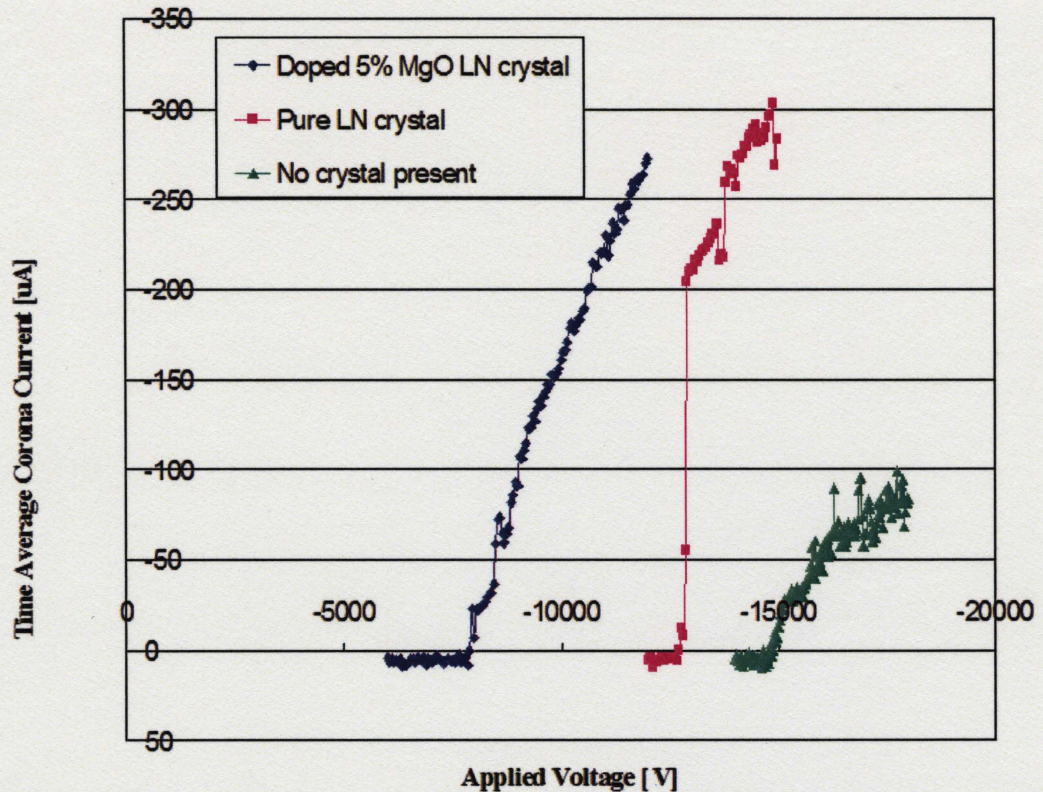


Figure 4.1: Effect of crystal presence on corona torch time averaged discharge current-voltage characteristics.

4.1 Plasma parameters

In order to measure the ion density distribution downstream from the corona torch exit, a floating potential double probe was used [3]. Electrostatic probes are simple devices; however, depending on the plasma environment a suitable theory is required for analyses. Electrostatic probes have the advantage for local measurements where spectroscopy and the other methods measure over integrated large plasma volumes. Most

electrostatic probes function by varying the probe voltage with respect to a known reference and analyzing the I-V characteristics. The problem with employing a probe of this nature is that it requires a steady state plasma discharge and will disturb the plasma environments.

4.1.1 Double probe method

The double probe method was originally proposed by Johnson and Malter [4]. This device was developed to measure afterglow plasmas, in which the plasma potential changed with time, so that it was difficult to maintain a constant probe-plasma potential difference. With two probes biased with respect to each other but insulated from ground, the entire system “floats” with the plasma and therefore follows the change in plasma potential [5]. This device functions by providing a DC electric potential between two small wires biased with respect to each other and insulated from ground. The double probe is immersed in a plasma region and current flows between the two probes. The current flow through the double probe is proportional to the ion density, N_i , in the region between the wires and mobility of the charge carriers present in that region based on continuum theory [3]. A schematic of the circuit used is shown in Figure 4.2.

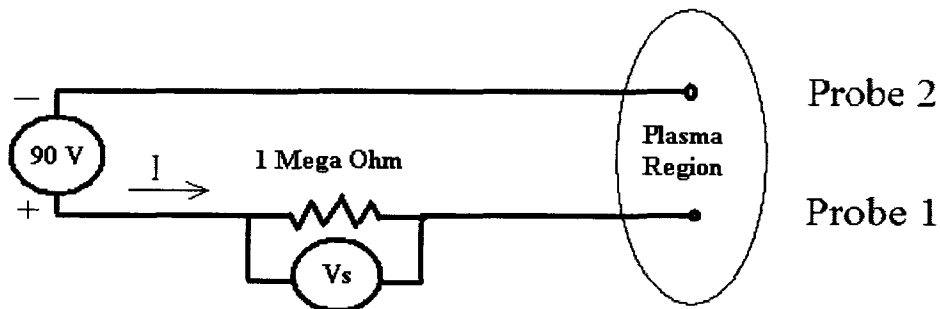


Figure 4.2 Circuit diagram of double probe.

A current flow through the double probe is positive when the applied bias is positive. Figure 4.3 shows the potential distribution between the probes. Figure 4.4 shows a typical probe current-voltage characteristic.

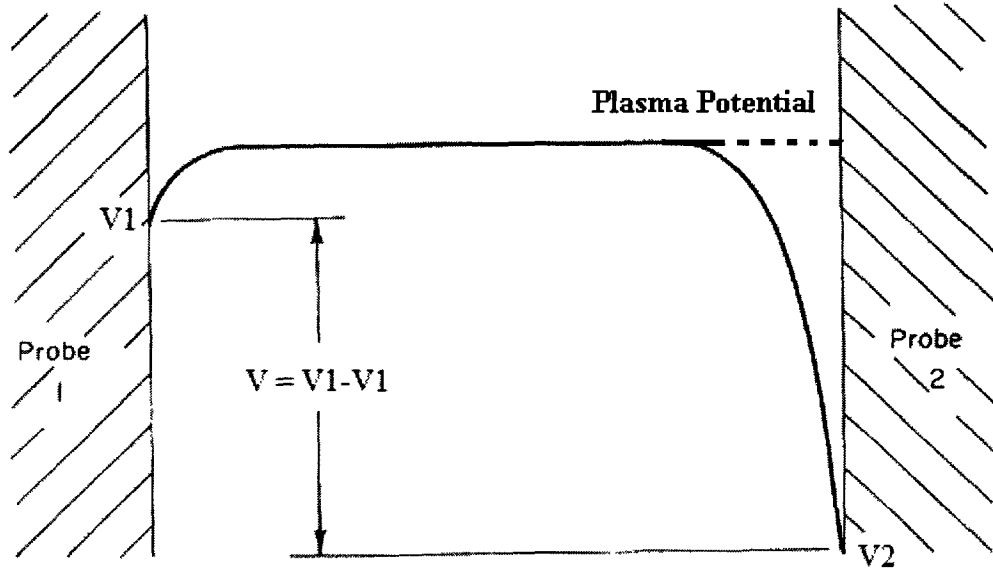


Figure 4.3: Schematic of potential distribution between the probes of a floating potential double probe system [5].

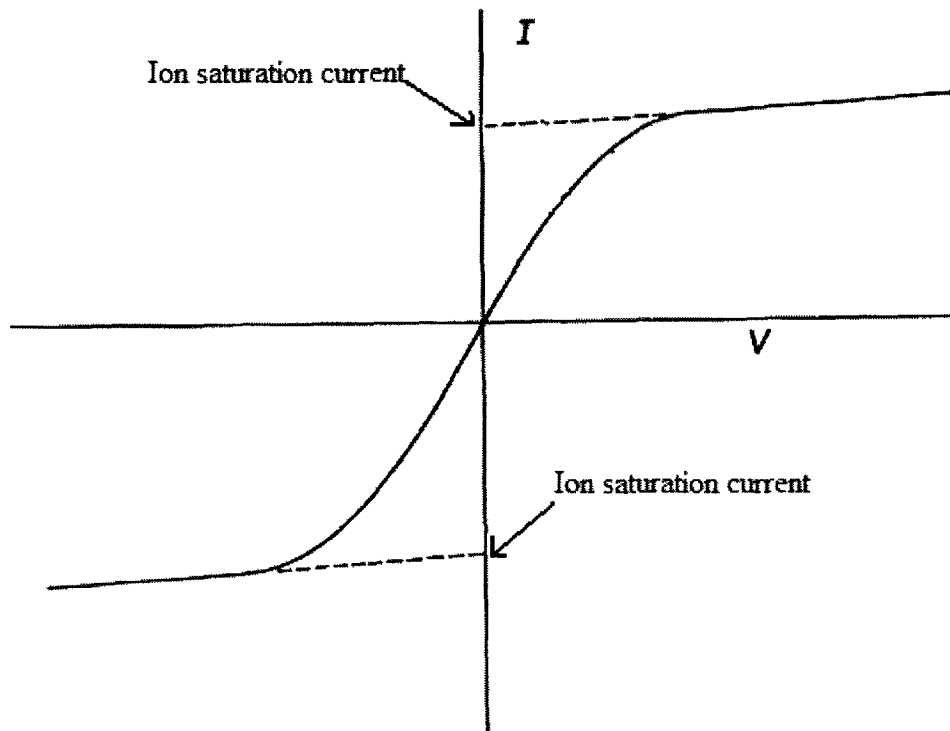


Figure 4.4: Schematic of a double probe I-V characteristic with symmetric probes [5].

Figure 4.4 reveals an important advantage of the double probe method. The total current of the system can never exceed the saturation ion current because the ion and electron saturation currents must always be balanced. For this reason, the disturbance to the plasma environment is minimal. The main disadvantage of this method is that part of the electron, negative ion and positive ion energy distribution is not sampled and hence electron or ion temperatures obtained may not be accurate.

One of the basic assumptions made in the present double probe operation is that the probes are sufficiently negatively biased to be collecting ion saturation current at the applied voltage. If the I-V characteristics were taken as in Figure 4.4 and plotted, the slope of the line at $V = 0$ would be proportional to the electron or ion temperature. The ion density can be obtained from equation 4.1 [3].

$$N_i = \frac{I^{sat} R_p}{e D^i S} \quad (4.1)$$

where I^{sat} is the saturation current, R_p is the probe radius, D^i is the diffusion coefficient, and S is a shape constant given by $S = 4\pi R_p^2 L / \ln L$ for a cylindrical probe [3] where L is the length to diameter ratio.

4.1.2 Ion density distribution

The double probe was positioned in different locations downstream of the corona torch tip in order to measure the ion density distribution. Figure 4.5 shows a schematic of double probe ion density profile. The corona torch was set to a constant discharge voltage 17.7 kV and nitrogen flow rate of 3 L/min. The ground ring was fixed at 30 mm above the edge of the corona torch hollow electrode which drove the torch with a constant current of 150 μ A. It was observed that the position of the ground ring influenced the corona current but did not significantly alter the ion density distribution.

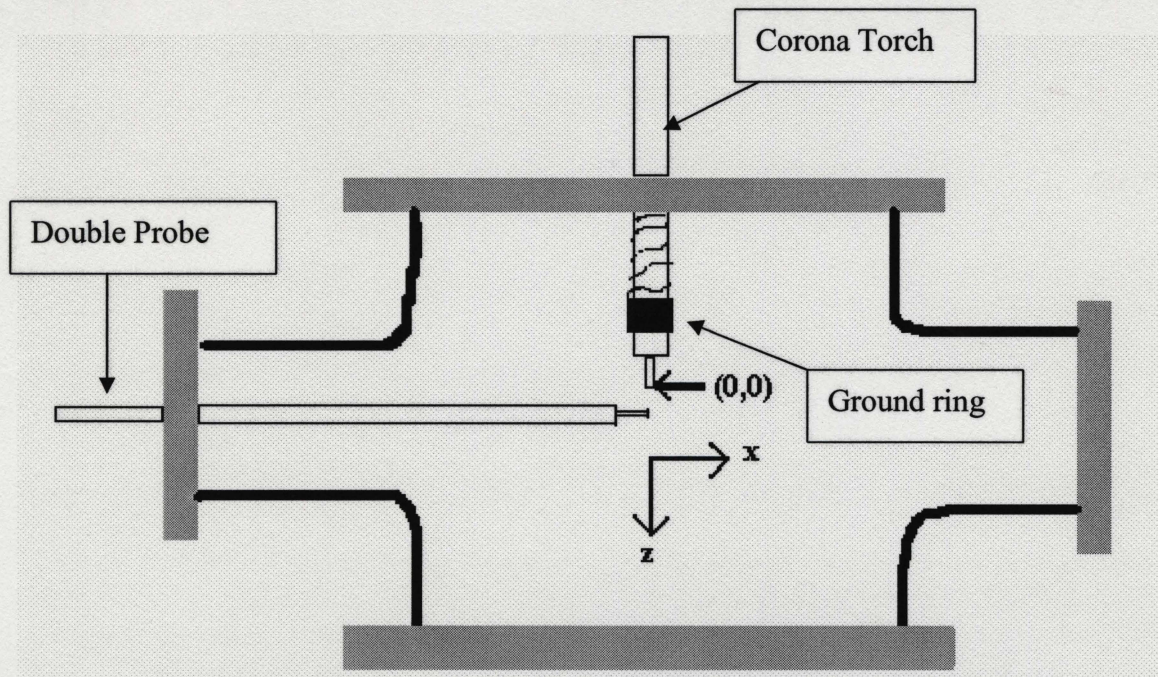


Figure 4.5 Schematic of double probe plasma profile measurement.

The gas flow rate of the corona torch was not observed to influence the distribution of the ion density. The gas flow rate affected the magnitude of the corona torch discharge current and its waveform only at flow rates below 2 L/min. For this reason, the ion density and distribution was studied at 2 L/min. Figure 4.6 shows the ion density profile below the gas flow exit of the corona torch. From Figure 4.6 it is clear that the ion density decreases with increasing distance from the corona torch gas exit.

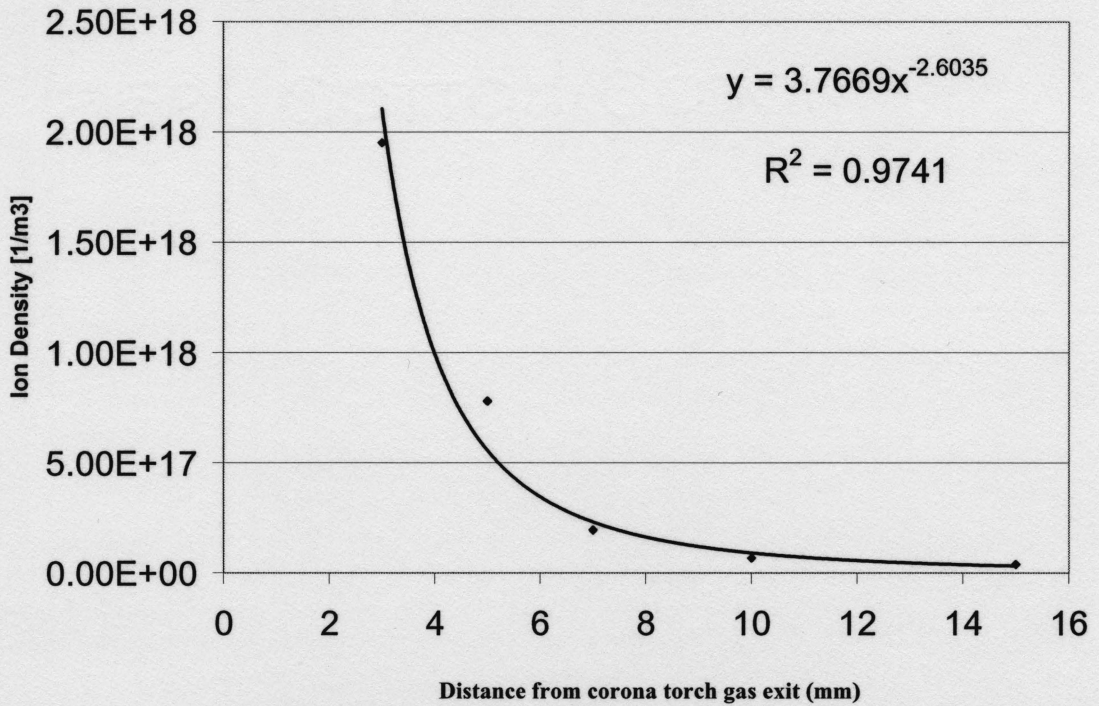


Figure 4.6: Ion density profile along gas exit axis.

Figure 4.7 shows the ion density distribution contour lines downstream of the corona torch. From Figure 4.7 shows that the radial direction distribution of ion density becomes more uniform as the axial z-direction distance is increased. This suggests that greater process uniformity may be achieved by increasing the spacing between the corona torch and the lithium niobate crystal.

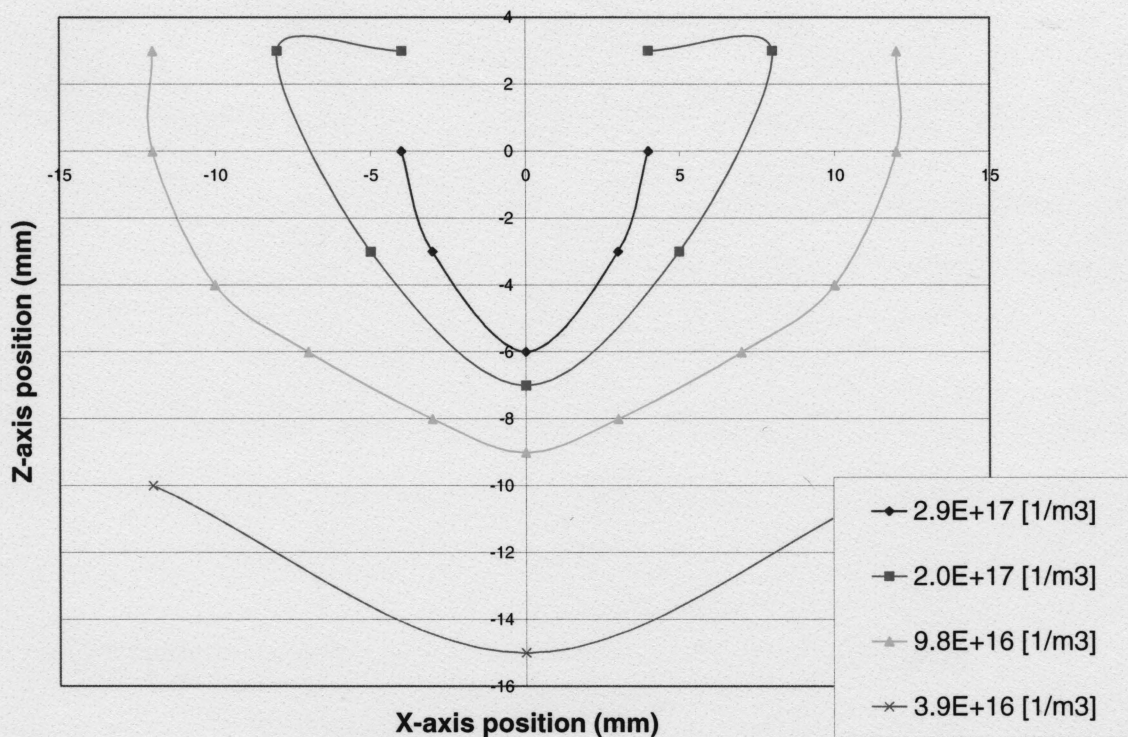


Figure 4.7: Ion densities vs. Position in 2D.

Due to the nature of the discharge the double probe current-voltage characteristics, similar to those shown in Figure 4.4, were not obtained. The double probe electrode spacing was minimized as much as possible and the floating DC bias was increased from 0 - 90 V. The corona torch grounding ring and applied voltage was set to yield the maximum corona current possible. Measuring the characteristics of the negative DC corona, by double probe method, is difficult since nitrogen is a non attaching gas and easily sparks over between the corona torch and the probes. The double probe current-voltage characteristics as shown in Figure 4.4 require both the presence of positive ions and electrons or negative ions to obtain an ion density measurement.

4.1.3 Optical emission spectroscopy background

Emission spectroscopy is a non-disturbing method used to investigate plasma parameters such as the identification of molecules, vibrational and rotational temperatures, electron and ion densities, etc. During a corona discharge in nitrogen, the molecules are transferred from the ground state into the excited or ionic state by collision with energetic electrons. After that, the excited and ionized molecules transit into their ground and metastable states by emitting radiation of a specific wavelength. The emitted line spectra contain information about the electron energy and density. For example, the nitrogen molecule can be transferred from the ground state ($X^1\Sigma_g^+$) into the excited state ($C^3\Pi_u$) by the impact of electrons with energy greater than 11 eV. In the radiative emission process the ($C^3\Pi_u$) electrons will transfer into the ($B^3\Pi_g$) state by emitting a photon with a wavelength of 337.1 nm. Figure 4.8 shows the energy potential curves for N_2 in the range from 6 to 12 eV.

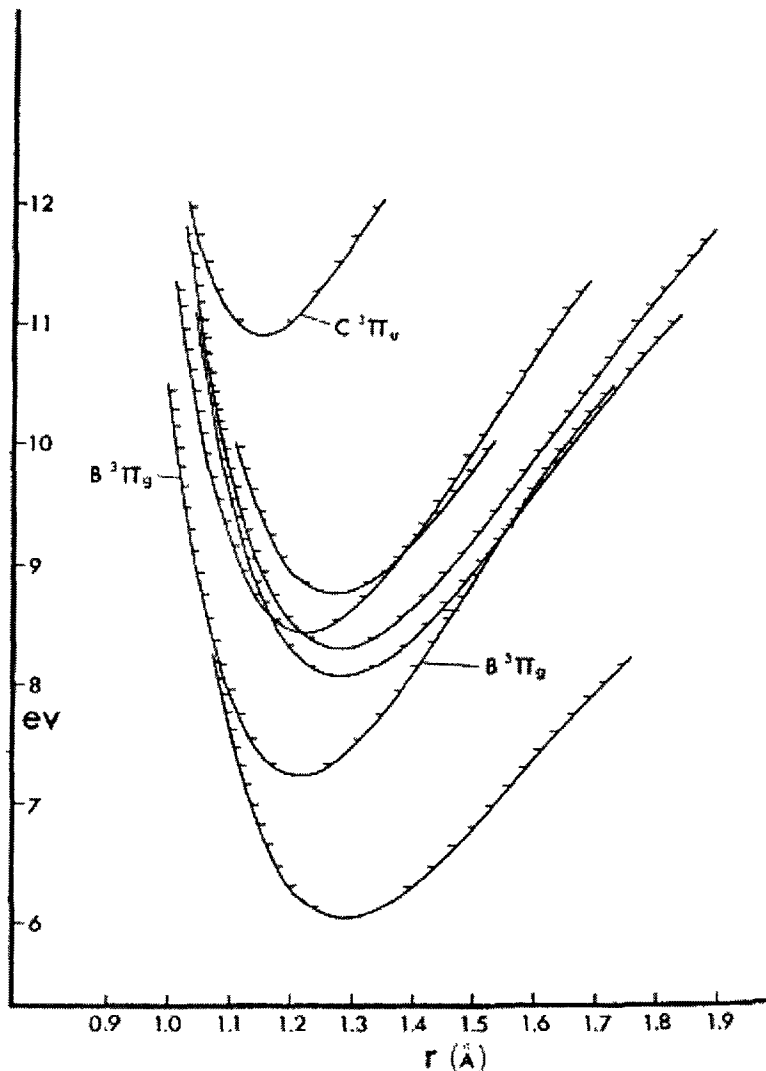


Figure 4.8: Potential curves for N_2 in the range from 6 to 12 eV [6].

In general the band intensity is given as [7]

$$I_{v'v''} \propto N_{v'} A_{v'v''} \nu_{v'v''}^4 \quad (4.2)$$

where $I_{v'v''}$ is the band intensity for a transition between vibrational energy levels $E_{v'}$ and $E_{v''}$ of the nitrogen molecule $C^3\Pi_u(v')$ and $B^3\Pi_g(v'')$ states, $N_{v'}$ is the population density of the vibrational energy level $E_{v'}$, $A_{v'v''}$ is the Frank Condon factor associated with the $v'-v''$ transition and $\nu_{v'v''}$ is the transition frequency. The population density of the

vibrational energy level can be calculated from the measured band intensities $I_{\nu' \nu''}$ using equations 4.3 and 4.4. Both the Frank-Condon factor and the transition frequency are known values [6,8].

$$N_{\nu'} \propto \frac{I_{\nu' \nu''}}{A_{\nu' \nu''} \nu_{\nu' \nu''}^4} \quad (4.3)$$

In equation 4.4 [7], N_{π} is the total population of $C^3\Pi_u$ state, Q is the vibrational partition function, K is Boltzmann's constant and T_{ν} is the vibrational temperature.

$$N_{\nu'} = \frac{N_{\pi}}{Q} \exp\left(-\frac{E_{\nu'}}{kT_{\nu'}}\right) \quad (4.4)$$

The relative population density $N_{\nu'}$ can be determined experimentally by plotting the population density versus the vibrational quantum number ν' on a semi-logarithmic plot and measuring the slope. Ideally, the points should all lie on a straight line meaning the population density distribution follows a Maxwellian distribution.

4.1.4 Optical emission spectrum from discharge

In order to better understand the nature of the discharge used in the poling process the optical emission spectrum was measured for determination of the vibrational temperature and the species of excited nitrogen molecules present in the plasma. Figure 4.8 shows a typical optical emission spectrum of the corona torch. The spectrometer used was a USB4000 Miniature Fiber Optic Spectrometer by Ocean Optics. The spectral range is 200-850 nm with a resolution of 0.3 nm.

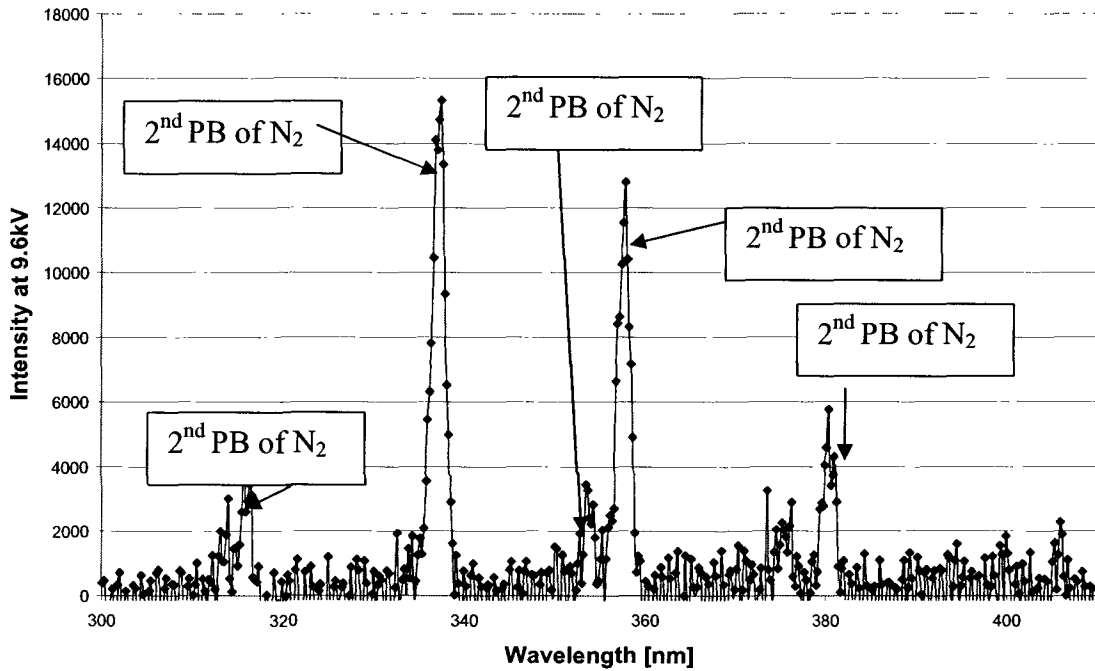


Figure 4.9: Typical optical emission spectrum of the corona torch, at $V_{\text{applied}} = 10 \text{ kV}$, $I_{\text{corona}} = 150 \text{ } \mu\text{A}$, separation distance was 13 mm and 5% MgO LN crystal present.

From Figure 4.9 it can be seen that the observed spectrum consists mainly of the second positive band (PB) of nitrogen. Other emission spectra are sometimes ambiguous due to the overlap between bands. Some other potential emission bands are summarized in Appendix B. Table 4.1 shows the quantitative data used to determine the vibrational temperature.

Table 4.1: Identified 2nd positive band emissions used and values used in calculations[6,8]

| Wavelength (nm) | Bands | Intensity (arb) | V-trans | $A_{v'v''}$ | $V_{v'v''}$ | $N_{v'}(\text{arb})$ | Normalized |
|--------------------|---------|--------------------|---------|-------------|-------------|----------------------|------------|
| 337.4 | 10(0,0) | 15331 | 0 | 4.527E-01 | 29670.6 | 4.37E-14 | 0.86 |
| 357.8 | 10(0,1) | 12816 | 1 | 3.291E-01 | 29670.6 | 5.02E-14 | 0.99 |
| 380.4 | 10(0,2) | 5777 | 2 | 1.462E-01 | 29670.6 | 5.10E-14 | 1.00 |

The population density versus the vibrational quantum number v' was plotted on a semi logarithmic plot shown in Figure 4.10. The linearity shown in Figure 4.10

suggests that the population density nearly follows the Maxwell distribution because the data points almost lie on a straight line.

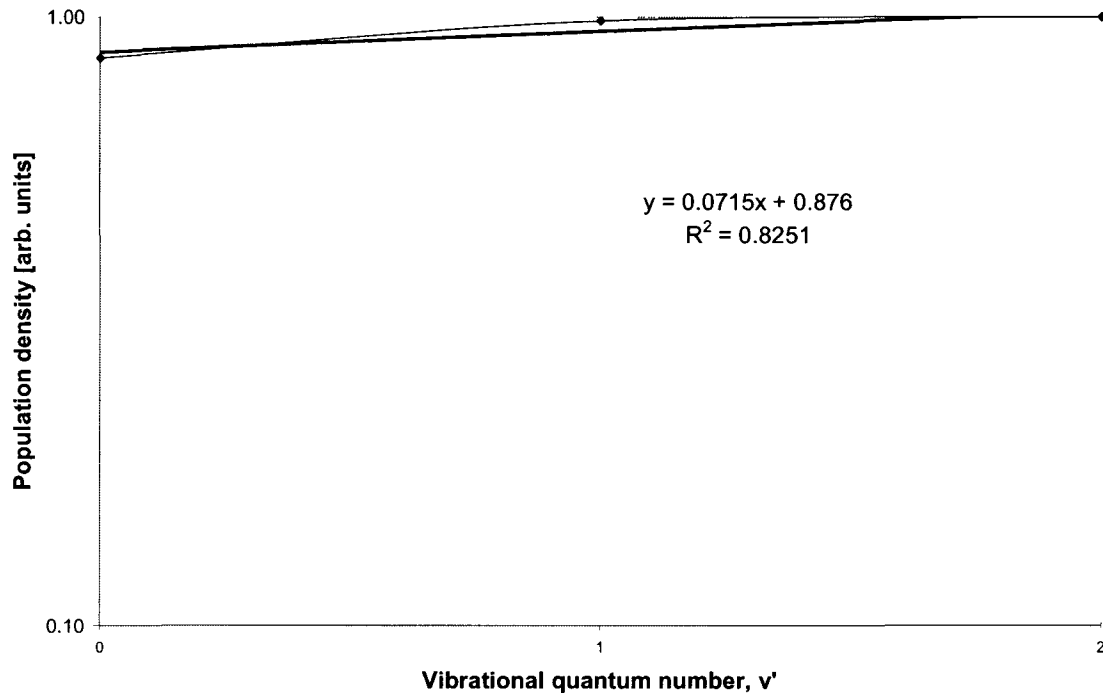


Figure 4.10: Population density versus the vibrational quantum number v' .

Using the slope obtained in Figure 4.10 and taking the natural logarithm of both sides of equation 4.3 we are able to solve for the vibrational temperature. The vibrational temperature calculated for the N_2 spectrum in Figure 4.9 was 3953 K.

References for Chapter 4

- [1] A. Harada and Y. Nihei, “Bulk periodically poled MgO-LiNbO₃ by corona discharge method,” *Applied Physics Letters*, Vol. **69** (18), 2629-31 (1996).
- [2] J. S. Chang and I. Maezono, “The effects of electrohydrodynamic flow on a corona torch,” *J. Electrostatics*, Vol. **23**, pp. 323-330, 1989.
- [3] J.S. Chang and J.G. Laframboise, “Double-probe theory for continuum low-density plasma,” *J. Phys. D: Appl. Phys.*, Vol. **9**, pp. 1699-1703 (1976).
- [4] E. O. Johnson and L. Malter, “A Floating Double Probe Method for Measurements in Gas Discharges,” *Phys. Rev.* Vol. **80**, pp. 58-65 (1950).
- [5] R. Huddlestone and S. Leonard, “Plasma diagnostic techniques,” Academic press; New York, (1965).
- [6] W. Benesch, J. Vanderslice, S. G. Tilford and P. G. Wilkinson, “Franck-Condon Factors for Permitted Transitions in N⁺”, *Astrophys. J.*, Vol. **144**, pp. 408-418, 1966.
- [7] Y. Uchida, K. Takaki, K. Urashima and J.S. Chang, “Atmospheric Pressure of Nitrogen Plasmas in a Ferro-electric Packed-bed Barrier Discharge Reactor Part II: Spectroscopic Measurements of Excited Nitrogen Molecule Density and its Vibrational Temperature,” *IEEE Transactions on Dielectrics and Electrical Insulation*, Vol. **11**, pp. 491-497, (2004).
- [8] G. Herzberg, “Molecular Spectra and Molecular Structure 1: Structure of Diatomic Molecules,” D. Van Nostrand Company, Inc., New York, (1950).

CHAPTER 5: PERIODIC DOMAIN INVERSION BY CORONA TORCH METHOD

One of the difficulties in the present parametric study is that almost all variables are interdependent and in many cases a particular variable cannot be studied simply by keeping all other variables constant. This stems from the primary feedback mechanism being the evaluation of the poled crystal post processing via chemical etching. No periodic poling or significant over poling, yields very little information. For this reason, the effect of a particular variable often requires another variable to be altered to bring the process into the functional range for evaluation.

5.1 Corona torch characteristics

Optimization efforts required an understanding of what the corona torch characteristics for the poling process are. For the poling process to be commercially viable, it must be reproducible with a high process yield. This is especially important because the current (2006) cost of a doped 76.2 mm wafer is roughly \$500 US dollars each.

Another corona torch parameter is uniformity. An even charge distribution is required so that the poling process is uniform across the entire crystal area. The surface charging must also be controllable and repeatable. How the specific process parameters influence the charging characteristics and the poling will be presented in this chapter.

5.2 Corona torch operating parameters

The corona torch performance is dependent on the various parameters. Some of the critical variables are: applied voltage, position relative to crystal, grounding electrode scheme, gas used, flow rate, etc. The ideal discharge yields a uniform glow on the surface in the desired poling region. The corona current waveform of such a discharge is roughly stable and diminishes as poling progresses. The corona current is the current involved in the plasma discharge and is measured by the high voltage amplifier. The amplifier outputs an analog voltage that represents 2 mA/V. This representative voltage is sampled 20 times per second and recorded using a data acquisition system. Figure 5.1 shows an example of a typical ideal discharge waveform.

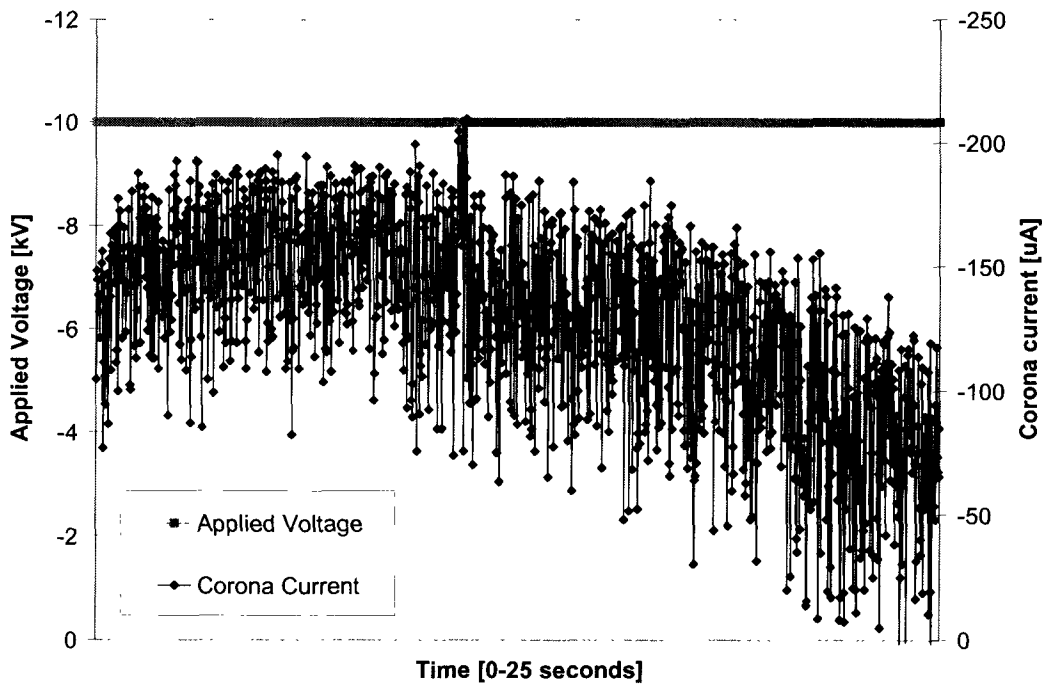


Figure 5.1: Typical corona torch current waveform yielding high quality crystal poling.

From Figure 5.1 it can be seen that the corona current diminishes as the crystal becomes progressively more poled. If the process were to continue the corona current would eventually approach 0 A. This waveform can also be used to determine the ideal poling time.

5.2.1 Effect of applied voltage

The applied voltage must be operated between the corona onset voltage and the spark initiation threshold for a corona discharge to occur. The negative corona used in poling is made up of many tiny electron avalanches that trigger successive avalanches [1]. The time average corona current for a point-to-plane geometry is usually stable even though it is composed of tiny pulses. As the voltage is increased the number of pulses increases and the time between them decreases. This is called a Trichel corona. Increasing the voltage will yield what appears to be a pulseless constant corona. As the voltage is further increased additional current carrying species will be produced and sparking will initiate. It is important to note that the transitions for a Trichel pulse to pulseless and from pulseless to sparking are not sharply defined and random [1].

The presence of the ferroelectric barrier contributes time dependence to the process. The discharge is not constant over time because the surface potential and crystal conductivity change during processing. This factor further reduces the operational voltage range. The applied voltage controls the charging rate of the crystal surface. There are two separate discharge issues that contribute to a poor poling result: an inadequate applied voltage or an excessive one.

1. Inadequate applied voltage

If the charging rate is too slow, an adequate poling potential is not reached across the entire desired poling area. Also, if the applied voltage is too low the discharge can be intermittent and the process will not take full advantage of uniformity driven by charge repulsion and surface mobility. The typical poling result under this type of discharge is high domain quality with regions left un-poled.

2. Excessive applied voltage

If the charging rate is too fast, the surface potential will get high enough to terminate the discharge. Poling done under this condition is often over-poled and the domains are poor quality because the uniformity of surface potential is not adequate for the growth of uniform domains. Figure 5.2 shows the domain structures associated with non-ideal applied voltages.

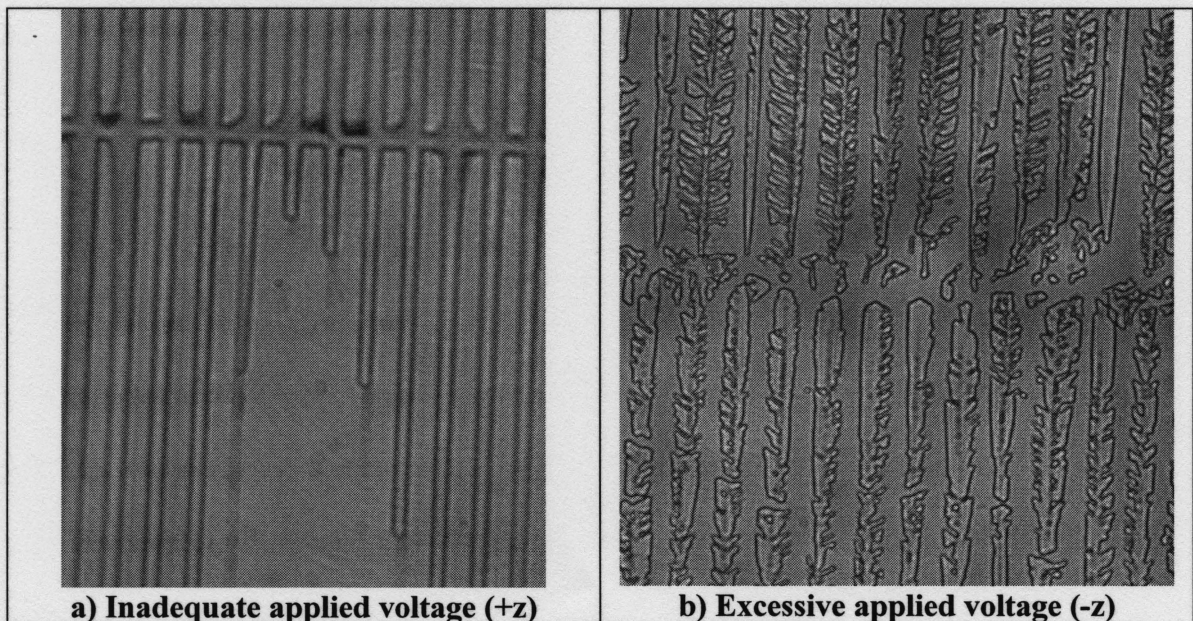


Figure 5.2: Typical domain structures for incorrect applied voltage.

From Figure 5.2 the result of both inadequate and excessive applied voltage is shown. Image a) shows how under the case of inadequate applied voltage domains will not nucleate in all areas on the (+z) surface of the crystal. Image b) shows the branching structure of the domains due to the improper growth characteristics of poling at excessive applied voltage. The domain structures were obtained by viewing the surfaces of the crystal under the microscope after etching by HF. Viewing the (-z) surface is beneficial because the domains propagate from the (+z) surface through the 0.4 mm crystal. The domain exposed at the (-z) surface represents the results of domain growth through the entire thickness of the crystal and gives excellent insight into the characteristics of domain growth.

The applied voltage not only controls the uniformity of surface charge but also its magnitude. Increasing the applied voltage, and thus the surface potential, significantly reduces the domain switching time and thus the time required to pole the crystal. This increases the required resolution of the termination control to maintain process repeatability.

Increased surface potential, as a result of increased applied voltage, may also alter the ratio of horizontal domain spreading to domain propagation in the (z) direction. The problem with using this alone to control domain profile is that there is only a small applied voltage range where domain growth is optimum. Above this voltage range the domain spreading is not uniform due to the poor discharge characteristics and the domains branch out similar to that shown in Figure 5.2. Below this range the nucleation

site density may be too low for high quality poling to be achieved and the crystal becomes over-poled in some areas and not poled in others.

There was no noticeable relation between time average corona current and applied voltage. Without the presence of the grounded crystal substrate the time average corona current would be directly related to the applied voltage. This was observed and discussed in chapter 4. In order to show that the surface potential is related to the applied voltage the poling result must be analyzed. Table 5.1 shows the % area poled directly beneath the hollow electrode and the cross-sectional domain area for different applied voltages. The crystal electrode spacing was 13 mm, the N₂ gas flow was 4 L/min and the crystal temperature was 90 °C.

Table 5.1: Typical effect of applied voltage on poling result

| Applied Voltage | % area poled | Cross sectional domain area [μm^2] |
|------------------------|---------------------|---|
| 9 | 80 - 90% | 1960 |
| 9.5 | 90 - 95% | 2349 |
| 10 | 100% | 2961 |

Table 5.1 confirms the relationship between applied voltage and cross-sectional domain area on nucleation site density because the amount of area nucleated (% area poled) increases with increasing applied voltage. The volume of inverted domains also increases with applied voltage. Larger domains are the result of faster domain growth due to the increased surface potential in the poling process. To determine the % area poled the crystal is examined from both surfaces post etching. Regions where no poling has taken place are transparent to the naked eye and poled regions appear opaque and diffract light at certain orientations. The total area of the non-poled regions is compared

to that of the intended grating area to determine the percent of area poled. This is not a precise process because it is done by eye and without the aid of image analysis. The percentage area has been expressed as a range in Table 5.1 due to the difficulty in accurately assessing the true value and the inconsistency of the nucleation phenomena. The cross-sectional domain area was determined by measuring the domain width at both (+z and (-z) surfaces. The domain cross-section is assumed to be a symmetric trapezoid which allows for the calculation of the domain area. The validity of this assumption has been verified by using image analysis on high quality cross-sectional images shown in Figure 5.9. Domain widths plotted against crystal depth yields a linear result.

5.2.2 Effect of electrode position

The position of the hollow electrode shifts the poling voltage range. The onset voltage and sparking threshold are directly related to the spacing between the crystal and the hollow torch electrode. The voltage range is also functionally larger for greater torch electrode separation.

The position of the corona torch electrode also influences the process uniformity. Separation distances from $h=5$ mm to $h=13$ mm were studied. Poling attempts below 12 mm showed some amount of over poling directly beneath the hollow electrode. Poling tests made at 5 mm showed significant over poling directly beneath the hollow electrode. Figure 5.3 compares the poling uniformity for different torch electrode positions. Uniformity is determined by comparing the measured domain duty cycles over 3 common positions across the grating. The three positions were chosen to show the

greatest contrast in domain duty cycle. The top and bottom edges of the grating and directly beneath the hollow electrode were used to determine the uniformity of processing. Both the (-z) and (+z) surfaces were analyzed. The data points for both top and bottom edges were adjusted to represent a percentage of the duty cycle in the center of the crystal. The center is always more poled than the outer edges. This allows for a more clear comparison between different electrode heights because the same center conditions could not be replicated for different electrode heights. The poling parameters used in this study were different for all 3 separation distances because no set of parameters functions for all 3 separation distances.

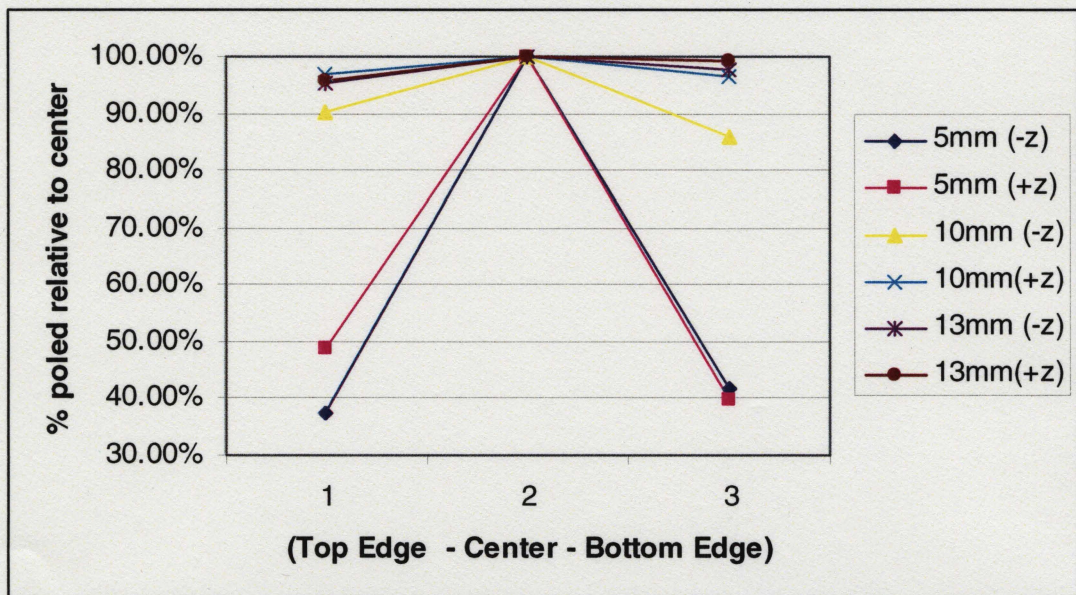


Figure 5.3: Horizontal processing uniformity for different corona torch electrode heights.

Figure 5.3 shows that for the 5 mm separation distance the domains at the edges of the grating are less than half the width of those in the center of the grating. In contrast, if we look at the 13 mm separation distance the domains at the edges of the grating are

less than 5% smaller than those directly beneath the hollow electrode. This shows that by increasing the height greater horizontal process uniformity can be achieved.

The ability to pole larger areas is desirable because it allows the creation of longer periodic gratings. Figure 5.4 shows the result of poling a full 76 mm wafer using the current corona torch. The applied voltage was 10 kV and the electrode separation was 13 mm. From Figure 5.4, the functional processing area was only achieved in an 18 mm diameter circle directly beneath the hollow electrode. The diameter of the anode pattern was 52 mm. The poling time was 20 seconds.

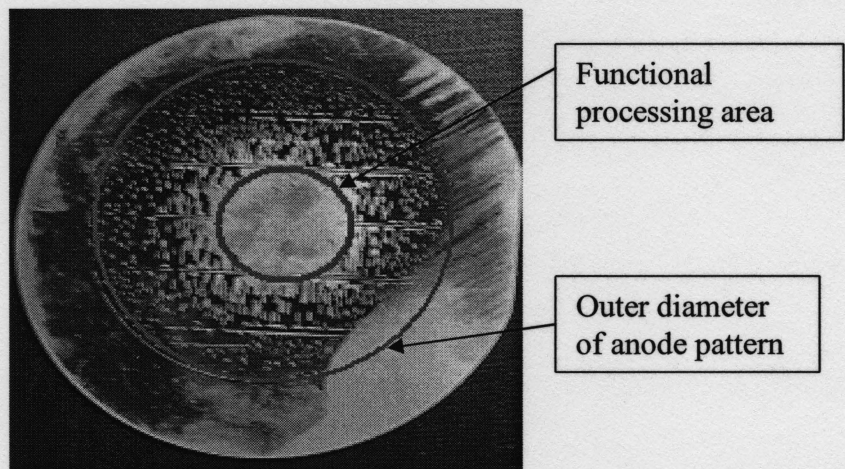


Figure 5.4: Poling of a 76 mm substrate with single corona torch in center position.

After poling, the crystal was removed and the extent of poling was observed using non etching techniques. The process was then repeated. There was no observable change in the area poled. This suggests that the poled area cannot be increased by simply increasing poling time and that other techniques are required to pole the full 76 mm wafer. The quality of the poling was then analyzed by etching in HF. As expected the poling in the center region was significantly over poled. This was due to the extensive poling time.

Due to the inability to evaluate the poling inside the 18 mm diameter center region we can only state that the functional area of the corona torch is less than the 18 mm diameter and greater than the 12 mm diameter of the quarter wafer patterns.

In order to pole the 76 mm wafers by corona torch method it will be necessary to employ multiple corona torch electrodes in order to achieve the horizontal charge distribution required to uniformly pole the large area crystal. Figure 5.5 shows a 76 mm substrate, after etching in HF that has been poled with a single corona torch from multiple torch positions at different times.

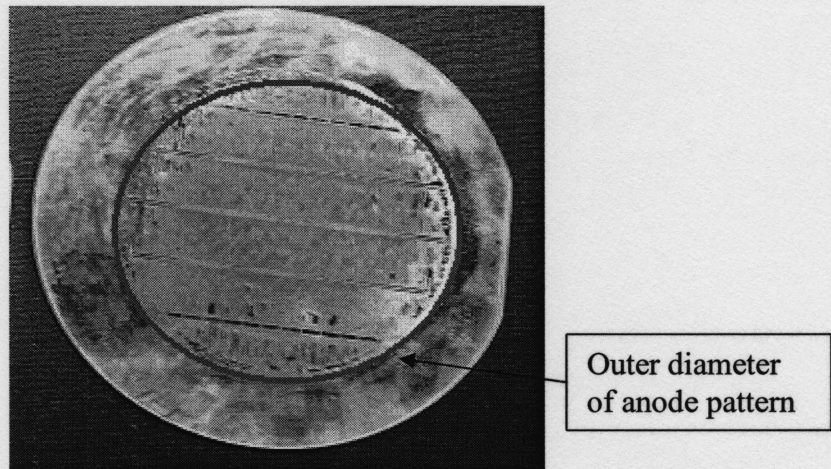


Figure 5.5: Poling of a 76 mm substrate with multiple corona torch positions.

By poling the large area crystal from many positions at different times shows that the required surface potential can be reached in all areas of the large crystal by using the current device. The poling duration was 10 seconds in each region and the poling process was repeated in 12 different positions. The quality of the poling result was very poor, as many regions were significantly over poled. In order to pole this size wafer successfully a 2D array of corona torch electrodes will be required so that the entire area is poled

simultaneously. The complication with employing more corona torch electrodes will be how they affect each other with regards to space charge and the resulting electric field.

5.2.3 Effect of gas and flow rate

Before significant poling could be achieved both UHP nitrogen and UHP argon were used in efforts to achieve domain inversion of the doped crystal. Argon had a lower onset voltage and a lower arcing threshold than nitrogen. The majority of the poling study was performed in nitrogen because it was the first gas to demonstrate domain inversion.

The nitrogen flow through the corona torch stabilized the discharge as well as contributed to ion transport in the direction of flow. Current waveforms over 25 seconds at 10 kV were compared for differing flow rates from 0 – 8 L/min. It was observed that the corona torch current was most consistent between 1-5 L/min. No real performance difference could be seen across this range so 4 L/min was chosen for the poling process as it contributes to ion transport [2]. This variable has been held constant for most of the poling study. This variable should be further studied in order to determine its effect on the poling result through contribution of ion transport.

5.3 Crystal Variables

The properties of the crystal are also very important in the poling process. As mentioned previously, the introduction of the ferroelectric barrier greatly increases the complexity of this system. The crystal is functionally conductive during the poling.

There are 3 likely reasons for the crystal conductivity. First, the ions migrate along the surface of the crystal via surface diffusion. Second, the doped crystal has some conductivity. Lastly, the domain inversion process inherently displaces charge which acts like a current. If the crystal and its support structure are removed it drastically alters the discharge characteristics. Without the crystal, the onset voltage is much higher and the achievable torch corona current is much lower. Not only is the crystal a dominant parameter in the process but its properties change over time during the poling process. Figure 5.6 shows the typical time dependence of the poling process that is a result of the varying crystal parameters.

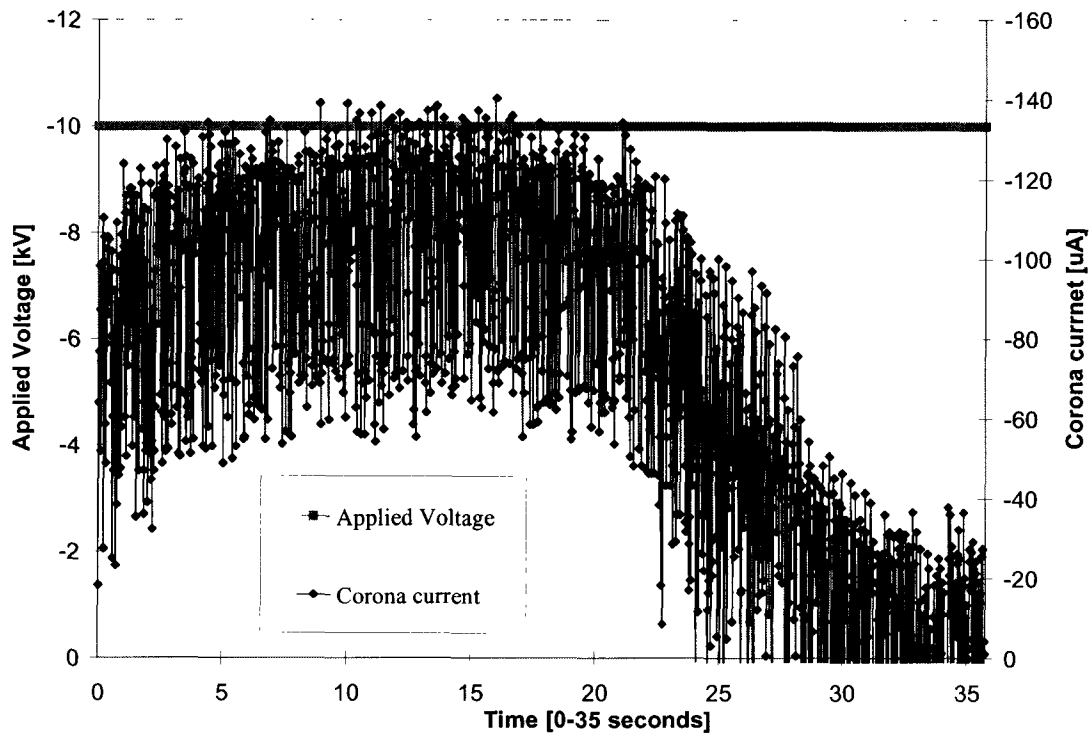


Figure 5.6: Typical corona current vs. time.

Figure 5.6 shows how the current drops to zero over the course of the poling process. This also shows how the crystal and its time dependent properties have a very

significant effect on the discharge characteristics. This is a typical waveform of an overpoled substrate.

5.3.1 Effect of crystal temperature

Increasing the crystal temperature alters many of its properties. Most importantly, by increasing the crystal temperature the required coercive field for domain inversion is reduced [3]. This shifts the required poling voltage down and also reduces the required poling time by increasing the domain switching rate [3]. Experimental observation has observed that increasing temperature has a similar effect to increasing the applied voltage.

The main motivation behind studying the crystal temperature effect was to determine if temperature could alter the range of achievable domain profiles. Ideally the domain width should be the same on the (-z) surface as it is on the (+z) surface. This has presented itself as a major challenge in corona discharge poling. By increasing temperature and thus the domain switching rate, it was believed that profiles closer to the ideal profile could be achieved. Only poling results with high quality domains could be analyzed. Crystal temperatures of 50 °C and 90 °C and voltages of 9 kV and 10 kV were used. Applied voltages above 10kV were not used in this study because they often yielded intermittent current waveforms and/or resulted in poor domain quality. Table 5.2 shows typical data from optimization efforts from these four parameters. The data presented in this table is the best result taken from each of the four different poling parameters.

Table 5.2: Typical data from temperature study of corona torch at applied voltage V_c

| Crystal Temperature | $V_c = 9$ kV | $V_c = 10$ kV |
|---------------------|---|---|
| 50 °C | Time: 20 seconds Domain quality: not perfect -z duty cycle: 26% +z duty cycle: 51% Δ domain width: 4.5 μm | Time: 15 seconds Domain quality: Excellent -z duty cycle: 14% +z duty cycle: 51% Δ domain width: 7.1 μm |
| 90 °C | Time: 30 seconds Domain quality: Excellent -z duty cycle: 27% +z duty cycle: 69% Δ domain width: 8.1 μm | Time: 20 seconds Domain quality: Excellent -z duty cycle: 24% +z duty cycle: 50% Δ domain width: 4.9 μm |

From this temperature study no conclusion regarding the temperature dependence on achievable domain profile can be drawn. Further work is required in order to better understand the effect this parameter has on the poling process.

5.3.2 Effect of anode properties

The anode properties are important for two reasons. First, the anode pattern provides the nucleation condition. Domain nucleation occurs at the edge of the grounded anode bars [4]. The dimensions, metal used, and insulation scheme all affect the nucleation condition [5]. Second, the anode dimensions determine the starting point for domain growth. Domain propagation is dependent on the position of neighboring domains during their growth. The ranges of achievable domain profiles are dependent on the initial dimensions of the anode bars. Both the anode period and duty cycle are important factors in achieving good domain profiles.

In order to determine the effect of the insulation schemes employed, the optimized condition was applied to 3 samples with different anode insulation schemes, high vacuum, photoresist, and no insulation scheme. The high vacuum scheme involved submitting the metal anode grid to a region of low pressure 10^{-4} Torr. The photoresist method involved using a spin coated polymer layer to insulate between the electrode bars. The other case “no insulation” involved anode bars in a regular air environment. The anode patterns that employed some method to increase electrical insulation yielded typical optimized poling quality with near 100% uniformity. Any difference between these samples cannot be seen as it could easily be attributed to lithography errors. In the sample where no insulation scheme was used, the domain quality was noticeably reduced. This is likely due to a reduced nucleation site density and thus different domain growth dynamics. The growth dynamics associated with this reduced nucleation site density are not favorable for achieving high levels of uniformity.

5.3.3 Effect of proton exchange pretreatment

Proton exchange has been demonstrated to control domain spreading for the purpose of periodic poling of MgO-doped lithium niobate [6]. Not only can it be used to inhibit horizontal domain spreading, but it has also been used as the only method of creating the periodicity required for QPM gratings. This means that proton exchange is capable of not only inhibiting spreading but also inhibiting the nucleation of domains.

Proton exchange was performed for 2 different durations in order to determine if the depth of proton exchange had any effect on the domain spreading. The crystal was

heated in benzoic acid at 200 °C for for 30 minutes and also for 2 hours. Both proton exchange samples were similar. Under both conditions the reduction of domain spreading could be seen. Figure 5.7 shows the effect of proton exchange treatment on domain profile. The dark regions represent poled domains.

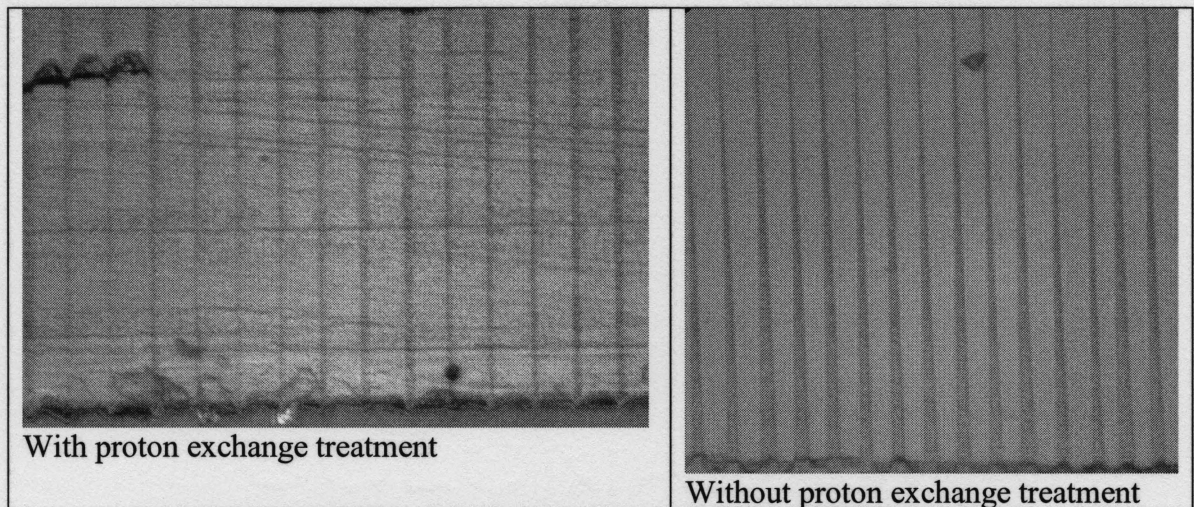


Figure 5.7: Effect of proton exchange treatment on domain profile.

In all trials yielding measurable domain structures, the domain profiles of the inverted domains are wider at the anode side of the crystal. This is because spreading occurs for a longer duration near the anode where the domain first nucleates. By periodic proton exchange treatment the domain width near the anode can be controlled by inhibiting domain spreading. Figure 5.7 shows how the opposite domain profile can be achieved under proton exchange pretreatment.

A major drawback of the proton exchange pretreatment was the destruction of process uniformity. During the corona poling process it was clear that the plasma distribution was not uniform across the crystal surface. Many small spots would glow as opposed to the entire intended region. These glowing spots were stable throughout the

process and corresponded to the regions where poling had taken place when evaluated afterwards. Initially it was not understood why the process uniformity had been lost. In order to determine which crystal surface was reducing the process uniformity the top (-z) surface was protected with deposited aluminum during the proton exchange process. Even with the top surface protected from proton exchange the uniformity issue still remained. This strongly suggests that the issue is with the proton exchanged regions between the anode bars. It is likely that the proton exchange is not perfectly step like and it that it is inhibiting the nucleation that occurs at the edges of the anode bars. When the proton exchange time was reduced and the top surface was protected this issue still remained.

In order to take advantage of proton exchange as an inhibitor to domain spreading a new proton exchange scheme is required. One option to reduce the nucleation uniformity issue would be to expose a narrower region to the proton exchange treatment. This ensures that the edges of the anode bars do not extend into the proton exchange treated region. This would involve another mask and lithography step and may be tried in the future. Another option is to use the anode bars as a window for proton exchange and then deposit additional chrome afterwards to make a solid anode. The periodic proton exchange treatment should uniformly nucleate periodic domains.

5.3.4 Batch dependent properties

It is very clear that there are differences between crystal batches. At this point the exact differences are not understood. The poling parameters used for the optimal poling differ from batch to batch and from supplier to supplier. For example, the optimized poling conditions for the first crystal batch were applied to the second batch. The result was drastically different.

This batch to batch variance is not seen in non-doped crystal wafers to the same extent. For this reason it is likely that the doping is related to the inconsistency between batches. It is possible that the MgO doping concentration or distribution uniformity may be slightly different between batches. There are many other factors not related to doping that could be the cause of the differing properties between wafer batches. Variance in crystal growth conditions and the presence of impurities could also explain the difference in crystal properties, however this should also be seen in non-doped crystals.

5.4 Characterization of MgO-PPLN

Through the optimization of the corona torch for the purpose of poling MgO-doped lithium niobate, many domain-inverted gratings, of various qualities, have been fabricated. In this section, the optical performance of these gratings will be discussed and linked to particular domain characteristics.

5.4.1 Quality of optimized periodic domain inversion

The corona discharge poling has been optimized to achieve excellent processing uniformity over a 12 mm grating length. With the incorporation of multiple corona torches larger gratings are likely possible. The flow stabilized corona torch method has demonstrated excellent poling results in comparison to other processing methods. Figure 5.8 shows a typical domain profile under optimized conditions.

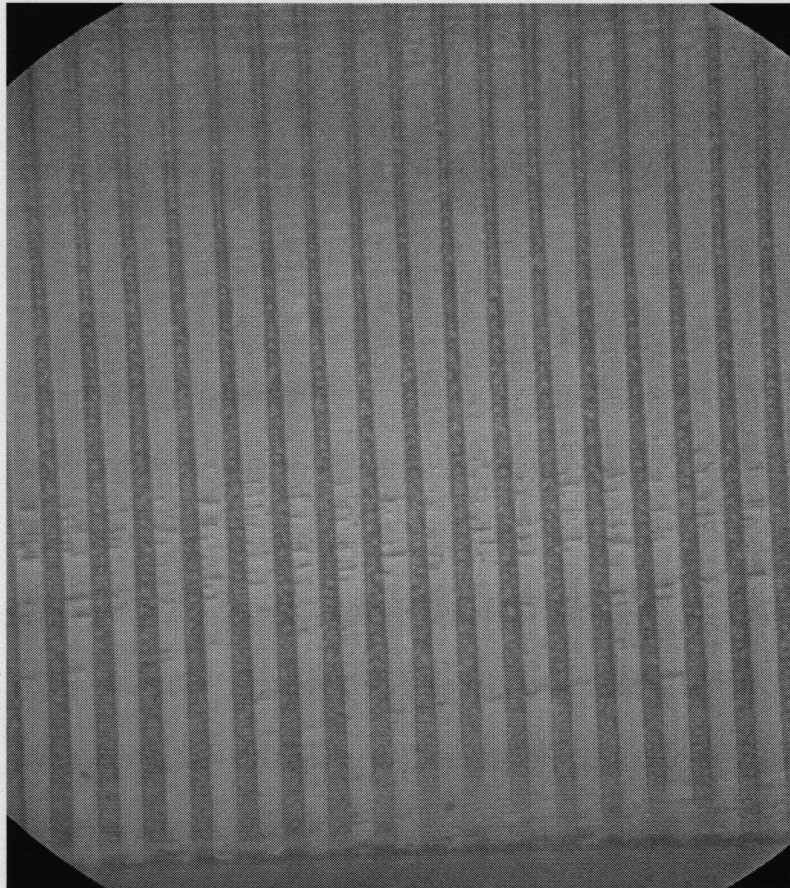


Figure 5.8: Typical domain profile under optimized poling conditions

Figure 5.8 shows almost the entire cross-section of a 0.4 mm thick crystal after polishing and etching in HF. From Figure 5.8 it can be seen that the dark (domain inverted) regions have a different duty cycle throughout the thickness of the crystal. This

means that the SHG efficiency will also vary in different regions of the poled crystal. In order to achieve the highest possible device efficiency the domain duty cycle must be 50%.

Using the image shown in Figure 5.8 the straightness of the domain boundaries can be analyzed. Figure 5.9 shows the measured domain width and grating period for different vertical positions in the crystal.

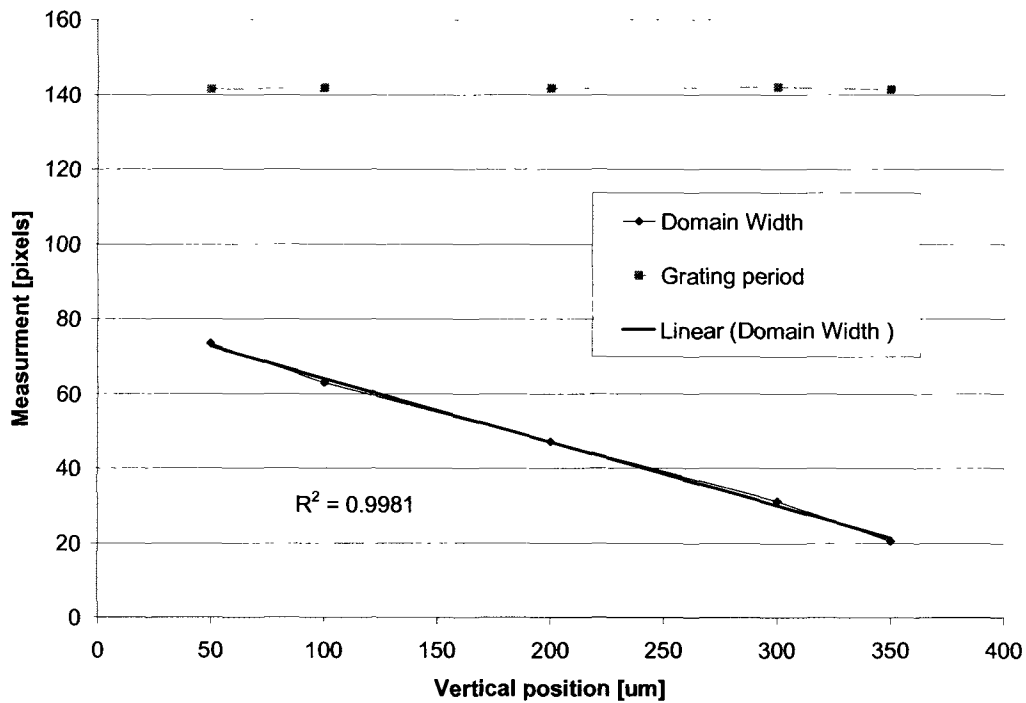


Figure 5.9: Measured domain width and grating period at different vertical positions in the crystal.

From Figure 5.9 it can be observed that the domain width is linearly related to the vertical position inside the crystal. It can be concluded that the domain boundaries are straight inside the crystal. This further verifies that domain measurements taken from the (+z) and (-z) surfaces of the crystal are adequate to accurately determine domain profile throughout the material.

5.4.2 SHG performance of MgO-PPLN

One way to evaluate the quality of a grating and its uniformity is to analyze the SHG tuning curve. The method of analysis allows for non-invasive analysis of domain quality. If the periodic grating is highly uniform, the SHG tuning curve will look like a SINC function. The SHG tuning curve is established by measuring the maximum SHG power using an optical spectrometer for various pump wavelengths. A tunable laser was used to pump the device at different wavelengths at 0.2 nm intervals. Figure 5.10 shows a schematic of the experimental setup used to analyze SHG performance.

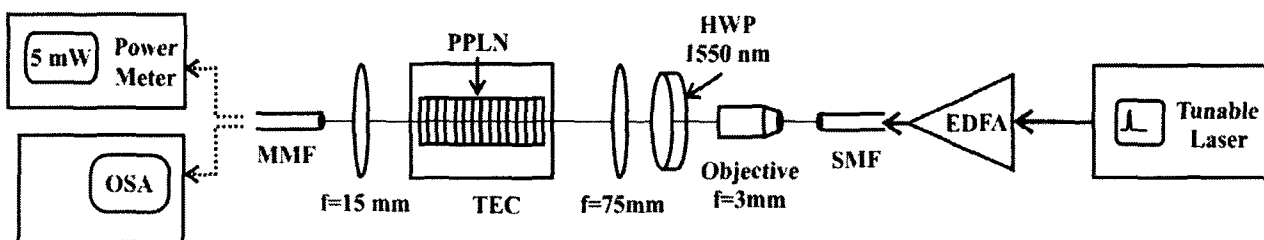


Figure 5.10: Schematic of experimental setup used to analyze SHG performance.

Figure 5.11 shows the resulting SHG tuning curve of a grating poled by corona discharge compared to the theoretical tuning curve for a device of that length. From the symmetry and agreement with the theoretical tuning curve shown in Figure 5.11 it is clear that the domain period is uniform across the sample tested. Any significant deviation in domain position would reduce the symmetry of the SGH tuning curve [7]. When using lithography defined nucleation control, this type of error can be the result of poor domain propagation in the material. The sensitivity to domain duty cycle error is less complex. In this case the average Δk through the material is 0. This duty cycle error only results in a reduction in efficiency [7].

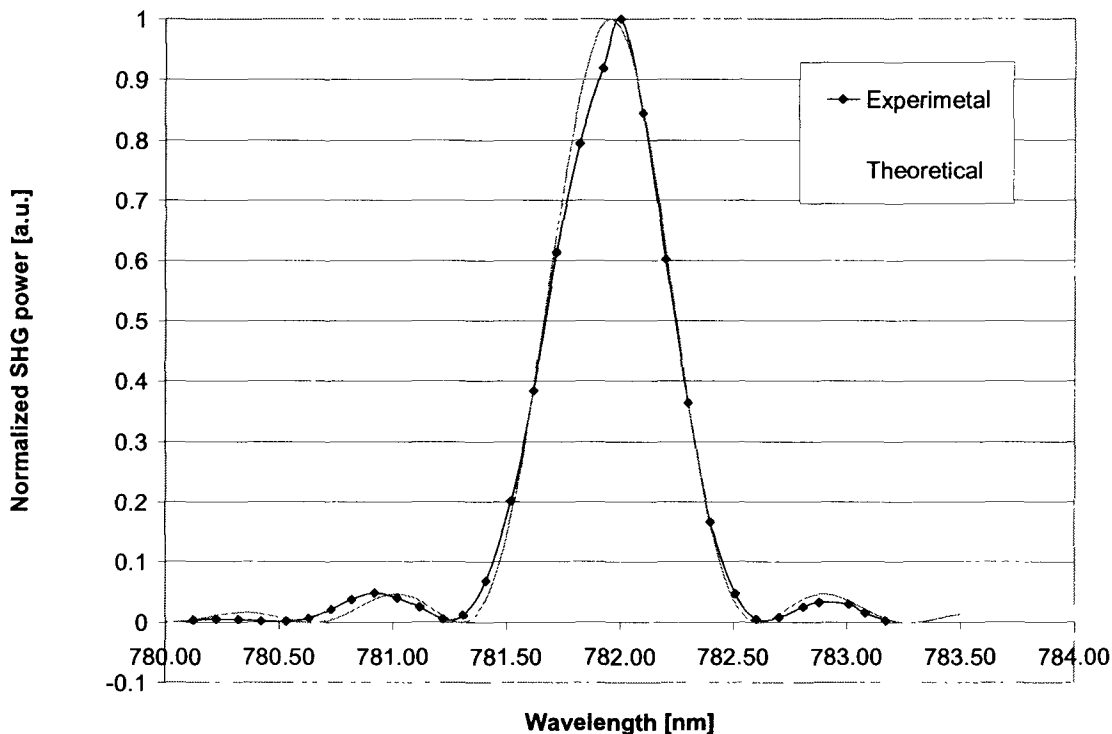


Figure 5.11: SHG power vs. wavelength.

The bandwidth of the SHG tuning curve from Figure 5.11 measured at full width half maximum is 0.6 nm. In order to better understand the merits of the corona poling method, a comparison with other works should be conducted using the same testing apparatus. It is important to mention that only the shape of the tuning curves is relevant in this comparison.

The only way to truly compare two gratings is to test them with the same apparatus. The beam confinement in the bulk, as well as the polarization of the pump could vary significantly. The device efficiency is also proportional to the length squared so it is difficult to compare devices of different lengths. This complicates device comparison because the mathematical expression for the Gaussian beam and its SHG performance cannot be perfectly described mathematically.

5.4.3 QPM temperature shift in MgO-PPLN

By altering the temperature of the periodic grating the QPM wavelength can be shifted. Increasing the temperature from 20 °C to 155 °C shifts the QPM wavelength by roughly 17 nm. Increasing temperature increases the QPM wavelength; this is called a red shift. The Sellmeier Equation shown in equation 5.1 was used to generate the theoretical plot shown in Figure 5.12. The constants A_i , B_i , C_i , and D_i in the Sellmeier equation have been well established experimentally [8] for different temperatures and both the ordinary and extraordinary refractive indices of MgO doped lithium niobate.

$$n_i^2 = A_i + \frac{B_i}{\lambda^2 - C_i} + D_i \lambda^2 \quad (5.1)$$

Figure 5.11 shows the relationship between temperature, domain period and QPM wavelength. Temperature dependence is an important factor of QPM gratings in nonlinear crystals because it allows the QPM wavelength to be tuned after periodic domain inversion has been performed. Small errors in the grating period have a significant affect on QPM wavelength. This means that coherent sources based on the technology will always require temperature control of the crystal to ensure wavelength accuracy and stability. This also means a tunable laser can be easily achieved at little added cost. Another important matter involving crystal temperature is the optical damage threshold. This threshold is increased with increased temperature as well as the recovery time post damage.

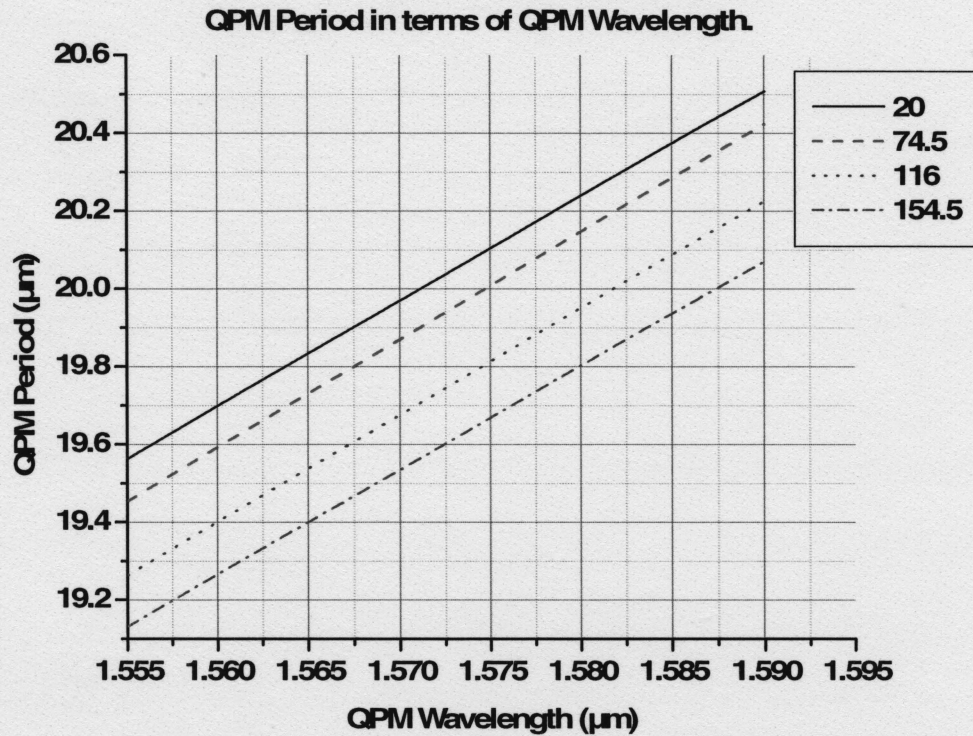


Figure 5.12: Temperature effect on QPM wavelength based on Sellmeier equation.

A similar red shift can be seen in the gratings poled via the corona discharge method. Figure 5.13 shows the QPM and SHG wavelengths for different temperatures in a typical sample poled by the corona torch. The linearity of Figure 5.13 shows that the gratings achieved by corona discharge function in the theoretical manner.

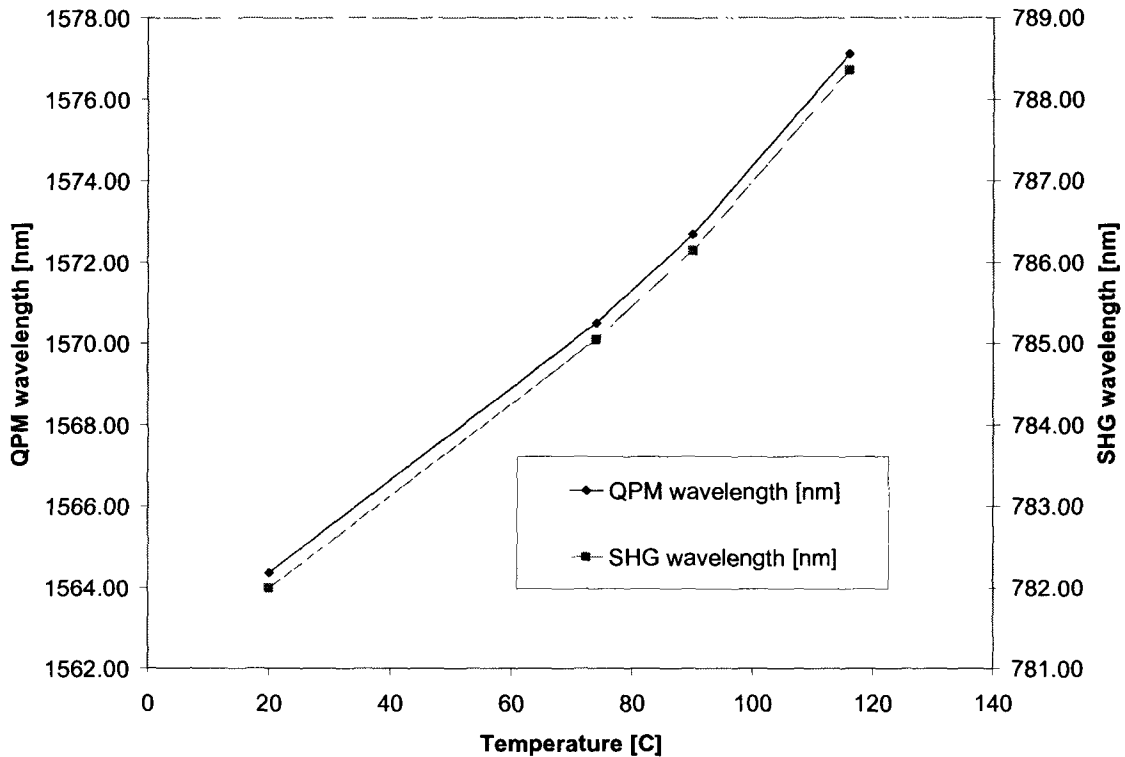


Figure 5.13: Temperature effect on QPM wavelength.

5.4.4 SHG performance related to domain characteristics in MgO-PPLN

In order to determine the effect of domain profile on SHG performance the pump beam was passed through the crystal at different vertical positions. The maximum SHG power was measured at multiple positions in the vertical dimension. Figure 5.14 shows the effect of a non-ideal domain profile on the SHG performance in different regions of the crystal. Ideally, the domain duty cycle should be 50% throughout the entire thickness of the crystal and the SHG output should be constant throughout the material tapering off at the edges the crystal due to coupling and scattering losses.

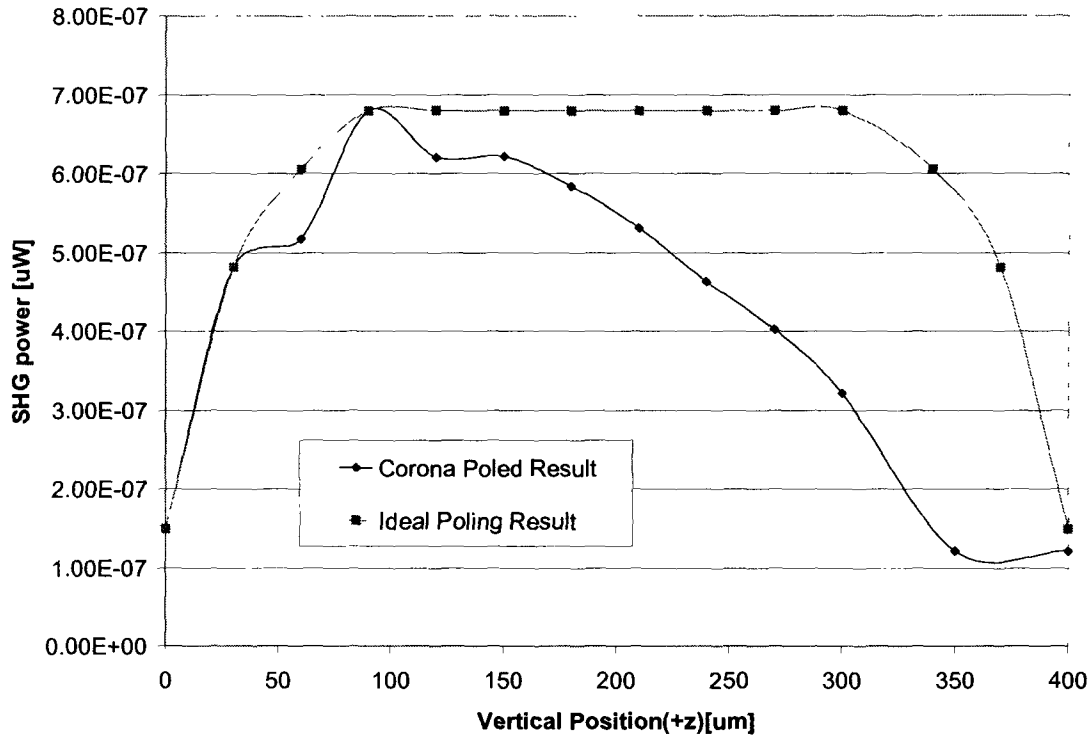


Figure 5.14: Device performance vs. Vertical position.

Figure 5.14 shows how the SHG power deviates from the ideal. The ideal curve shown in figure 5.14 is for discussion purposes only. The ideal curve was generated by mapping the coupling/scattering loss at the bottom of the crystal and assuming it would be the same at the top. Also, a constant peak performance throughout the core of the material was assumed. Although we know the beam waist to be $30\ \mu\text{m}$ at FWHM it is difficult to quantify the loss when coupling near the crystal edge due to scattering at the etched crystal surface. In order to explain the lack of symmetry in Figure 5.14 it is important to consider the domain duty cycle at different vertical positions in the poled crystal. Figure 5.15 overlays the domain duty cycle as a function of vertical position with the SHG performance.

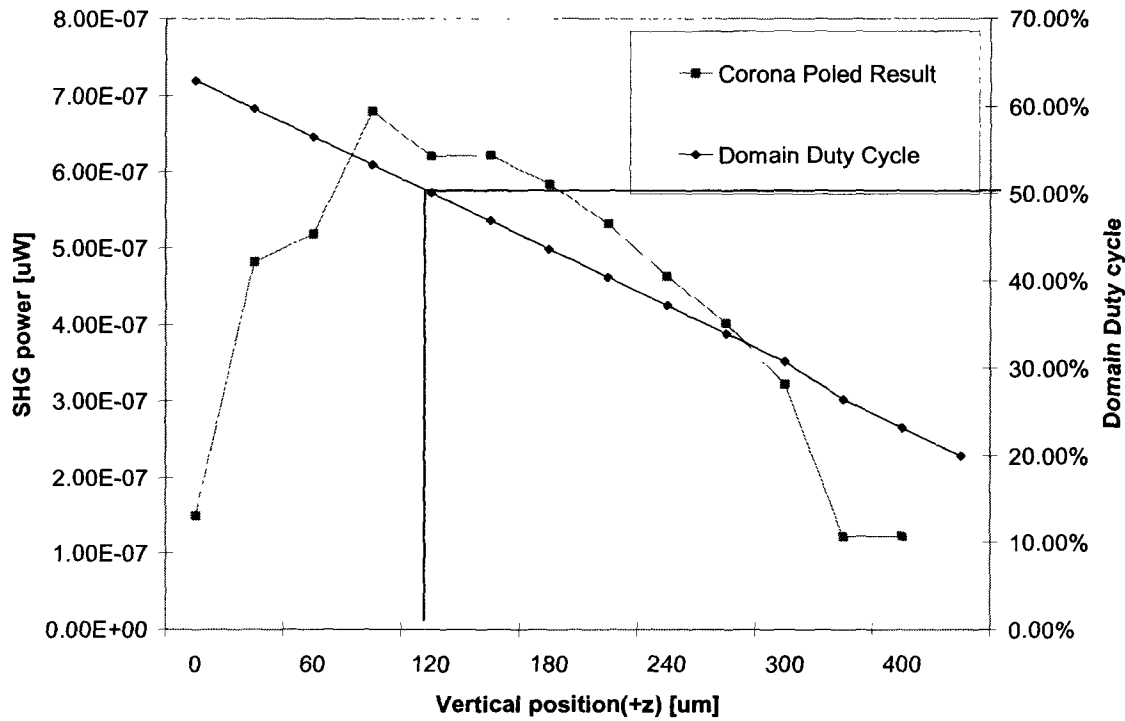


Figure 5.15: Device performance vs. domain duty cycle

Figure 5.15 shows that the peak SHG power corresponds to where the duty cycle is around 50%. The method of duty cycle measurement is described in Chapter 3.

5.4.5 SHG efficiency of MgO-PPLN

The analysis of SHG efficiency is based on the assumption that the pump beam can be accurately described by a focused Gaussian beam. Figure 5.16 shows a depiction of SHG generation with a focused Gaussian beam. The beam waist, w_1 , was measured to be 30 μm at FWHM and 33 μm at $1/e$.

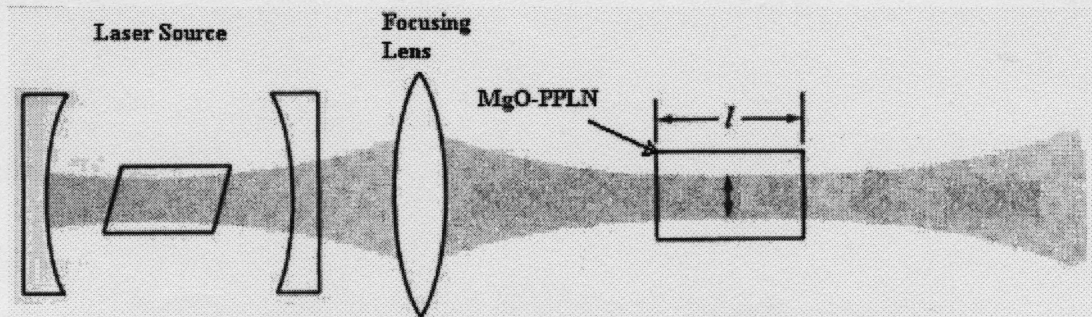


Figure 5.16: SHG generation with a focused Gaussian beam

The efficiency can be expressed as [9]

$$\eta = \frac{P_{2\omega}}{P_{\omega}^2} = \frac{2\omega^2 L^2 d_{eff}^2 \exp\{-L(\alpha_{\omega} + \frac{1}{2}\alpha_{2\omega})\}}{\pi\epsilon_0 c^3 \omega_1^2 n_{\omega}^2 n_{\omega}} \sin^2\left(\frac{\Delta\kappa L}{2}\right) \quad (5.2)$$

where ω is angular frequency of the fundamental wave, d_{eff} is the effective nonlinear coefficient under ideal QPM with $\Delta k=0$ and α is the absorption coefficient.. The calculated conversion efficiency was 1.12 %/W/cm. The calculated d_{eff} achieved by corona discharge poling was 17.5 pm/V, which agrees well with reported theoretical values of 16~19 pm/V [5, 10].

References for chapter 5

- [1] J.S. Chang, A. Kelly, J. Crowley, "Handbook of Electrostatic Processes," Marcel Dekker, Inc., New York, (1995).
- [2] J. S. Chang and I. Maezono, "The effects of electrohydrodynamic flow on a corona torch," J. Electrostatics, Vol. 23, pp. 323-330, 1989.
- [3] H. Ishizuki, I. Shoji, and T. Tiara, "Periodical poling characteristics of congruent MgO:LiNbO₃ crystals at elevated temperature" Appl. Phys. Lett. 82, 4062-4064 (2003).
- [4] L. E. Myers, R. C. Eckardt, M. M. Fejer *et al.*, "Quasi-phase-matched optical parametric oscillators in bulk periodically poled LiNbO₃," Journal of the Optical Society of America B (Optical Physics) 12 (11), 2102-16 (1995).
- [5] A. Harada and Y. Nihei, "Bulk periodically poled MgO-LiNbO₃ by corona discharge method," Applied Physics Letters 69 (18), 2629-31 (1996).
- [6] S. Grilli, C. Canalias, F. Laurell, P. Ferraro, P. De Natale, "Control of lateral domain spreading in congruent lithium niobate by selective proton exchange," accepted by Applied Physics Letters.
- [7] M. Fejer, G. Magel, "Quasi-Phase-Matched Second Harmonic Generation: Tuning and Tolerances," IEEE J. of Quantum Electronics, 28, 2633-2654, (1992).
- [8] H.Y. Shen, "Measurement of refractive indices and thermal refractive-index coefficients of LiNbO₃ crystal doped with 5 mol % MgO," Applied Optics, 31, 6695-6697, (1992).
- [9] M. Weber, "Handbook of Laser Science and Technology Vol. 3: Optical materials Part1: Nonlinear Optical properties/Radiation Damage," CRC Press, Inc., Florida (2000).
- [10] T. Suhara and M Fujimura, "Waveguide Nonlinear-optic Devices," Springer, New York, 5,10 (2003).

CHAPTER 6: CONCLUSIONS

A corona discharge method for periodic domain inversion of ferroelectric LiNbO₃ was experimentally investigated. In this work, a flow stabilized corona torch was used for periodic domain inversion of lithium niobate with a 19.1 μm periodic grating. By analysing the SHG tuning curves, the grating uniformity has been evaluated and the effective non-linear coefficient (d_{eff}) achieved through corona discharge poling was 17.5 pm/V, which agrees well with theoretical value of 16~19 pm/V. Due to horizontal domain spreading the duty cycle varies throughout the thickness of the crystal.

The objective of this work was to develop a corona discharge poling method for the purpose of domain inversion in MgO-doped LiNbO₃. The drive behind this method is that by soft charging the (-z) surface of the crystal via a negative polarity corona discharge, a more uniform process of domain inversion can be achieved. Through this soft charging method the negative effect of crystal irregularities can be minimized by limiting the mobility of charge.

In chapter 4 the corona torch characteristics were studied. It was observed that presence of the grounded crystal and crystal doping greatly affect the discharge characteristics of the corona torch. A floating potential double probe was used to measure ion density in different locations in the region downstream of the corona torch because it causes minimal disturbance to the plasma environment. The distribution of ion density was observed which suggest that greater process uniformity can be achieved by increasing the spacing between corona torch and lithium niobate crystal. Optical emission spectroscopy was used to investigate the plasma parameters such as the

identification of molecules and vibrational and rotational temperatures. The observed spectrum consisted mainly of the second positive band of nitrogen and the vibrational temperature calculated for the N₂ spectrum was 3953 K.

In chapter 5 the effects of many process parameters, such as applied voltage, gas flow, electrode to crystal separation, crystal temperature etc., on the poling result were studied. It was observed that many of these parameters are interdependent. The applied voltage range of 9 kV to 10 kV was observed to be optimum for domain growth which may be due to both the uniformity and magnitude of the surface charge. Increasing the applied voltage, and thus the surface potential, may significantly reduce the domain switching time and therefore the time required to pole the crystal.

The nitrogen gas flow functions to stabilize the corona discharge and increases ion transport in the direction of gas flow. The position of the hollow electrode changes the discharge characteristics of the corona torch. By increasing the separation distance between the hollow torch electrode and the crystal surface the horizontal process uniformity can be greatly improved.

The crystal is conductive during the poling process. The crystal contributes a time dependence to the poling process and significantly influences the discharge characteristics of the corona torch. The crystal and the discharge are linked to the extent that the corona poling is a self-terminating process. The batch-to-batch variance associated with MgO doped crystals requires optimization of each batch of wafers as they have significantly different poling conditions. By increasing the crystal temperature the required coercive field for domain inversion is reduced. This lowers the required poling

voltage and also reduces the required poling time by increasing the domain-switching rate. Experimental observation has observed that an increase in temperature has a similar effect to an increase of applied voltage.

The nucleation site density is affected by the electrical insulation scheme used to increase discrimination between the anode bars and the regions between them. Although the ideal scheme was not determined, it was observed that both high vacuum and photoresist functioned similarly and can yield a high quality poling result. Without employing either of these techniques high quality results have not been obtained.

Proton exchange has been demonstrated to control domain spreading for the purpose of periodical poling of MgO-doped lithium niobate. A major drawback of the proton exchange pretreatment was its effect on the uniformity of domain nucleation. The proton exchange process must be altered so that it doesn't hinder the domain nucleation process.

Future efforts involving a proton exchange treatment and altering anode duty cycle will very likely result in a near flawless final product. The corona discharge poling method is a valid solution for the large scale production of MgO-PPLN since the method involves less substrate preparation and is better suited to deal with crystal imperfections. It was expected that the present method, when optimised, would have higher process yields than the conventional electrostatic method.

CHAPTER 7: RECOMMENDATION FOR FUTURE WORK

There are a number of topics related to this thesis which either were not completed for various reasons, or which would be interesting to explore in the future.

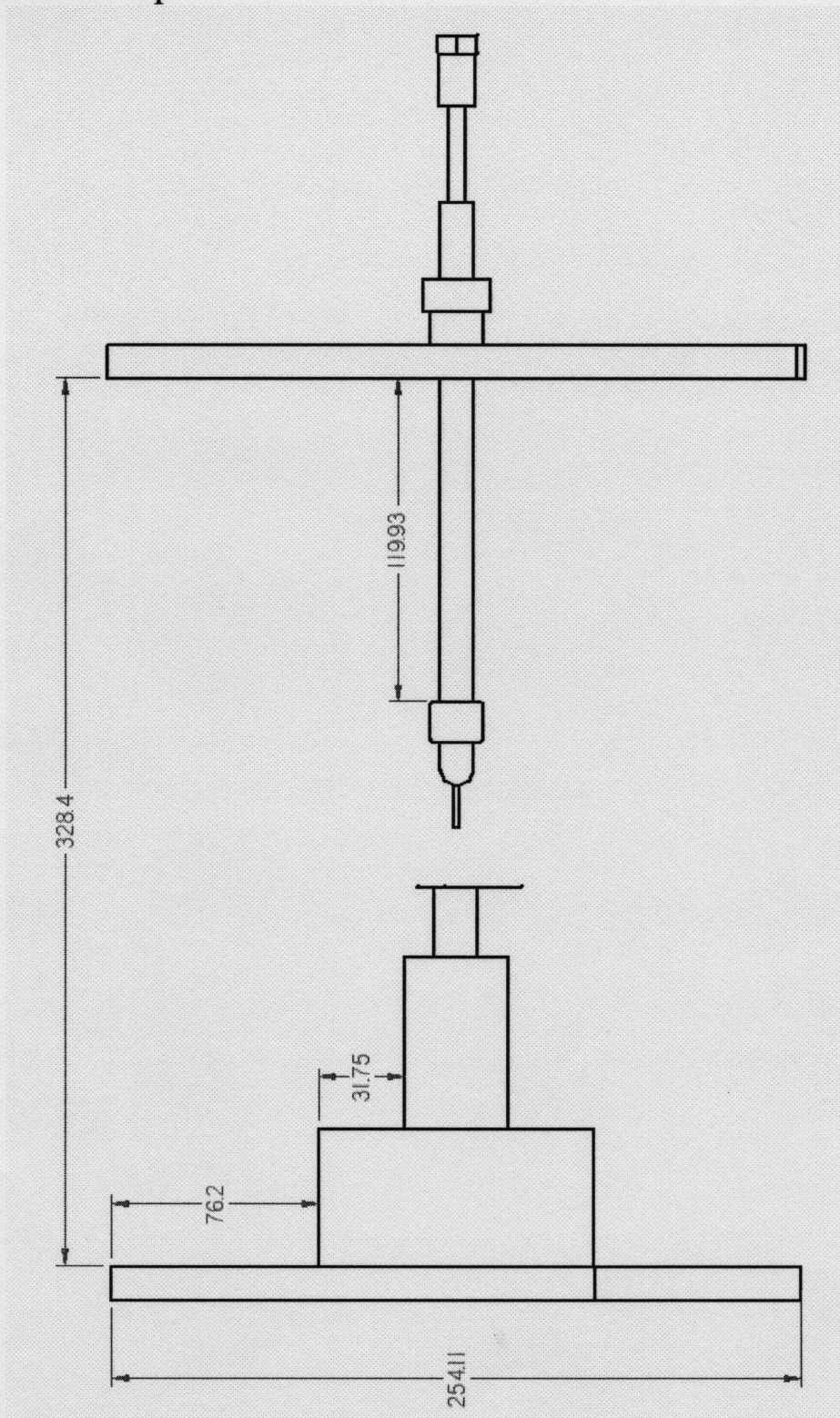
1. In order to pole larger wafers and create longer more efficient gratings the use of multiple torches employed in a 2D array should be developed.
2. In order to fully optimize domain profiles different anode duty cycles and their effect on domain growth dynamics should be explored.
3. Greater efforts should be devoted to utilizing proton exchange as an inhibitor to horizontal domain broadening. This can be achieved by simply adding another lithography step to the current process.
4. Numerical modeling could be utilized for the purpose of
 - a. Determining the optimum anode insulation scheme.
 - b. Studying domain kinetics and the effect of external parameters.
5. The effect of gas flow should be further studied in order to determine its effect on the poling result through its contribution to ion transport.

Appendix A

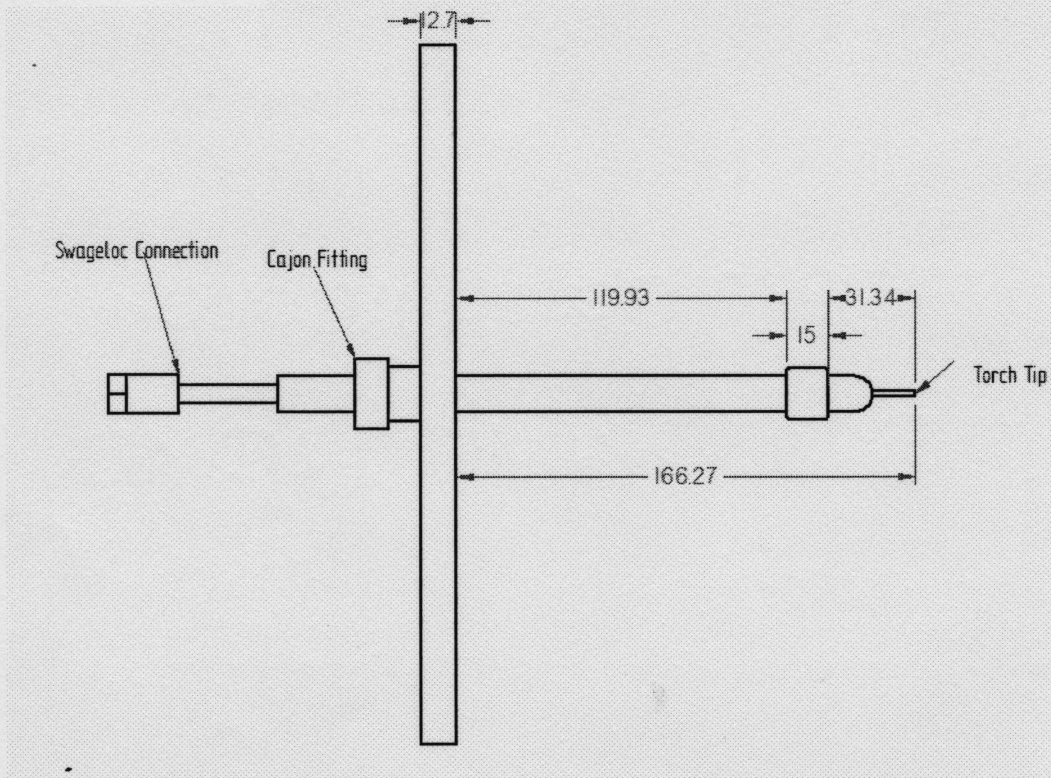
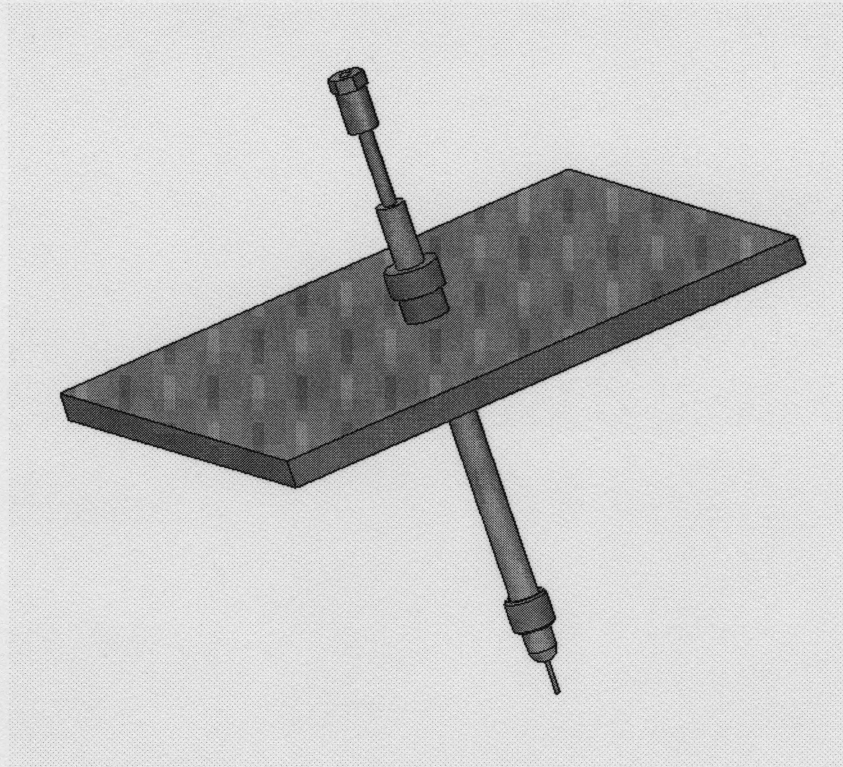
Dimension drawings of major components

(Dimensions in mm)

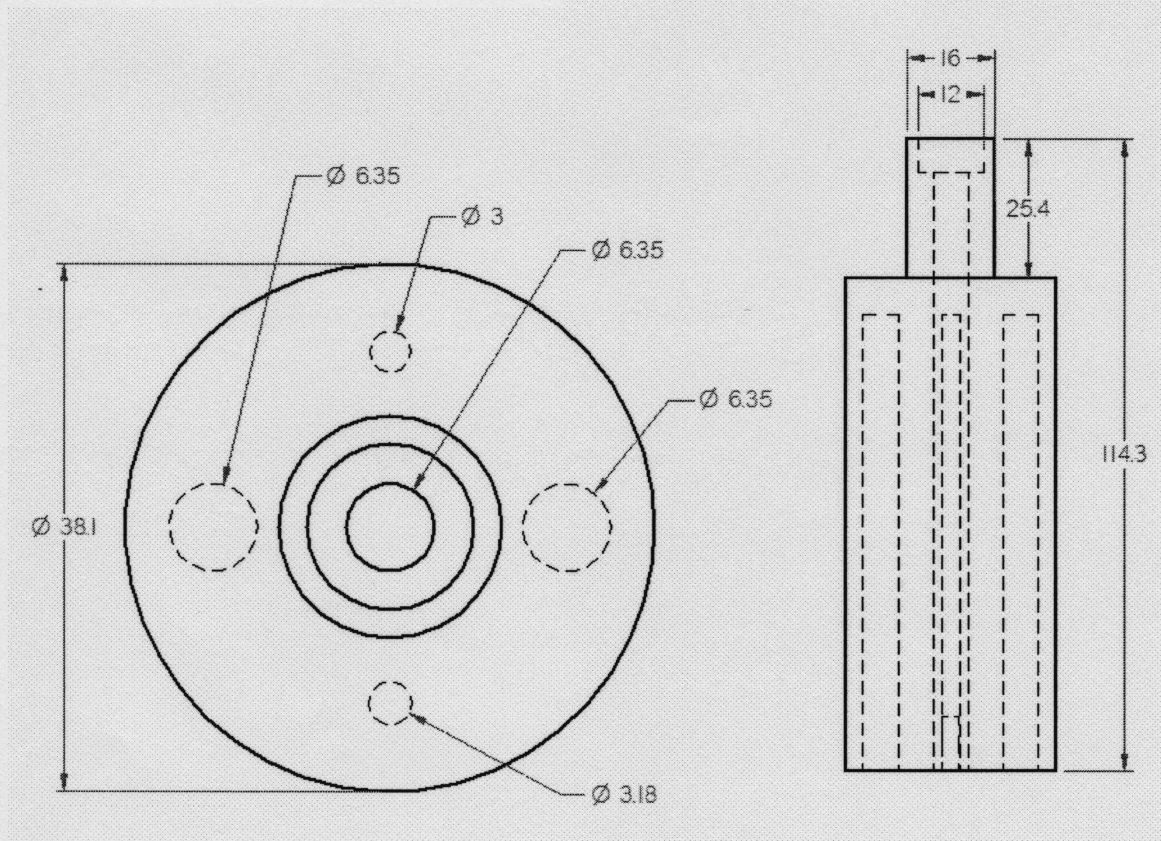
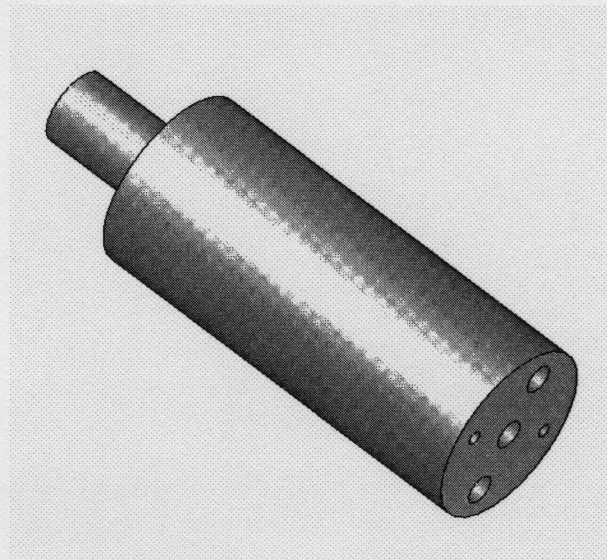
Completed Setup



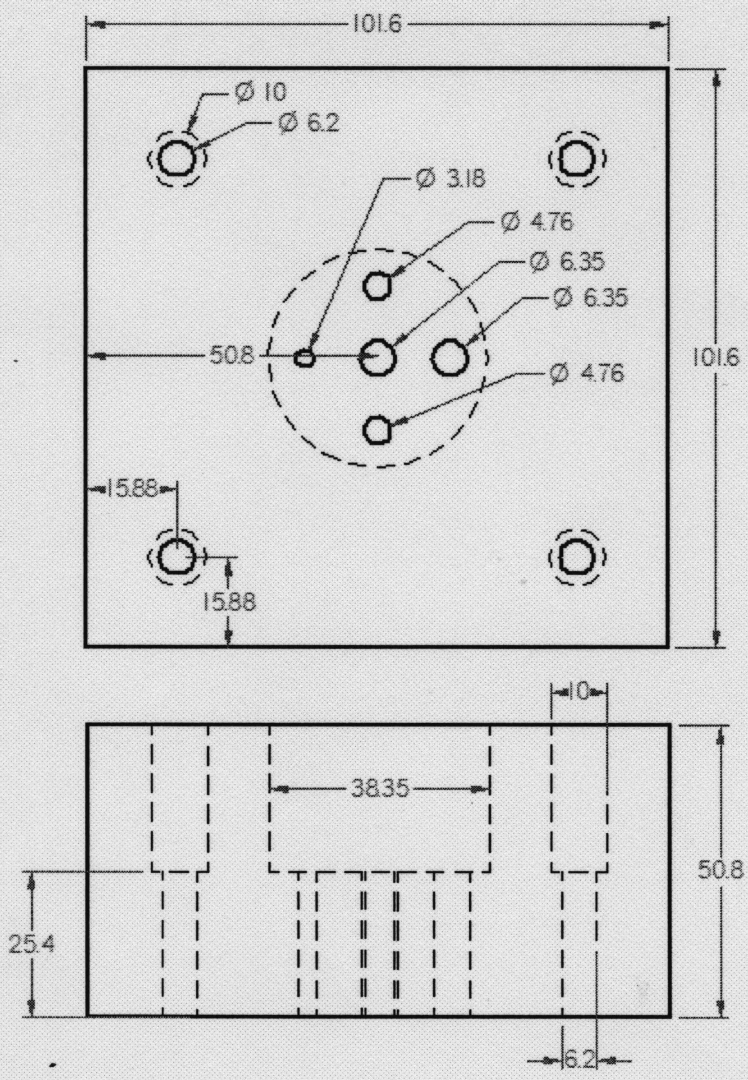
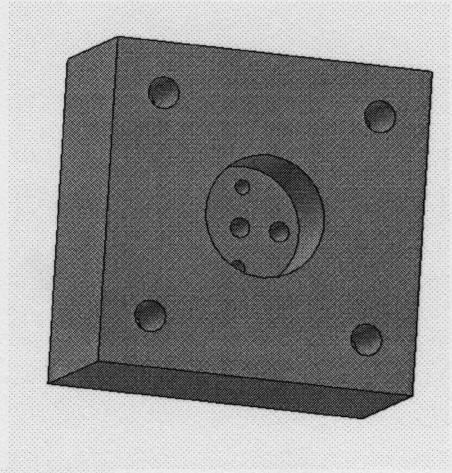
Corona Torch



Crystal Holder



Ceramic base block



Appendix B

A list of dominant optical emission bands in $\text{N}_2 - \text{O}_2$ plasmas

Table B1: Candidates for vibration transitions [1]

| Experiment | | Candidates | | | | |
|-------------|-----------|---------------|-----------------------------|---|--------------------------------|--|
| Wave Length | Intensity | Wave Length | Molecule | Type | System | Appearance |
| 318.57 | 120.2 | 316.19 | N ₂ | | Goldstein-K. | Degraded to red |
| | | 315.93 | N₂ | 9(1,0) | 2nd Positive | Degraded to red; Close tripleheader |
| | | 321.08 | O ₂ ⁺ | 8(2,6i) | 2 nd Negative | Degraded to red Double headed |
| | | 321.1 | O ₂ | | Herzberg I | Degraded to red |
| | | 323.2 | | | Schumann-R | |
| | | 318.88 | O ₃ | Other peaks 320.6;320.1;319.48; 318.15;317.16;316.26 | | |
| 340.37 | 379.4 | 337.13 | N₂ | 10(0,0) | 2nd Positive | Degraded to red |
| | | 339.78 | O ₂ ⁺ | 8(0,6i) | 2 nd Negative | Degraded to red |
| | | 342.12 | | 8(0,6ii) | | |
| | | 341.62 | | 2(2,7ii) | | |
| | | 339.31 | | 4(2,7i) | | |
| | | 337 | O ₂ | 10(3,5) | Herzberg I | |
| | | 340.26 | O ₃ | Other peaks:343.22;342,14;337.77 | | |
| 356.45 | 82.8 | 353.67 | N₂ | 8(1,2) | 2nd Positive | |
| | | 358.21 | N ₂ ⁺ | 9(1,0) | 1 st Negative | |
| | | 356.39 | | 9(2,1) | | |
| | | 354.89 | | 7(3,2) | | |
| | | 354.2 | O ₂ | 8(3,6) | Herzberg I | |
| | | 359.45 | O ₂ ⁺ | | 2 nd Negative | |
| | | 351.77 | | | | |
| 360.87 | 271.4 | 357.69 | N₂ | 10(0,1) | 2nd Positive | |
| | | 358.21 | N ₂ ⁺ | 9(1,0) | 1 st Negative | |
| | | 359.45 | O ₂ ⁺ | | 2 nd Negative | |
| | | 362.98 | | 8(0,7ii) | | |
| | | 360.37 | | 7(0,7i) | | |
| | | 363.3 | O ₂ | 8(3,6) | Herzberg I | |

Table B1 (continued)

| Experiment | | Candidates | | | | |
|-------------|-----------|---------------|----------|----------------|--------------------------------|---------------|
| Wave Length | Intensity | Wave Length | Molecule | Type | System | Appearance |
| 378.46 | 73.2 | 375.54 | N_2 | 10(1,3) | 2nd Positive | |
| | | 380.49 | | 10(0,2) | | |
| | | 378.28 | N_2^+ | 8(18,15) | 1 st Negative | |
| | | 376.16 | | 10(20,16) | | |
| | | 375.61 | | 5(22,17) | | |
| | | 379.2 | O_2 | (6,3ii) | Chamberlains | Tripleheader |
| | | 377.1 | | (6,3iii) | | |
| 383.38 | 114.8 | 380.49 | N_2 | 10(0,2) | 2nd Positive | |
| | | 383.05 | O_2^+ | 8(0,8i) | 2 nd Negative | Double headed |
| | | 382.9 | O_2 | 8(2,7) | Herzberg I | |
| | | 384 | | 5(0,6) | | |
| | | 385.79 | N_2^+ | 4(2,2) | 1 st Negative | |
| 394.3 | 14.2 | 391.44 | N_2^+ | 10(0,0) | 1 st Negative | |
| | | 394.3 | N_2 | 8(2,5) | 2 nd Positive | |
| | | 398.5 | O_2 | 6.4ii | Chamberlains | Triple headed |
| 397 | 24 | 399.84 | N_2 | 9(1,4) | 2 nd Positive | |
| | | 398.5 | O_2 | 6.4ii | Chamberlains | Triple headed |
| | | 393.8 | O_2 | 7(1,7) | Herzberg I | |
| 402.97 | 37.6 | 405.94 | N_2 | 8(0,3) | 2 nd Positive | |
| | | 403.1 | O_2 | 6.4i | Chamberlains | Triple headed |
| | | 400.9 | | 6.4ii | | |
| | | 398.5 | | 6.4iii | | |
| | | 406.4 | | 5(0,7) | | |
| 408.93 | 39 | 409.48 | N_2 | 8(0,3) | 2 nd Positive | |
| | | 406.4 | O_2 | 5(0,7) | Herzberg I | |
| | | 408.24 | O_2^+ | 8(0,9i) | 2 nd Negative | |
| | | 411.58 | | 8(0,9i) | | |
| 430.45 | 6 | 427.81 | N_2^+ | 9(0,1) | 1 st Negative | |
| | | 430.9 | O_2 | 7(0,8) | Herzberg I | |
| | | 432.6 | O_2 | (5,5ii) | Chamberlains | Triple headed |
| | | 431.7 | | (3,4iii) | | |

| | | | | | | |
|--------|-----|---------------|----------------------|--|--------------------------------|----------------------------------|
| 634.65 | 9.2 | 632 | N ₂ | | 1 st Positive | Degraded to violet Triple headed |
| | | 630 | O ₂ | | | Dimol emission |
| 677.35 | 17 | 670.48 | N₂ | | 1st Positive | |

References

- [1] G. Herzberg, "Molecular Spectra and Molecular Structure 1: Structure of Diatomic Molecules," D. Van Norstrand Company, Inc., New York, (1950).